The Pennsylvania State University

The Graduate School

College of Engineering

APPLICATIONS OF ACOUSTOFLUIDICS IN BIOTECHNOLOGY

A Dissertation in

Engineering Science and Mechanics

by

Adem Ozcelik

Submitted in Partial Fulfillment
of the Requirements
for the Degree of

Doctor of Philosophy

August 2016

The dissertation of Adem Ozcelik was reviewed and approved* by the following:

Tony Jun Huang
Professor of Engineering Science and Mechanics and Huck Distinguished Chair in Bioengineering Science and Mechanics
Dissertation Advisor
Chair of Committee

Bernhard R. Tittmann
Schell Professor of Engineering Science and Mechanics

Corina Drapaca
Associate Professor of Engineering Science and Mechanics

Wendy Hanna-Rose
Associate Professor of Biochemistry and Molecular Biology

Judith A. Todd
Professor
P. B. Breneman Head of the Department of Engineering Science and Mechanics

*Signatures are on file in the Graduate School

ABSTRACT

Acoustofluidics, the fusion of microfluidics and acoustics, has become a rapidly expanding research field that has various important applications in physical, chemical, biological and engineering sciences. Development of new acoustofluidic technologies has significantly contributed to the fields of biotechnology and nanotechnology in which gentle handling of single cells or precise manipulation of nanoscale samples such as nanowires are useful. Acoustic tweezer technology is a new method of manipulation of cells and small organisms. In addition to acoustic based translational manipulation, controlled and precise rotational manipulation of single cells or small model organisms such as Caenorhabditis elegans (*C. elegans*) can facilitate visualization and screening of normal and abnormal cell and sub-cellular morphology, contributing to our understanding of molecular mechanisms underlying human diseases. In this dissertation, I describe a novel on-chip manipulation method to rotate microparticles, cells and organisms in a controlled manner. To achieve this, I developed two different methods based on oscillating microbubbles and oscillating solid structures. For the first approach, I trapped air bubbles within predefined sidewall microcavities inside a microchannel. The trapped air bubbles were driven into oscillatory motion by an application of a low power biocompatible acoustic field. The oscillatory motion produced steady microvortices in the surrounding liquid. Depending on excitation of various modes of the bubble, effective in or out-of-plane vortex was generated, allowing rotation of objects of various shapes. Colloids, HeLa cells and *C. elegans* were precisely rotated using our method. For the second rotational manipulation approach, I utilize the acoustofluidic streaming vortices

generated via oscillating solid structures inside microchannels. Finally, I have demonstrated the capability of our method by analyzing the reproductive system pathologies and nervous system morphology in *C. elegans*. Using our device, we revealed the defective vulva morphology due to abnormal cell migration in the mutant worms. ARM is an easy-to-use, compact, cheap and biocompatible method, permitting rotation regardless of optical, magnetic or the electrical properties of the sample under investigation.

Microfluidics has been sprouting numerous applications including chemical synthesis, biological sample preparation, point-of-care diagnostics and enzymatic reactions. Microfluidic platforms offer many advantages for these applications such as small reagent volume, rapid and high resolution analysis, and low-cost fabrication. On the other hand, realizing on-chip fast mixing of viscous samples is very challenging due to the laminar flow nature of the liquids in confined channels. In this dissertation, a new acoustofluidic method of on-chip high viscosity fluid mixing is presented. This acoustofluidic method takes advantage of the acoustic streaming and jetting flows created by the acoustically generated bubbles inside polydimethylsiloxane (PDMS) microchannels. During the deep reactive ion etching process, the sidewall of a silicon mold features rough wavy structures, which can be transferred onto a PDMS microchannel through the soft lithography technique. I utilized the wavy structures of PDMS microchannel sidewalls to initiate and cavitate bubbles in the presence of acoustic waves. Through bubble cavitation, this acoustofluidic approach demonstrates fast, effective mixing in microfluidics. I characterized its performance by using viscous fluids

such as polyethyleneglycol (PEG). When two PEG solutions with a resultant viscosity 54.9 times higher than that of water were used, the mixing efficiency was found to be 0.92, indicating excellent, homogenous mixing. The acoustofluidic micromixer presented here has the advantages of simple fabrication, easy integration, and capability to mix high-viscosity fluids (Reynolds number: ~0.01) in less than 100 milliseconds.

TABLE OF CONTENTS

LIST OF FIGURES

LIST OF TABLES

ACKNOWLEDGEMENTS

First and foremost, I would like express my gratitude to Prof. Tony Jun Huang for his supervision and support that provided me the opportunity to pursue my doctoral studies. I am also grateful for my committee members Prof. Wendy Hanna-Rose, Prof. Bernhard R. Tittmann, and Prof. Corina Drapaca.

I would like to thank my mentor Dr. Daniel Ahmed for his friendship and guidance in my research. I am grateful to Nitesh Nama for his help with the numerical simulations and fruitful discussions during my studies. I am thankful to Dr. Ahmed Ahsan Nawaz, Dr. Mengqian Lu, Dr. Yuliang Xie, Dr. Yuchao Chen, Dr. Feng Guo, Chung Yu Chan, Zhangming Mao, Po-Hsun Huang, Dr. Sixing Li, Dr. Peng Li, Liqiang Ren, Joseph Rufo, Dr. Yanhui Zhao, Murat Kaynak, Sinem Orbay, Bugra Ayan, Rui Zhang, Mengxi Wu, Dr. James Lata, Dr. Shiyang Tang, Dr. Yi Zhang, Dr. Wu Liu, and Dr. Yusheng Bian. I would like to thank all the past and present members of the Acoustofluidics group.

I am thankful for the fellowship provided by the Republic of Turkey Ministry of National Education.

Last but not least, I would like to express my love to my wife Arzu and daughter Fatma Zumra Ozcelik who helped me go through my struggles. I express my love to my parents, Emine and Muhammet Ali, my sisters Hatice and Zehra, and my little brother Battal Ozcelik, for their never-ending support, and love.

Chapter 1

Introduction

1-1 A brief introduction of microfluidics

Microfluidics is an interdisciplinary research field that deals with manipulation of very small amounts of liquids generally from microliters to picoliters volumes [1]. A simple microfluidic device can be considered as a fluidic channel that has at least one dimension on the order of a few micrometers [2]. The capability to handle small volumes of fluids makes microfluidic devices excellent tools for chemical reactions that require fine control of reagent amounts and concentrations. Furthermore, microfluidic devices can be fabricated from various materials including polydimethylsiloxane (PDMS), polymethyl methacrylate (PMMA), polycarbonate (PC), polystyrene (PS), and glass which renders these devices low cost and disposable [3]. The above advantages (*i.e.* high precision, small size, low cost, and disposable) makes the microfluidic systems suitable for many applications such as point-of-care diagnostics, bioanalysis, biochemical reactors, single cell analysis and model organism studies [4]–[11]. Through integration of multiple microelectromechanical systems for functions including heating, sensing, and mixing in a single microfluidic device, micro total analysis systems have been also realized [12]–[15]. With the increasing functionalities and further miniaturizations, multi-component microfluidic systems have started replacing large-scale conventional laboratories for

various biological, analytical and physical applications which is also called lab-on-a-chip applications [16]–[21].

Behavior of fluids inside microfluidic channels is often different than what we experience in macro scale which enables unique fluid manipulation and control capabilities in these devices. The fluid flow in microfluidic channels can be described by using the Reynolds number (Re) which is given by:

$$\mathrm{Re} = \frac{\rho V^2 L^2}{\mu V L} = \frac{\rho V L}{\mu} \qquad 1\text{-}1$$

where ρ is the fluid density, V is the average flow velocity, L is the characteristic width of the fluidic channel, and μ is the dynamic viscosity of the fluid. The fluid flow in a microfluidic channel is characterized as laminar when Re is less than ~2000 (Figure 1.1(a)) [22]. Above that, the flow becomes turbulent which is defined by chaotic changes in fluid velocity and direction (Figure 1.1(b)). In the laminar flow regime, there is minimal interaction between the layers of fluids. In addition, the velocity profile is characterized by a parabolic curve for the pressure driven microfluidic systems as shown in Figure 1.1(a) which is also called as “no slip boundary condition”. Re is also defined as the ratio of the inertial forces to viscous forces. Therefore, low Re indicates that viscous forces are dominant over the inertial ones which is usually the case in microfluidic channels.

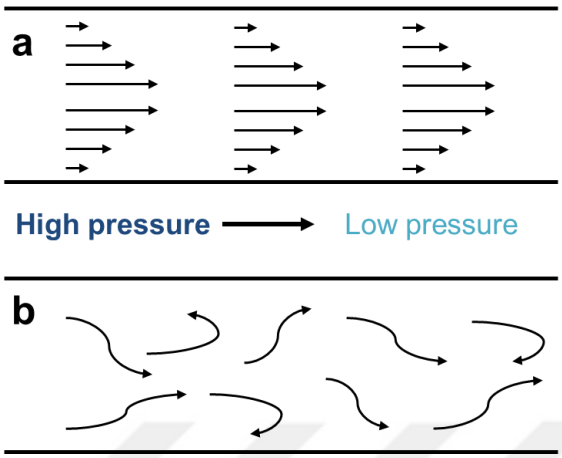

Figure 1.1. Cartoon depiction of the flow behavior at (a) low and (b) high Reynolds number. In the pressure driven flows, at the low Reynolds number, flow velocity reaches a maximum at the center of the channel while it goes to zero on the channel side walls.

1-2 A brief introduction of acoustofluidics

Acoustofluidics is a rapidly growing research field that has been conceived by the fusion of microfluidics and acoustics. Acoustofluidics mainly deals with the interaction of acoustic waves with fluids, microparticles, and biological cells. During this interaction, acoustic radiation and acoustic streaming forces are generated [23]–[25]. These forces have been widely used in the manipulation of matter in the applications of separation, sorting, patterning and transport of microparticles and cells [26]–[33]. There are two main utilization of acoustic waves in microfluidics; surface acoustic waves (SAWs) and bulk acoustic waves (BAWs). In SAW based devices, interdigital transducers, fabricated on a piezoelectric substrate, are used to apply an electric field to generate a propagating mechanical stress along the surface of the substrate. The most widely used mode of SAW in microfluidic research is Rayleigh SAW that has longitudinal and vertical shear components providing strong coupling with the liquid media. Traveling SAWs (tSAWs)

have been employed to induce fluid mixing and particle manipulation in droplet or closed channel microfluidic applications [26]. In addition to the tSAWs, interference of two oppositely propagating SAWs creates standing surface acoustic waves (SSAWs) that are characterized by periodically positioned pressure nodes and antinodes in a fluid media. SSAW are used in various manipulation and patterning applications by taking advantage of the primary acoustic radiation force generated in the fluid media [29]. In BAWs, the mechanical stress propagates in the volume of a piezoelectric material as opposed to the SAWs. Through coupling of the BAW transducers with glass capillary resonators [34], manipulation and separation of microparticles and cells have been demonstrated similar to the SAW based devices [35], [36]. BAW microfluidic devices usually requires higher power to generate strong acoustic forces which in turn requires active cooling elements to reduce the temperature inside the microfluidic channels [26]. Microbubbles present a low-power BAW application in microfluidics due to their ability to focus the acoustic energy in a local area [37]–[39]. Using transient microbubble oscillations or collapsing microbubble jetting flows, a wide range of applications have been demonstrated including fluid mixing, particle manipulation, cell lysis, and cell membrane poration [37]–[43]

1-3 Research objectives

Acoustofluidics offers contact-free, biocompatible, and highly versatile solutions to various applications in biotechnology from single cell manipulation [44] to cancer cell separation [30] and nanowire patterning [45] to fluid pumping [46]. In single cell studies

or multicellular model animal research, effective manipulation enables clear and accessible imaging of cellular and subcellular identities. Controllable and precise rotational manipulation of biological specimen under bright field or fluorescence microscopy provides multidimensional imaging of cells and tissues. In this dissertation, novel methods of rotational manipulation are presented in Chapters 2 and 3. In Chapter 2, trapped microbubble based acoustofluidic rotational manipulation is studied. By applying certain acoustic frequencies to trapped microbubbles inside a microchannel, acoustic microstreaming flows are generated and controlled in order to trap and rotate single cells and model organism *C. elegans.* In Chapter 3, oscillating solid structures of PDMS and glass slide are utilized to generate acoustic streaming flows for rotating samples. In Chapter 4, an acoustofluidic high viscosity fluid mixer is presented based on bubble inception and cavitation inside PDMS microchannels. In chapter 5, summary and future research directions are given.

Chapter 2

Rotational Manipulation of Single Cells and Organisms Using Acoustically Driven Microbubbles

In this chapter, a new rotational manipulation method for cells and small organisms like *C. elegans* (i.e. Caenorhabditis elegans) is developed utilizing the acoustic microstreaming flows generated by the trapped microbubbles excited by acoustic waves where in-plane and out-plane rotation can be achieved using higher oscillation modes of the trapped microbubbles. In the Introduction, an overview of the existing rotational manipulation methods and the brief description of the acoustofluidic rotational manipulation (ARM) are given. In the Experimental methods section, device fabrication and preparation as well as operation are explained. Results section gives the application of the ARM method to rotate single cells, microparticles, and *C. elegans*. Finally, discussion section outlines the importance and potential of the presented ARM method.

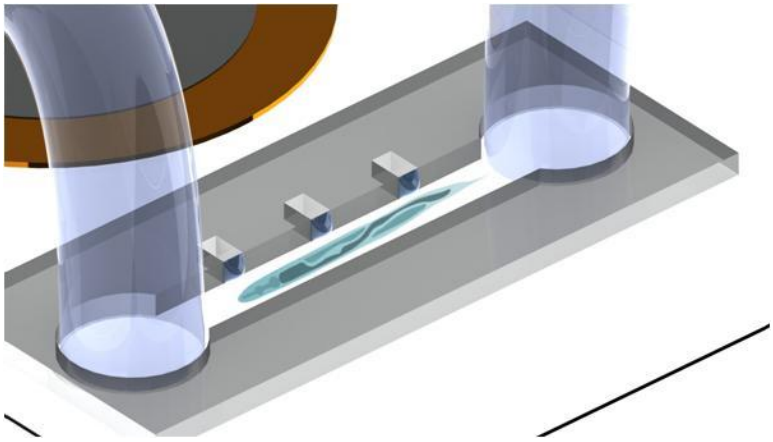

Caption: Cartoon schematic of the bubble based acoustofluidic rotational manipulation device.

2-1 Introduction

The field of microfluidics has introduced numerous platforms for the study of biological samples such as single cells, embryos, and model organisms [47], [48]. In the last decade, microfluidic laboratories for model organisms especially for *C. elegans* have become increasingly popular and efficient platforms for a wide spectrum of model animal studies [49]. One of the important applications of the mentioned platforms is to enable easy imaging and analysis of small worms like *C. elegans*. Some of the examples of these microfluidic laboratories for worm sensitivity, stimulation and behavioural analyses are shown in Figure 2.1. In these applications, generally PDMS is chosen as the material of the microdevice due to its transparency, oxygen permeability, and ease of fabrication. It is critical that optical access to the microdevice is available for easy observation. Even though there are various advantages of microfluidic devices for model animal studies, dynamic and multi-angle observation or probing of these model animals or single cells has not been achieved yet. Precise rotational manipulation of particles, cells, and multicellular organisms is an essential capacity in biotechnology that impacts various disciplines including single-cell analysis [47], [48], drug discovery [50], [51], and organism studies [52]–[54]. For example, distinct rotational behaviour due to different cell morphologies has been identified as a potential diagnosis method [55], [56]. Providing three-dimensional (3D) interrogation, rotational manipulation can reveal hidden genetic, cellular, and structural details which are vital in small organism phenotyping [11], [57]–[59], screening [8], [53], [60], and microsurgery[61]–[63] and which are not visible in typical translational manipulation.

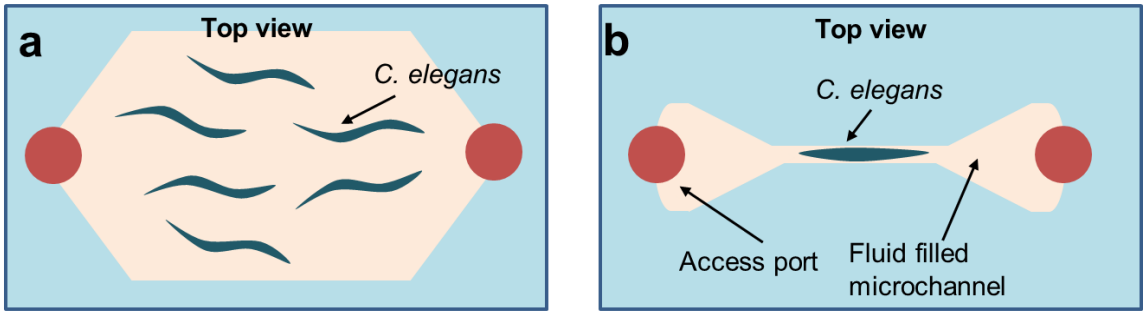

Figure 2.1. Schematic illustration of simple microfluidic laboratories for *C. elegans* studies. (a) A PDMS device is schematically depicted for the study of worm behavior under various stimuli such as mechanical, chemical, and electrical. (b) Schematic depiction of a device is shown that is used for worm immobilization and study under external stimuli.

Although several techniques have been established for the translational manipulation of particles and cells (*e.g.*, optical tweezers [64], magnetic tweezers [65], acoustic tweezers [9], [66], dielectrophoresis [67], and electrorotation [68], [69]), performing rotational manipulation has remained a significant challenge. Optical trapping and rotation of birefringent calcite particles was demonstrated as an example of optically driven micromachines [70]. The same concept, with vaterite particles, was used to guide the direction of axonal growth by applying a shear force from the spinning particles to the growth cone of the nerves [71]. Rotation of other microobjects like silica spheres, glass rods, and chromosomes was also achieved using spiral interference patterns that were created by interfering Laguerre-Gaussian light beams with a plane wave [72]. Optical tweezers are widely used for generating rotational manipulation but results are limited by physiological damage to cells and other biospecimens due to laser-induced heating [73]. Nanowires and carbon nanotubes were rotated by using phase-shifted AC voltages with a sequential phase shift[74]. A non-linear and irrotational Electric field was also employed to generate self-rotation of certain types of cells [75]. Rotating magnetic fields were

utilized for generating rotational motion of magnetic nanowires and tumor cells loaded with nanoparticles [56]. It is important to stress that the manipulation capability of existing methods strongly depends on the optical [70], [76], magnetic [56], [77], and electrical [75], [78] properties of the biospecimen. Recent studies have demonstrated acoustic vortex generation by array of individually addressable transducers excited at various phases [79]–[81], by acoustic transducers with helicoidal wave radiating surfaces [82], and by the optoacoustic technique [83]. However, as of yet, no existing method has demonstrated the capacity to rotate small model animals (such as *C. elegans*) or cells on-chip.

Acoustofluidic methods that fuse acoustics and microfluidics have the potential for dramatically improving methods for manipulating cells and small animals. Acoustically driven trapped microbubbles are important tools in microfluidics [84] that have been employed in various applications including microflow control[85], fluid mixing [86] and pumping [87], particle manipulation [32], [88], [89], and gradient and chemical waveform generation [90], [91]. In this dissertation, I describe an acoustofluidic rotational manipulation (ARM) method, which utilizes steady acoustic microstreaming vortices created by the oscillatory motion of air microbubbles trapped in a microfluidic channel. The oscillatory motion is driven by the application of a low-power acoustic field. The ARM method presented here represents the first acoustic-based rotational manipulation approach to rotate biospecimen. This method is extremely versatile. Its operation is independent of the samples' intrinsic properties. It allows effective and precise rotation of specimens over a wide range of sizes, shapes, and properties. In addition, compared to optical, magnetic, or electric field based rotational manipulation

methods, ARM is both extremely simple and practical. The entire operation requires only a single-layer polydimethylsiloxane (PDMS) channel and a simple, low-cost piezo transducer which can be integrated to existing microfluidic platforms. Using ARM, I have demonstrated for the first time, on-chip rotation of *C. elegans*, a valuable and frequently used model organism for elucidating the molecular mechanisms underlying human diseases [92]. I have used the ARM method to analyse the morphological features of *C. elegans'* nervous and reproductive systems. Precise rotation of multicellular organisms such as *C. elegans* can provide a powerful and versatile platform to perform efficient and rapid analysis of cell and tissue morphologies or positions in three dimensions. With the growing use of organism-on-chip tools for investigating microorganisms and cells, our method is anticipated to be an invaluable tool in biology, biophysics, and medicine.

2-2 Experimental methods

2-2-1 Device design and fabrication

A single-layer PDMS microchannel schematically illustrated in Figure 2.2 (height: 100 μm, width: 120 μm, length: 10 mm) with pre-designated microbubble trapping sites was fabricated using the soft lithography and the replica moulding technique. A silicon master mould for the microchannel was patterned using a positive photoresist (Shipley 1827, MicroChem, USA) and etched with Deep Reactive Ion Etching (DRIE) using an Alcatel Speeder 100Si BOSCH etch system (schematically illustrated in Figure 2.3). The etching process consists of octafluorocyclobutane (C_4F_8) passivation layer deposition and sulphur

hexafluoride (SF_6) plasma etching steps. Once the etching is completed, the height of the features that are used as for moulding the PDMS microchannels is measured using a KLA Tencor P-16+ stylus profiler as shown in Figure 2.4. The mould was then vapour coated with 1H,1H,2H,2H-perfluorooctyl-trichlorosilane (Sigma Aldrich, USA) to reduce its surface energy and any subsequent damage to the PDMS channel during the demoulding process. Sylgard 184 Silicone Elastomer Base and Sylgard 184 Silicone Elastomer Curing Agent (Dow Corning, USA) were mixed at a 10:1 (weight:weight) ratio and cast onto the silicon mould. The uncured PDMS on the silicon mould was then degassed in a vacuum desiccator for 2 hours to remove any air microbubbles and later cured at 65 ℃ for 2 hours. After gently removing the cured PDMS from the silicon mould, the inlets and the outlets were punched into the PDMS using a reusable biopsy punch (Harris Uni-Core, Ted Pella, USA). The microfluidic channel device and a 25x60 mm micro cover glass (SuperSlips, VWR, USA) were treated with oxygen plasma for 10 and 60 seconds, respectively. Then, the PDMS device was bonded to the cover glass, and kept at 65 ℃ overnight (Figure 2.5). A piezoelectric transducer (81-7BB-27-4L0, Murata Electronics, Japan) was then attached to the glass slide adjacent to the channel using a thin layer of epoxy (84101, Permatex, USA). Actual device assembly is shown in Figure 2.6.

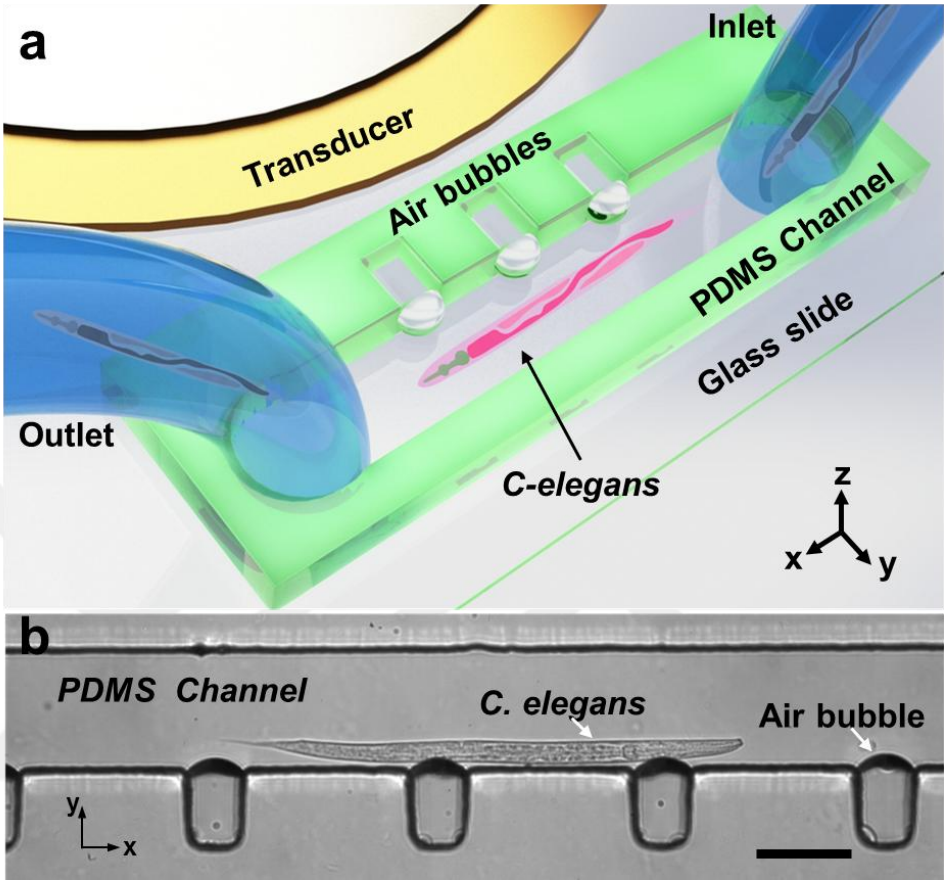

Figure 2.2. Design and operation of the acoustofluidic rotational manipulation (ARM) device. (a) A schematic of the experimental setup (not to scale). The piezoelectric transducer that generates acoustic waves is placed adjacent to the microfluidic channel. The acoustic waves actuate air microbubbles trapped within sidewall microcavities. (b) An optical image showing a mid-L4 stage C. elegans trapped by multiple oscillating microbubbles. Scale bar = 100 μm.

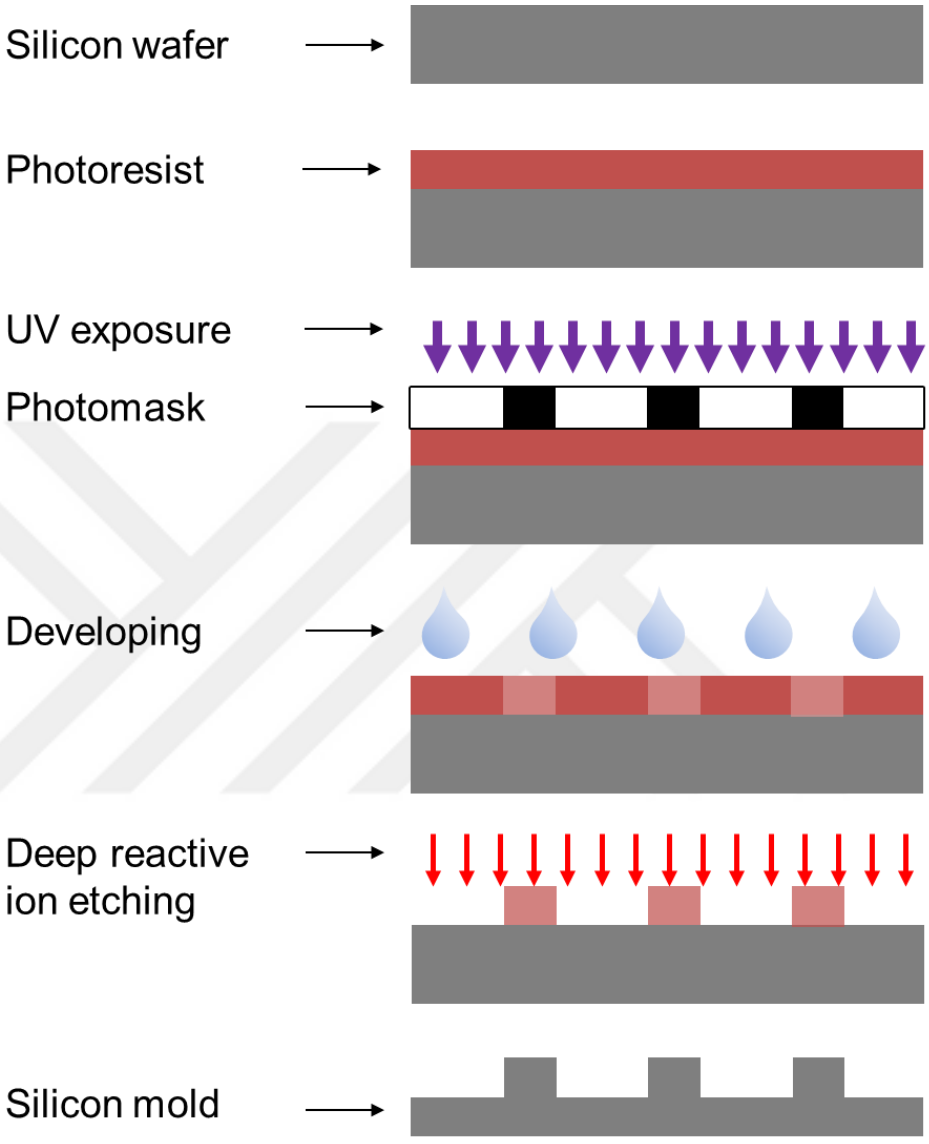

Figure 2.3. Schematic flow diagram of the silicon master mold fabrication.

Figure 2.4. KLA Tencor P-16+ stylus profiler is used to measure the height of the etched silicon features.

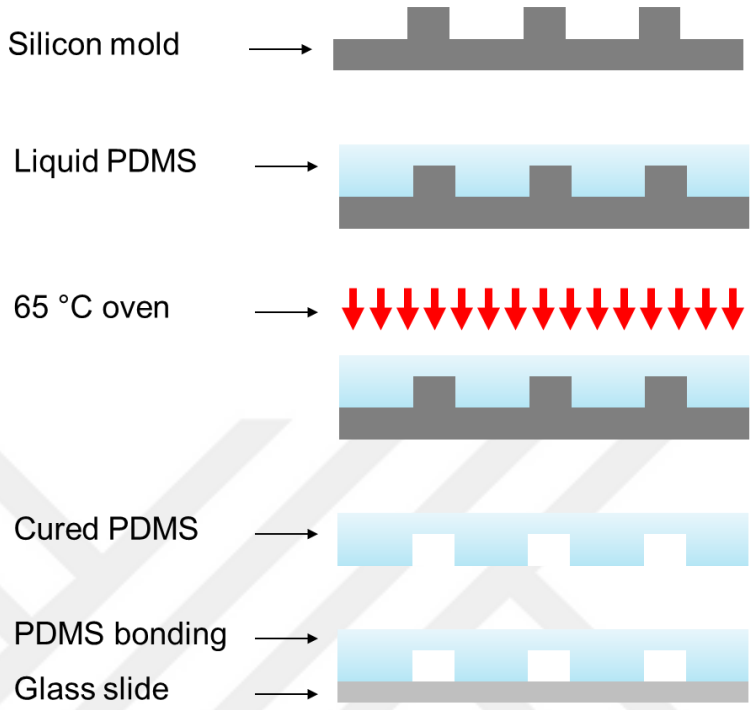

Figure 2.5. Schematic flow diagram of the PDMS device fabrication.

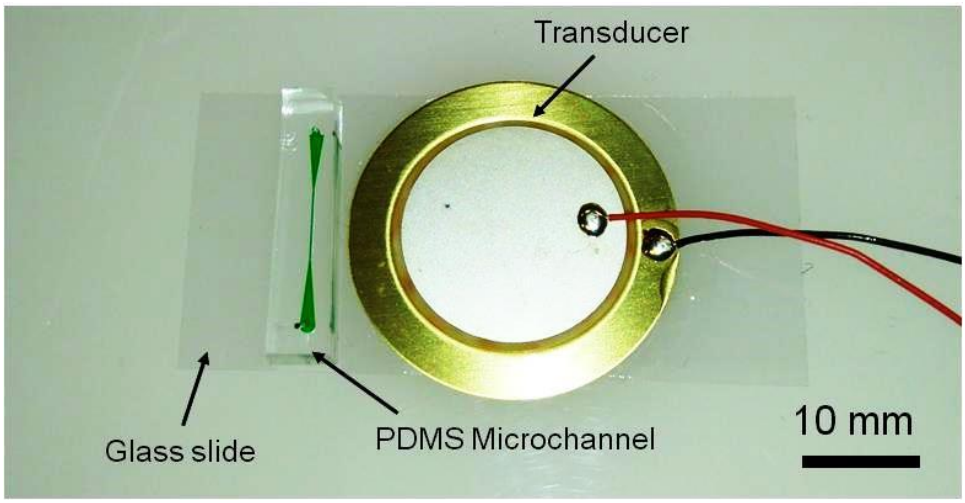

Figure 2.6 Optical image of the actual device assembly. Green color dye is injected inside the microchannel for better visualization of the fluidic part of the device. The piezoelectric transducer is bonded close to the PDMS microchip without direct contact.

2-2-2 Device operation

The glass slide, with the attached microfluidic channel and piezoelectric transducer, was mounted on an inverted optical microscope stage (TE-2000U, Nikon, Japan). Microparticles, cells, and *C. elegans* were infused into the channel through a 1 ml syringe (309659, Becton Dickinson, USA) by automated syringe pumps (Nemesys, Cetoni, Germany). Once the microbubbles were trapped via surface tension effect, the transducer was connected to a function generator to control the microbubble activation using a sine wave produced by a function generator (AFG 3011, Tektronix, USA). The driving voltages used in the experiments were 2–20 $V_{PP.}$ The working frequency for the rotational manipulation was adjusted by sweeping the frequency. The entire working station is shown in Figure 2.7 including the electronic equipment and the microscope.

2-2-3 Image acquisition

Microfluidic cell and worm images were captured at room temperature (~25 ^{0}C) using an inverted microscope (Eclipse TE2000-U, Nikon, Japan) with 4x, 10x, 20x, and 60x objectives (numerical aperture: 0.45). Images were captured by Nikon imaging software (NIS-Advanced, Nikon, Japan) using a Coolsnap CCD digital camera (CoolSNAP HQ2, Photometrics, USA). High-speed images were recorded by a Photron FASTCAM Viewer (PFV, Photron, USA) using a fast camera (Fastcam SA4, Photron, USA). For fluorescence imaging, a Nikon filter cube (excitation: 470 nm, emission: 515 nm) and a fibre optic illumination system (Intensilight, Nikon, Japan) were used.

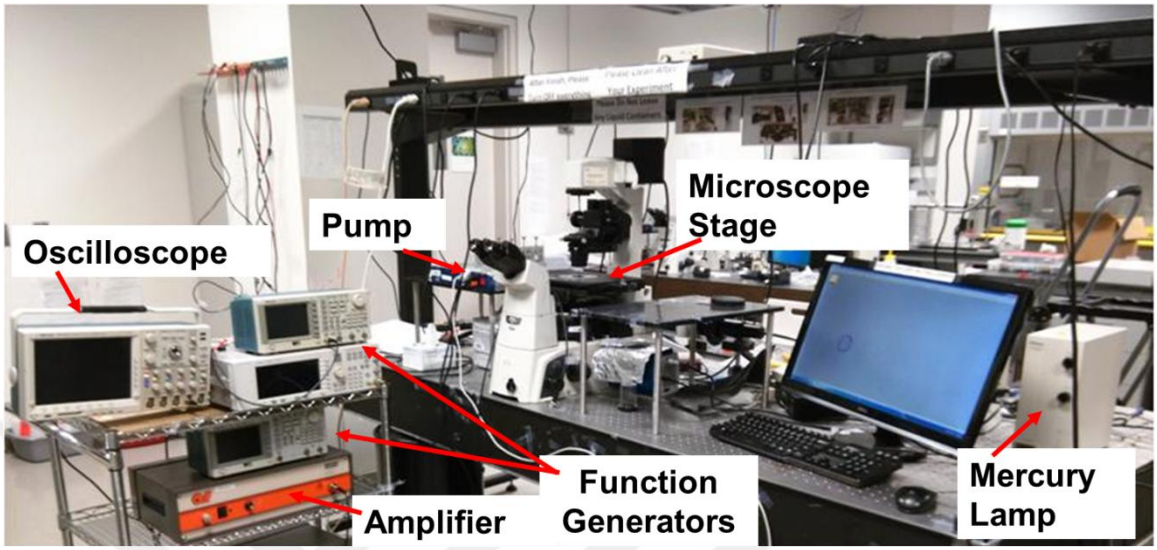

Figure 2.7. Experimental setup and work station for date acquisition.

2-2-4 Cell and particle preparation

HeLa cells (purchased from ATCC) were incubated in DMEM/F12 medium (Gibco, Life Technologies, USA), containing 10% fetal bovine serum (Gibco, Life Technologies, USA) and 1% penicillin−streptomycin (Mediatech, USA). 5 x 10^5 ml^{-1} HeLa cells were suspended in MEM solution and were injected into the microfluidic channel. Polystyrene beads (polybead, Polyscience, USA) were prepared in DI water (~10^6 ml^{-1}) at room temperature.

2-2-5 Nematode strains

N2: a wild isolate of *C. elegans* from Bristol, UK**.**

BL5715: *inIs179* II; *him-8(e1489)* IV; a transgenic nematode strain carrying *ida-1*::*GFP* (*inIs179*). GFP is expressed in a subset of neurons (including ALA neurons) and the neuroendocrine uv1 cells.

SU93: *jcIs1* [*ajm-1*::*GFP* + *unc-29*(+) + *rol-6(su1006)*] IV; a transgenic nematode strain carrying adherens junction marker -1 (*ajm-1*) fused to GFP. GFP expression is seen at the apical surfaces of cells.

PS4308: *syIs107* [*unc-119*(+) + *lin-3(delta-pes-10)*::*GFP*; a transgenic nematode strain carrying Epidermal Growth Factor (EGF) homolog *lin-3*::*GFP*. GFP expression is seen in the anchor cell (AC) and VulF lineages during vulva development.

Strains N2, BL5715, SU93 and PS4308 were provided by the Caenorhabditis Genetics Center (CGC), which is funded by NIH Office of Research Infrastructure Programs (P40 OD010440).

2-2-6 Nematode growth and maintenance

Nematode Growth Medium (NGM) agar was made by dissolving and autoclaving 3 g of NaCl, 17 g of agar, and 2.5 g of peptone with 975 ml of H_2O. When the autoclaved media cooled down to 65^0 C, 1 ml of 1 M $CaCl_2$, 1 ml 5 mg/ml of cholesterol in ethanol, 1 ml of 1 M $MgSO_4$, and 25 ml of 1 M KPO_4 buffer were added to it. All strains were grown on 60 mm NGM agar petri plates at standard growth conditions of 20 ^oC[93]. The *E. coli* strain OP50 was used as the nematode food source on NGM plates.

2-2-7 Levamisole treatment

An M9 solution was made by adding 3 g of KH_2PO_4, 6 g of Na_2HPO_4, and 5 g of NaCl to 1 litre of H_2O. The solution was autoclaved. When cool, 1 ml of sterile 1 M $MgSO_4$ was added to it. A mixed staged population of *C. elegans* collected from three NGM plates was suspended in 200 µl M9. 50 µl of the resulting *C. elegans* pellet was

treated with 100 µl of 50 mM levamisole [(-) tetramisole hydrochloride, Sigma-Aldrich, USA] for 15 minutes. The *C. elegans* were sedated with 500 µl of 100 mM levamisole just before injecting them into the microfluidic chamber.

2-2-8 RNAi technique

Genes were knocked-down by feeding double-strand RNA (dsRNA) to *C. elegans* in order to degrade its complimentary messenger RNA (mRNA). Briefly, in order to express *nhr-25* dsRNA, *E. coli* HT115 harbouring isopropyl-β-D-thiogalactosidase (IPTG) inducible T7 polymerase was grown in LB-ampicillin (50 µg/ml) overnight at 37^0 C. 200 µl of bacterial culture was seeded onto NGM agar plates containing 50 µg/ml of carbenicillin, 12.5 µg/ml of tetracycline, and 0.4 mM of IPTG. These plates were left overnight for drying at room temperature. Three or four L4 stage SU93 worms were placed on each plate and their F1 progeny were observed for vulva ring morphologies.

2-3 Numerical simulation

The numerical simulations shown in Figure 2.8 were performed using the open source finite element library, deal.II. Owing to the difficulties associated with obtaining a direct solution for problems involving acoustic streaming [94], we utilized a perturbation approach to split the flow variables into the first- and second-order components. The acoustic streaming response of the fluid can be characterized by the second-order system of equations, which in turn is driven by the first-order equations. The fluid response is

governed by the standard Navier-Stokes equations for a linear, viscous compressible fluid:

$$\frac{\partial \rho}{\partial t} + \nabla \cdot (\rho v) = 0 \tag{2-1}$$

$$\rho \frac{\partial v}{\partial t} + \rho(v \cdot \nabla)v = -\nabla p + \mu \nabla^2 v + (\mu_b + \frac{1}{3}\mu)\nabla(\nabla \cdot v) \tag{2-2}$$

where ρ is the mass density of the fluid, p is the fluid pressure, and μ and μ_b are the shear and the bulk dynamic viscosities, respectively. We employ Nyborg's perturbation approach [95] where the fluid velocity, pressure, and density are assumed to be of the following form:

$$\begin{aligned} v &= v_0 + \varepsilon \tilde{v}_1 + \varepsilon^2 \tilde{v}_2 + O(\varepsilon^3) + \ldots \\ p &= p_0 + \varepsilon \tilde{p}_1 + \varepsilon^2 \tilde{p}_2 + O(\varepsilon^3) + \ldots \\ \rho &= \rho_0 + \varepsilon \tilde{\rho}_1 + \varepsilon^2 \tilde{\rho}_2 + O(\varepsilon^3) + \ldots \end{aligned} \tag{2-3}$$

where ε is a non-dimensional parameter defined as the ratio of oscillation amplitude to the microbubble radius. Substitution of equation (2-3) in equation (2-1) and (2-2), and segregation of first-order terms yields a first-order system:

$$\frac{\partial \rho_1}{\partial t} + \rho_0(\nabla . v_1) = 0 \tag{2-4}$$

$$\rho_0 \frac{\partial v_1}{\partial t} = -\nabla p_1 + \mu \nabla^2 v_1 + (\mu_b + \frac{1}{3}\mu)\nabla(\nabla . v_1), \tag{2-5}$$

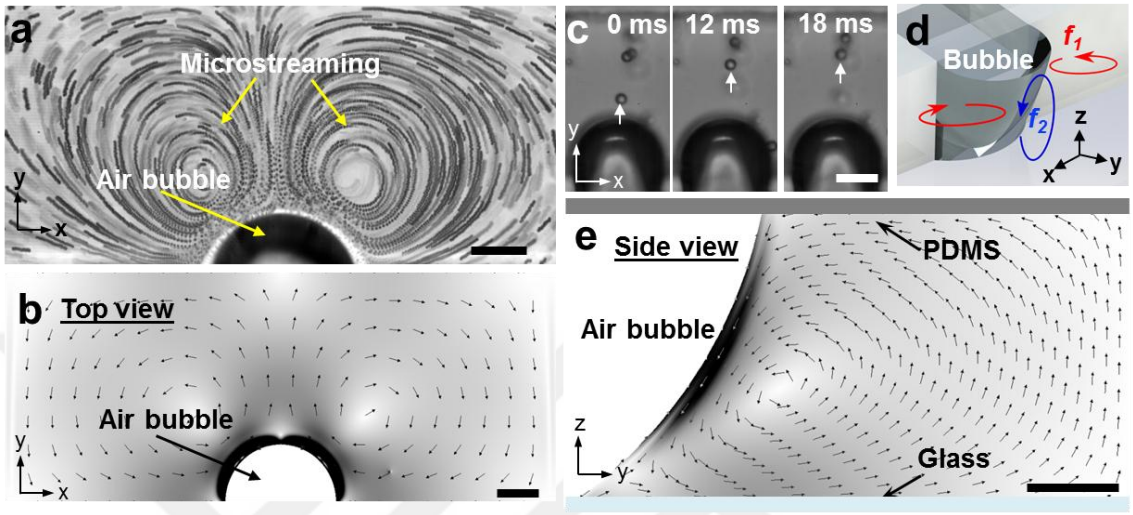

Figure 2.8. Experimental and numerical demonstration of acoustic microstreaming. (a) An optical image of acoustic microstreaming in the x-y plane during microbubble oscillation at a driving frequency of 24 kHz and voltage of 10 Vpp. (b) A simulation of microstreaming from the x-y plane (top view) of the microbubble. (c) An optical image of out-of-plane (perpendicular to the x-y plane) microstreaming during microbubble oscillation at 25.5 kHz and 15 Vpp. (d) 3D sketch demonstrating in-plane (marked in red) and out-of-plane (marked in blue) acoustic microstreaming vortices at frequency f1 and f2, respectively. (e) A graphic simulation illustrating microstreaming in the y-z plane (side view) of an asymmetric microbubble. Scale bars = 30 μm. In both (b) and (e) the arrows indicate the direction of the streaming velocity, while the colour plot shows the magnitude of the streaming velocity ranging from white (min) to black (max).

Following the same procedure for the second-order terms, and a subsequent time-averaging over a period of oscillation, yields the second-order system of equations:

$$\langle\frac{\partial\rho_2}{\partial t}\rangle + \rho_0\nabla.\langle v_2\rangle = -\nabla.\langle\rho_1 v_1\rangle, \qquad 2\text{-}6$$

$$\rho_0\langle\frac{\partial v_2}{\partial t}\rangle + \langle\rho_1\frac{\partial v_1}{\partial t}\rangle + \rho_0\langle(v_1.\nabla)v_1\rangle = -\nabla p_2 + \mu\nabla^2 v_2 + (\mu_b + \frac{1}{3}\mu)\nabla(\nabla.v_2). \qquad 2\text{-}7$$

We successively solved the first- and the second-order equations to obtain the streaming velocity of the fluid. Due to the high computational costs associated with the full 3D computations of the system, we performed separate 2D simulations for the top view and the side view, as shown in Figure 2.8. The primary purpose of the experimental results in Figure 2.8 is to identify the nature of the acoustic streaming field inside the microchannel. To this end, Figure 2.8(a),(b) show the top view (x-y plane) of the device experimentally and numerically, respectively, demonstrating the two vortices produced around the microbubble surface. Figure 2.8(c) shows the position of a microparticle on a focal plane close to the glass slide at different times, where the increasing distance of the microparticle from the microbubble surface demonstrates that the acoustic streaming velocity is pointed away from the microbubble surface. Figure 2.8(d) shows a sketch of the 3D nature of the flow field which was also identified in our experiments, where we observed a single vortex in the y-z plane arising from the non-symmetric nature of the microbubble surface in this plane. The non-symmetric nature of the microbubble surface can be attributed to the fact that the top and the bottom wall of the microchannel is made of different materials (PDMS and glass, respectively), resulting in different contact angles. This results in the formation of a single vortex in the y-z plane as demonstrated by the numerical simulations for an asymmetric microbubble surface in the y-z plane (Figure 2.8(e)).

2-4 Results

2-4-1 Working principle of the ARM method

The device setup (Figure 2.2(a)) includes a PDMS-based single layer microfluidic channel and a piezoelectric transducer. The channel contains linear arrays of rectangular microcavities (Figure 2.2(b)) that trap air microbubbles when liquid is injected. A piezoelectric transducer mounted on a glass slide adjacent to the channel generates acoustic waves. When the trapped microbubble is exposed to an acoustic field with a wavelength much larger than microbubble diameters, oscillations are created, which, in turn, generate acoustic microstreaming [96] (Figure 2.8).

A spherical microbubble undergoing both radial as well as transverse oscillations in an unbounded Newtonian fluid produces a second-order steady flow that scales with the product of radial (ε) and transverse (ε') microbubble oscillation amplitude and is linear in angular frequency, ω. For a fixed ratio of radial and transverse oscillations, the second-order streaming speed scales as $u \propto \varepsilon^2 \omega$ [95]. This scaling has been reported to be preserved even in low-symmetry cases such as a microbubble oscillating near a wall [97], [98], and similarly should be preserved in microcavities within our acoustofluidic channel. For such a trapped microbubble oscillating with a small amplitude ε, the flow field around the microbubble can be obtained via a perturbation expansion approach, $\boldsymbol{u} = \varepsilon \boldsymbol{u_1} + \varepsilon^2 \boldsymbol{u_2} + \cdots$. In a Newtonian fluid of density ρ, the oscillatory first-order velocity $\boldsymbol{u_1}$ induces a second-order steady flow (also known as the acoustic streaming) with a velocity $\boldsymbol{u_2}$ which is governed by a Stokes equation with a body force term induced by the first-order flow [94]. For an approximate semi-cylindrical microbubble

oscillating in the fundamental frequency, the liquid flow pattern is characterized by two symmetric vortices in the plane of oscillation as shown experimentally and numerically in Figure 2.8(a),(b)**,** respectively.

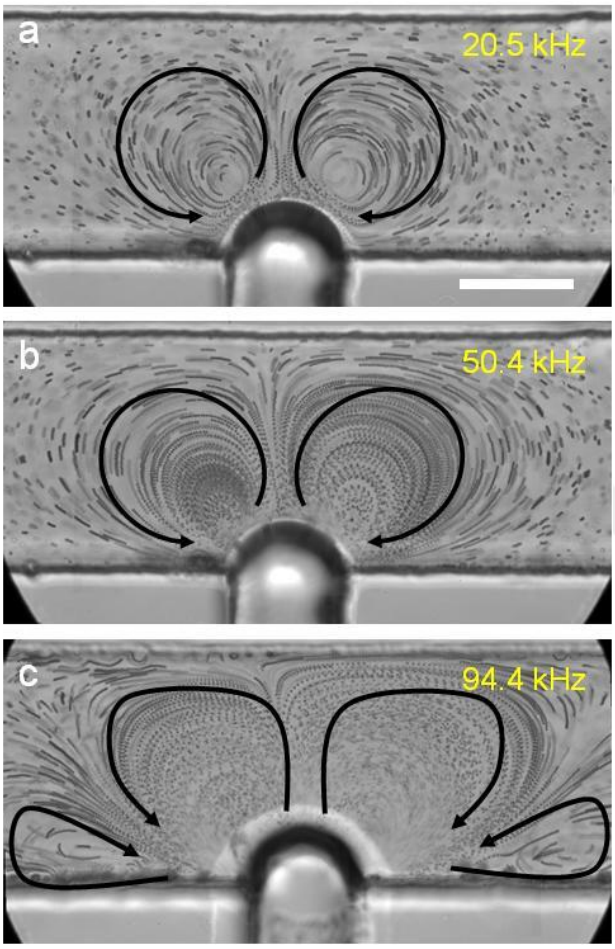

Figure 2.9. Microstreaming patterns at different modes. Streaming flow patterns near a 60 μm bubble at different excitation frequencies with polystyrene tracer particles. Superimposed high-speed images of acoustic microstreaming are shown at (a) 20.5 kHz, (b) 50.4 kHz, and (c) 94.4 kHz frequencies with 5 V_{PP}. The frequency dependence of microstreaming observed here is in agreement with the previous studies [99]. Scale bar = 60 μm.

A powerful feature of an oscillating microbubble in an acoustic field is that numerous modes of the microbubble can be excited to generate different microstreaming flow patterns. Our experiments demonstrated complex microstreaming patterns for higher

modes of oscillation (Figure 2.9). Additionally, we have observed that the acoustically excited microbubbles produce single out-of-plane microstreaming vortices (Figure 2.8(d)) as a result of microbubble shape distortion which occurs due to the difference in contact angles between the glass and the PDMS[100], as experimentally illustrated in Figure 2.8(c) and numerically simulated in Figure 2.8(e). The simulations shown in Figure 2.8(b),(e) are for the top view (*i.e.* the x-y plane) and side view (*i.e.* the y-z plane) of acoustic microstreaming induced by the microbubble.

When particles (polystyrene, cells, or organisms) are introduced near an oscillating microbubble in an acoustic field, they experience both acoustic radiation and microstreaming induced drag forces. Radiation force on particles arises due to the scattering of the incident waves from the oscillating microbubble. The time-averaged radiation force exerted on a spherical particle due to microbubble oscillation in an acoustic field can be expressed as [101]:

$$F_R = \frac{4}{3}\pi\rho\phi(\rho).\frac{a^4 a_S^3}{d^5}\omega^2\varepsilon^2 \qquad 2\text{-}8$$

$$\phi(\rho) = 3\frac{(\rho_S - \rho_M)}{(2\rho_S + \rho_M)} \qquad 2\text{-}9$$

where a, a_S, d, ω, ε are the radius of the microbubble, radius of the particle, distance between the microbubble and particle centre, angular frequency, and microbubble displacement, respectively; and ρ_M, ρ_S denotes the density of the surrounding liquid and density of the particle, respectively. Depending on the densities of the particle and the surrounding medium, this force can either be attractive or repulsive. Particles with density higher than that of the surrounding medium are attracted towards the microbubble

($\phi(\rho) > 0$) and particles with density lower than that of the medium are repelled ($\phi(\rho) < 0$). This expression is consistent with our experiments. For example, polystyrene particles (1.05 gcm^{-3}), HeLa cells (1.04 gcm^{-3}) [102], and *C. elegans* (1.08 gcm^{-3}) [103] are attracted towards the oscillating microbubbles. In addition, radiation force is strongly dependent on the distance between the microbubble and the particle centre, and is inversely proportional to the fifth power of d. However, radiation force alone cannot explain why particles of certain diameter are not trapped.

To gain a better understanding of the trapping mechanism of particles, we have to consider the effect of acoustic microstreaming on particles. Velocity (u) of the acoustic microstreaming flows due to an oscillating microbubble is given by [101]:

$$u = \frac{a^4}{d^5}\omega\varepsilon^2 \qquad 2\text{-}10$$

The force arising from acoustic microstreaming can be estimated by the Stokes' drag:

$$F_{AS} = 6\pi\mu a_S u_s \qquad 2\text{-}11$$

where μ and u_s are dynamic viscosity of the medium and the nonoscillatory velocity of the particle relative to the liquid, respectively. Figure 2.10(a)-(b) demonstrate the streaming effect on particles of different sizes. While initially all particles follow the streaming flows, 15 μm particles eventually get trapped at the microbubble surface.

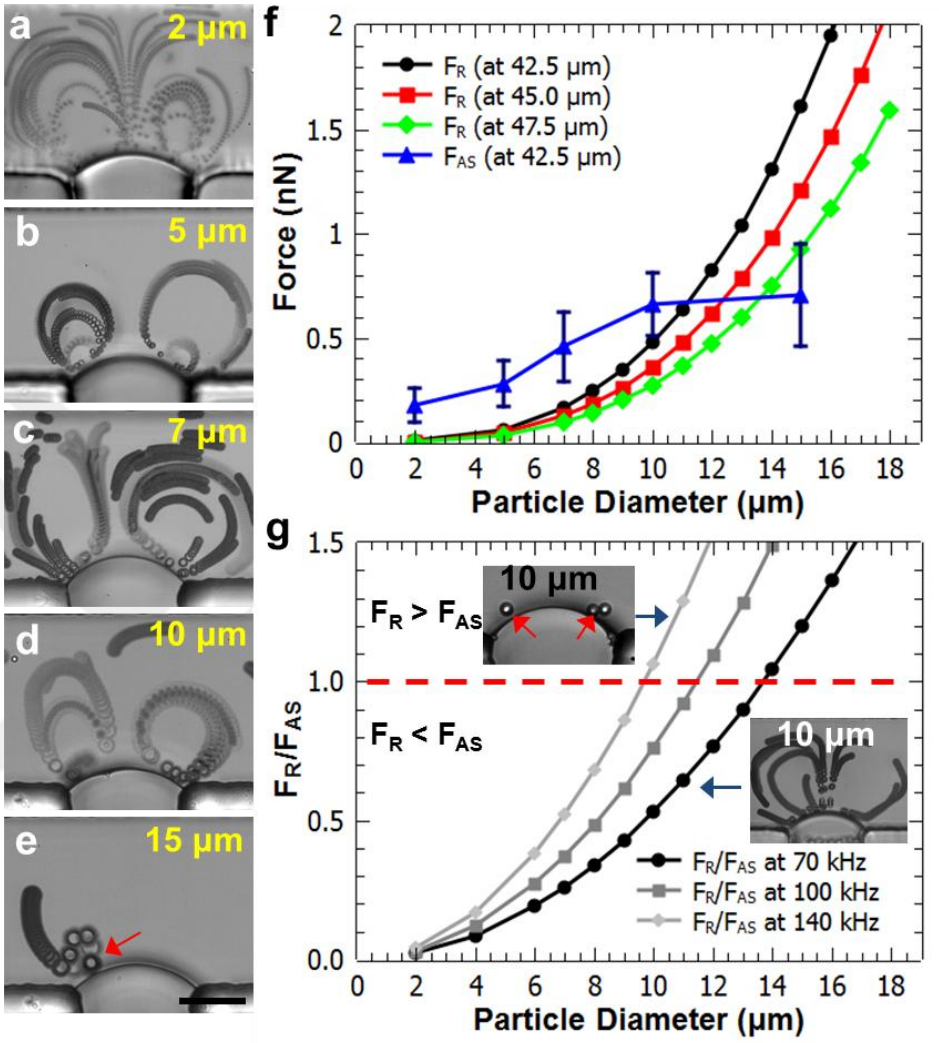

Figure 2.10 Acoustic radiation and acoustic streaming force analysis on particles with different sizes. Image sequence demonstrating (a)-(d) acoustic microstreaming of 2, 5, 7, and 10 µm polystyrene particles and (e) subsequent particle trapping of 15 µm particles at excitation frequency and amplitude of 70 kHz and ~3 µm, respectively. (f) Plots of acoustic streaming (triangle, F_{AS}) and radiation (F_R) forces. Radiation forces for three different particle-microbubble centre are plotted at 42.5 (circle), 45 (square), and 47.5 µm (diamond). (g) Ratio of acoustic radiation to streaming forces at 70, 100, and 140 kHz excitation frequencies are plotted. Insets of (g) shows 10 µm polystyrene particles being trapped (at 140 kHz) and following the streaming flows (at 70 kHz). Error bars represent standard deviation ($n \geq 5$). Scale bar = 50 µm.

In general, any particles that are placed near an oscillating microbubble experience both radiation and streaming forces. To understand whether a particle will be trapped by the microbubble or not, we have to analyse the competing forces and their magnitudes. As can be seen from equation 2-8 and equation 2-11, the radiation force scales with the cube of the particle radius, while the streaming force scales linearly with the particle radius. Thus, for smaller particles the streaming drag force dominates the motion of the particle until a transition size is reached, beyond which the radiation force becomes more dominant. Figure 2.10(f) describes the competing streaming and radiation forces for polystyrene particles of different sizes. The acoustic streaming force for particles with different sizes is calculated from the experimentally measured particle velocities. Here the distance between the microbubble and particle centre is ~42.5 μm. Radiation force is estimated for a microbubble acoustically excited at 70 kHz at experimentally measured $\varepsilon = 3$ μm. The critical particle size for which the competing forces are equal can be determined by intersection of the two plots in Figure 2.10(g), which corresponds to approximately 11 μm. For particles with diameter, $2a_s < 11$ μm, $F_{AS} < F_R$, microstreaming dominates over the radiation forces, which results in microparticles following the streamlines. On the other hand, for particles with diameter, $2a_s > 11$ μm, radiation force dominates over the microstreaming force and since $\phi > 0$, microparticles are attracted towards the microbubble.

In addition, when the centre-to-centre distance between the microbubble and particle is increased, the radiation force weakens ($F_R \propto \frac{1}{d^5}$), thus the threshold of critical particle size increases as marked by the intersection points of the red and green plots, as

demonstrated in Figure 2.10(f) It is also worth noting that as the particle size increases, the streaming force is compensated by the radiation force as demonstrated by the 15 μm polystyrene particle, in F_{AS} plot in Figure 2.10(f).

A similar approach regarding particle trapping by the competing forces can also be estimated by taking the ratio of the two forces: radiation (F_R) to the acoustic streaming forces (F_{AS}) [101]:

$$\frac{F_R}{F_{AS}} \approx \rho\mu^{-1}\phi(\rho)a_s^2\omega \qquad 2\text{-}12$$

The critical particle size for which the competing forces are equal can be determined when $F_R/F_{AS} = 1$, corresponding to a particle of diameter ~14 μm. For particles lower than the transition diameter, $F_R/F_{AS} < 1$, acoustic microstreaming dominates over radiation force. On the other hand, for particle greater than the transition diameter, $F_R/F_{AS} > 1$, radiation force dominates and microparticles are attracted towards the microbubble as indicated in Figure 2.10(g). By increasing the excitation frequencies of the microbubble, it is also possible to decrease the critical particle diameter to trap smaller sized particles, as demonstrated in the inset of Figure 2.10(g) in which 10 μm polystyrene particles are trapped at 140 kHz, whereas similar size particles follow the streamlines at 70 kHz.

We also note that when $F_R/F_{AS} = 1$, a particle is at equilibrium at some distance away from the microbubble, *i.e.*, the radiation force on a particle is balanced against the

streaming force. The number of events of micro objects remaining in equilibrium is rare; however, HeLa cells are sometimes seen to be at equilibrium, which may be attributed to its size variation. We note that the rotation of the particles is not sensitive to whether particles are trapped at the microbubble surface or trapped at equilibrium at some small distance away from the microbubble surface. Rotation is observed in either case. Estimating the exact critical size is not precise based on the current particle analysis, however, it provides a design strategy to trap and rotate smaller particles. Based on the analysis, one would expect that the transition or critical particle diameter to be similar in both analyses, however variations may arise from the fact that the streaming induced force is experimental in Figure 2.10(f) and theoretical in Figure 2.10(g). It is also important to note that the streaming speed in equation 2-10 is derived for a spherical microbubble, whereas the microbubble trapped in our experiment is asymmetrical. Nevertheless, the above analyses are useful and reliable for quantitatively describing the experimentally observed particle trapping behaviour. Finally, the above analysis is consistent with our experiment that the force generated by an oscillating microbubble is size dependent. Thus a *C. elegans* due to its much larger size experiences a larger radiation force, $F_R/F_{AS} > 1$, thus exhibiting a stronger trapping force. Our experiments show that a single microbubble can pull the entire mid-body of a *C. elegans* against the channel sidewall. (Figure 2.11). Presence of this trapping force enables us to rotate cells and worms under 3 μL/min within the microchannels of dimensions 120 μm in width and 100 μm in depth. However, once the rotation is halted, the samples drift, which may

impede proper imaging. Therefore, all rotational experiments were performed at zero flow rate, while maintaining the pressure at the inlets and the outlets at near equilibrium.

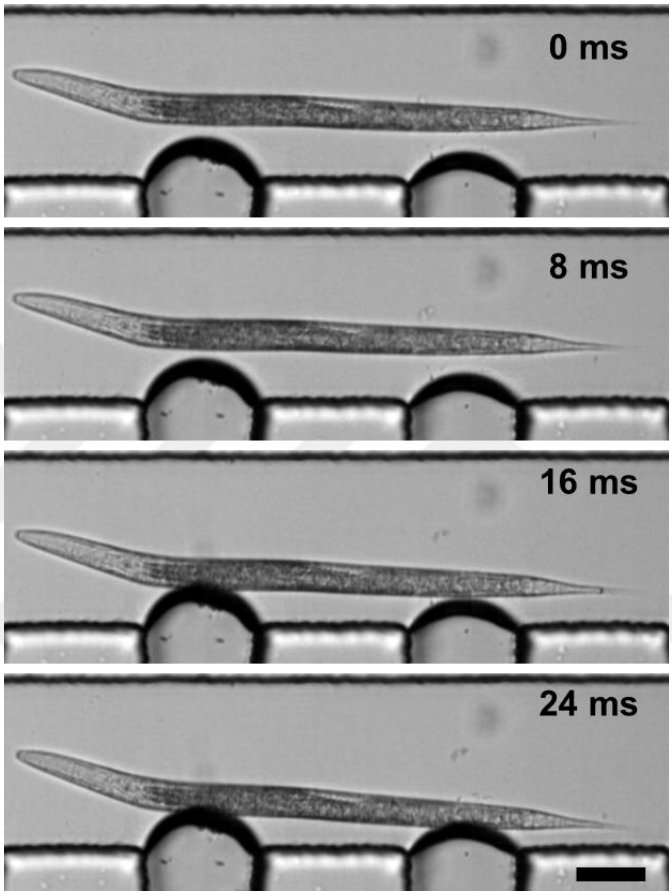

Figure 2.11. Acoustic radiation force on a *C. elegans*. Image sequences shown demonstrate trapping of a *C. elegans* by oscillating bubbles where the whole body of a worm is attracted to two microbubbles within 24 milliseconds. Scale bar = 60 μm.

2-4-2 Rotation of microparticles and HeLa cells

Diluted microparticles were introduced near an oscillating microbubble in the microfluidic channel. The particles were attracted towards the microbubble due to the radiation force of an oscillating microbubble. Particles trapped at the microbubble surface would reposition themselves by sliding along the air-liquid interface. Observation using fast camera showed that particles are actually trapped at the nodes, the points with

minimum oscillation displacement, of an oscillating microbubble (Figure 2.12). To demonstrate the node positions and particle trapping, we drove the microbubble at higher harmonics (60–90 kHz) and large driving voltage (20 V_{PP}), to ensure discernable nodes and antinodes at the microbubble surface (Figure 2.12).

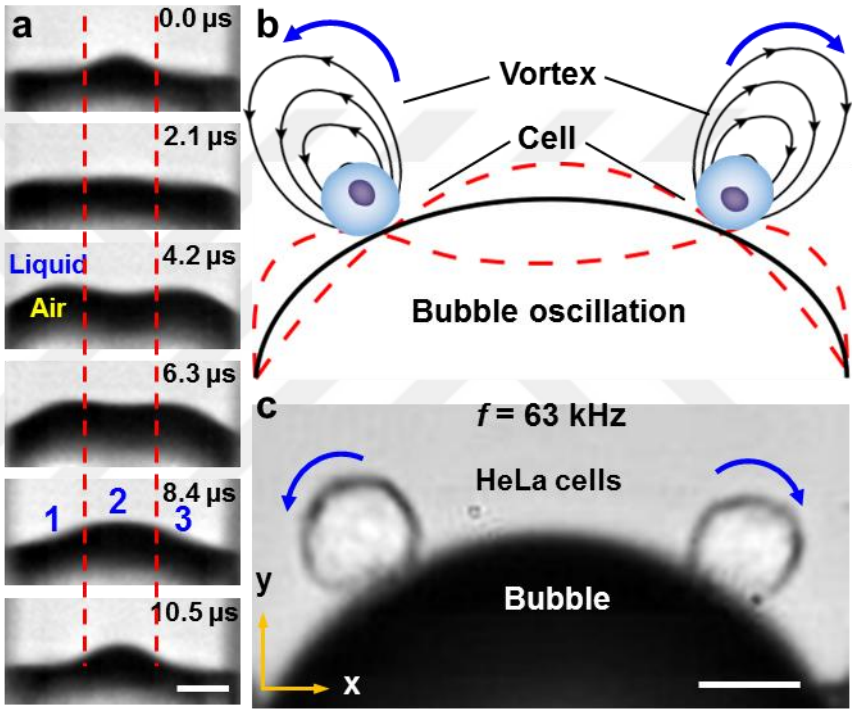

Figure 2.12. Particle trapping at nodes. (a) An image sequence captured at 360,000 frames per second demonstrates bubble oscillation at 63 kHz trapped within a sidewall microcavity. The oscillation consists of multiple nodes marked by dotted red lines. (b) A cartoon schematic demonstrating cell trapping located at the nodes and the subsequent rotation during vortex generation. (c) An optical image demonstrates trapping and rotation of HeLa cells at the nodal positions of an oscillating microbubble at 63 kHz. Scale bars = 10 µm.

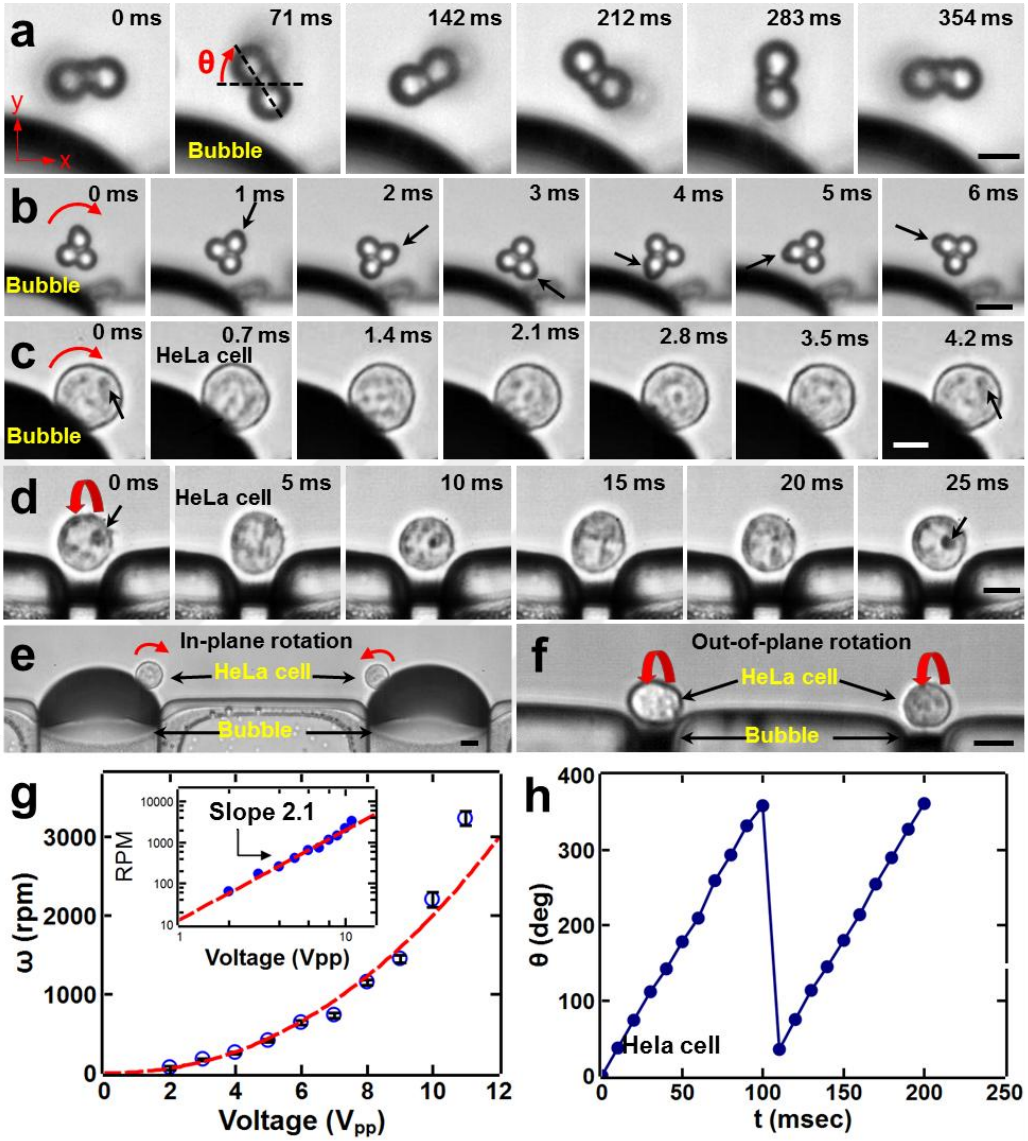

Figure 2.13. High-speed imaging showing the rotational motion of microparticles and cells caused by an oscillating microbubble. Clockwise and in-plane rotation motion of (a) a doublet and (b) a triplet. (c) Counter clockwise in-plane rotation of a HeLa cell. (d) Out-of-plane rotation of a HeLa cell. Parallel (e) in-plane and (f) out-of-plane rotation of a HeLa cells. (g) Plot of rotational speed ω against driving voltage V_{PP} of a HeLa cell driven by an oscillating microbubble, with a constant excitation frequency. The rotational rate of the cell varies as the second power of the driving voltage, $\omega \propto V^{2.1}$. (h) Plot of the rotational angle θ versus a function of time t for a HeLa cell. Error bars represent standard deviation ($n \geq 5$). Scale bars = 10 μm.

In a liquid, the hydrodynamic flow field produced by microstreaming induces a torque on the microparticle/cell and caused rotation. This rotation can be instantaneously turned on and off due to the low Reynolds number associated with the acoustic microstreaming. The Reynolds number for microbubble microstreaming was estimated [98] to be $Re = \left(\frac{\varepsilon}{a}\right)^2 \left(\frac{2\pi f a^2}{v}\right)^{1/2} \sim 2$, where ε=3 μm is the displacement amplitude of the microbubble oscillation, $a = 35\,\mu\text{m}$ is the microbubble radius, $f = 70\,\text{kHz}$ is the excitation frequency, and $v = 1.0 \times 10^{-6}\ \text{m}^2\text{s}^{-1}$ is the kinematic viscosity.

Rotational manipulation of doublets, triplets, and HeLa cells were demonstrated as image sequences in Figure 2.13(a), (b) and (c), respectively. The torque created by an oscillating microbubble is determined by the intensity of the ambient acoustic field, which is controlled by adjusting the voltage applied to the piezoelectric transducer. Rotational rates can be as large as ~3000 rotations per minute in water. The rotation axis of cells and particles follows the streamlines of the in-plane and out-of-plane vortices of the oscillating microbubbles and undergoes *z*-axis (Figure 2.13(c),(e)) and *x*-axis (Figure 2.13(d),(f)) rotation, respectively. In addition, the rotation axis is independent of the shape of the rotated object as demonstrated by *z*-axis rotation of HeLa cell, doublet and triplet in Figure 2.13(a), (b) and (c), respectively, thus making the system versatile.

The z-axis rotation rate of HeLa cells was quantified using direct high-speed measurements of the liquid/microbubble interface. We observed that the amplitude of the microbubble oscillation is linearly proportional to the amplitude $\boldsymbol{V}$ of the voltage applied to the signal generator in water [91], [104]. Thus for a given microbubble configuration at a fixed excitation frequency, the acoustic microstreaming, and therefore, particle rotation

$\boldsymbol{\omega}$ attained by microbubble oscillations, should scale as $\boldsymbol{V^2}$ in water. Figure 2.13(g) shows that this quadratic relation is reasonably well satisfied by the oscillating microbubble confined in the microfluidic channel. Furthermore, it is worth noting that microbubbles excited at higher harmonics generate smooth rotational motion for cells or microparticles as demonstrated by cycles of rotation in Figure 2.13(h).

A unique advantage of the ARM method is the ability to tune the rotation axis of the cells by tuning the excitation frequency or by designing bubbles with different sizes. By changing the frequency, different modes of microbubble oscillations can be achieved which results in a tuneable rotation axis as demonstrated in Figure 2.14. An important attribution to bubble oscillating in an acoustic field is that higher resonant modes can be excited. The modes of oscillation are primarily dependent on the applied acoustic frequency and independent of the applied acoustic pressure (or voltage). The excitation frequency (ω) and the mode (n) number are related by [105]

$$\omega_n = (n-1)(n+1)(n+2)\frac{\gamma}{\rho a^3} \qquad 2\text{-}13$$

where γ is the surface tension of the liquid. We demonstrate tunability of the orientation axis of a *C. elegans*' egg by sweeping the excitation acoustic frequency from 60 to 90 kHz. Figure 2.14 demonstrates that the change in rotation axis is not continuous but rather discretized. This is expected since the rotation occurs predominantly at the harmonics and the harmonics of the oscillating bubble occurs at certain frequencies.

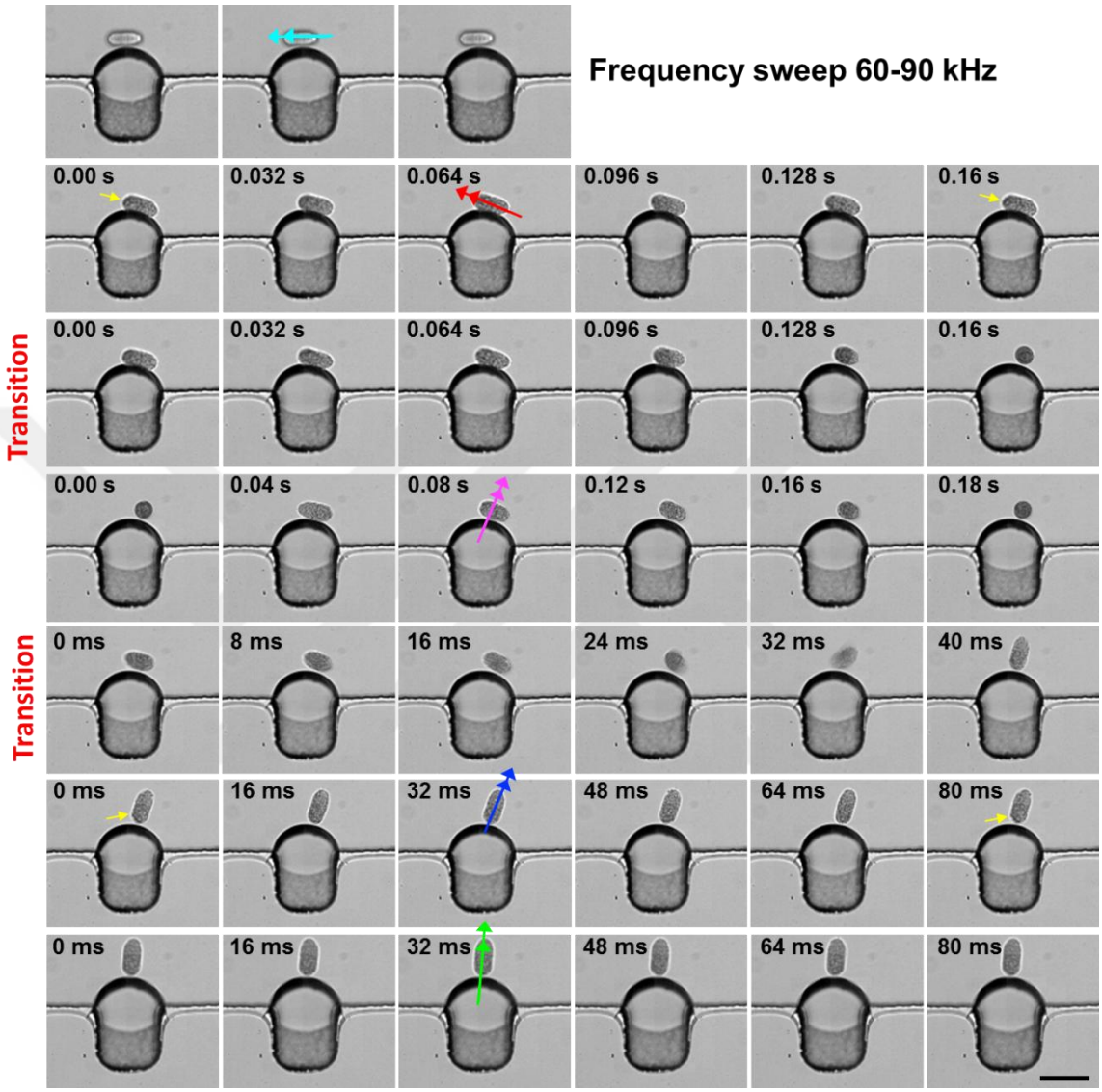

Figure 2.14. Tunability of the rotation axis. Excitation frequency of a 70 μm bubble is swept from 60 to 90 kHz in order to demonstrate the change of rotation axis of a *C. elegans'* egg. During the course of its rotation, the egg switches rotation axis (marked with double headed arrows) and orientation. Scale bar = 50 μm.

By changing the bubble size, out-of-plane rotation of a HeLa cell is achieved using ~10 μm width microbubbles (keeping the channel height constant at 100 μm) as shown in Figure 2.13(d). This geometry yields consistent and reproducible out-of-plane rotation of cells. High aspect ratio trapped bubble, oscillating at fundamental frequency,

constrains its oscillations along the channel height, thus contributing to out-of-plane streaming. Rotation of the HeLa cells about x-axis could become useful for a thorough scan of the cell, while maintaining the focus of the microscope constant at a certain plane within the cell diameter. It is also worth noting that the trapping and rotation of particles and cells are coupled. That is, particles that are attracted by the oscillating microbubble are simultaneously being trapped by the radiation force and rotated with the streamlines of acoustic microstreaming vortices, as demonstrated by z- and x-axis rotations of particles and cells.

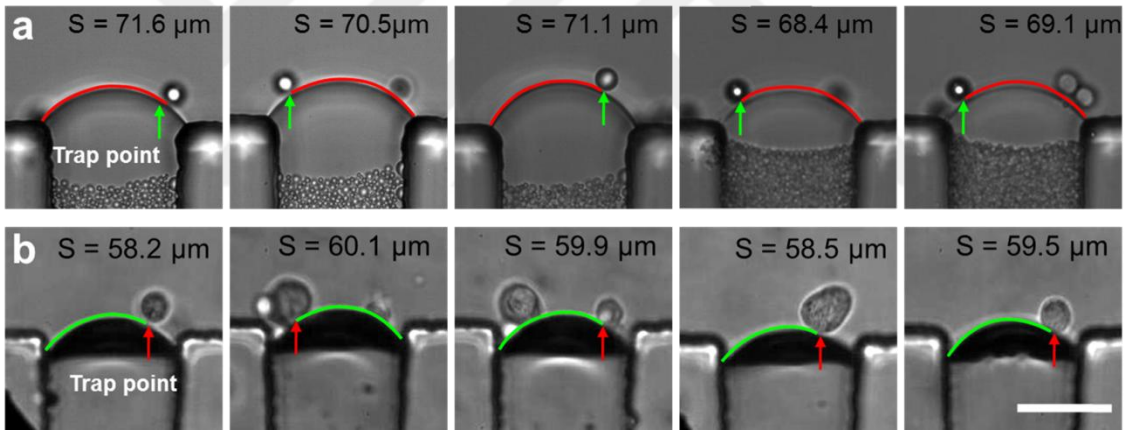

Figure 2.15. Particle and cell trapping. Characterization of trapping positions with microbubbles oscillating at 70 kHz is performed by measuring the arc length drawn from the edge of the bubble to the trapping point. Trapping positions for (a) particles and (b) HeLa cells with arc length measured to be 68.7 ± 1.8 µm and 58.8 ± 2 µm, respectively ($n \geq 10$ for particles and cells). Scale bar = 50 µm.

Trapping position repeatability and rotational stability of 15 µm particles and the HeLa cells were analysed. Trapping position repeatability is characterized by measuring the arc length from the edge of the bubble to the point where the particle/cell sits ($n \geq 10$ for particles and cells); arc length is measured to be 68.7 ± 1.8 µm and 58.8 ± 2 µm for

particles and cells, respectively (Figure 2.15). The small difference in the arc lengths arises from the slight curvature difference between two sets of microbubbles in water and cell medium (Dulbecco's Modified Eagle Medium), and can be attributed to surface tension variation between the two fluid media [106].

For rotational stability analysis, we manually tracked the spatial positions (*x* and *y* coordinates) of the particles/cells' center during rotation ($n \geq 10$ for particles and cells), as shown in Figure 2.16. For each particle, we measured the mean and standard deviation during its rotation of multiple cycles. Error bars (*i.e.*, the standard deviation) demonstrates the stability during rotation of each particle. Similarly, we measured the mean and standard deviation of the center position of the HeLa cells. For the slightly elongated HeLa cells, the center point was taken as the intersection of major and minor axes of the cells. The scattering of the center positions of the HeLa cells is higher than that of particles, and can be attributed to various size and shape distribution of the cells. Nonetheless, the x and y positions of each cell/particle remain within 1 μm during rotation.

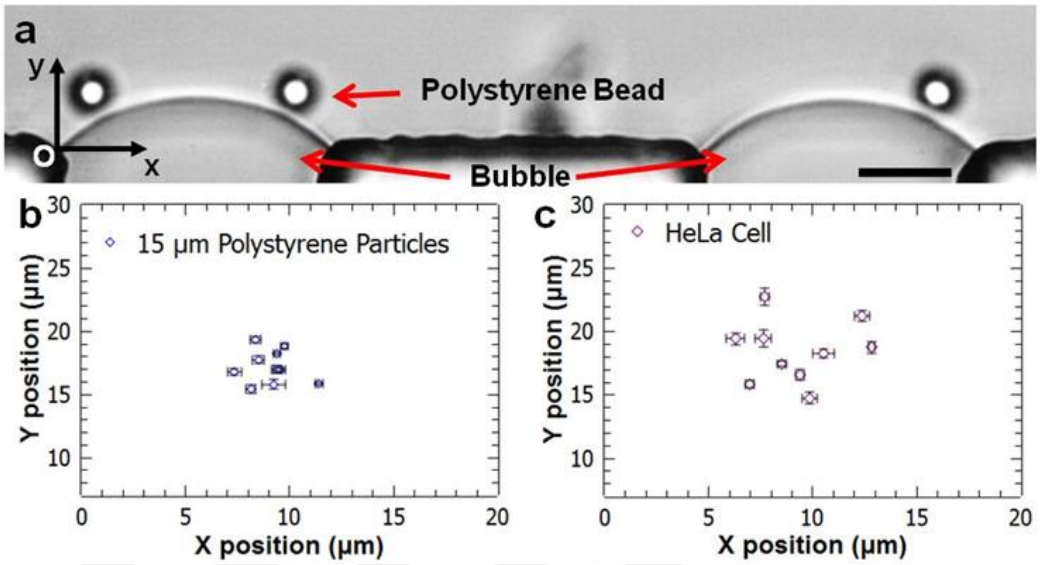

Figure 2.16. Rotation stability analysis for HeLa cells and microparticles. (a) An image showing three 15 μm polystyrene particles trapped by 70 μm microbubbles. Origin point for each particle/cell is set to the edge of the microbubble for measuring the spatial coordinates during rotation. The spatial distribution of the x and y coordinates for 10 different (b) particles and (c) cells during their multiple rotations are plotted. Scale bar = 25 μm.

2-4-3 Rotation of *C. elegans*

Mixed populations of wild-type *C. elegans* at various development stages were introduced into the ARM device after they were treated with levamisole, an anesthetic agent. During acoustic excitation of the microbubbles at their resonances, *C. elegans* were attracted (Figure 2.17(a)) and trapped at the surface of the microbubbles, and the excitation frequency is adjusted to out-of-plane vortex to rotate the *C. elegans* along the *x*-axis. We were particular about the *x*-axis rotation of *C. elegans*, which is the same as the long axis of the worm, as it allows investigating the worm at different planes. A thorough scan of the worm can be achieved for this mode of rotation axis, while maintaining the microscope focus constant within the worm diameter.

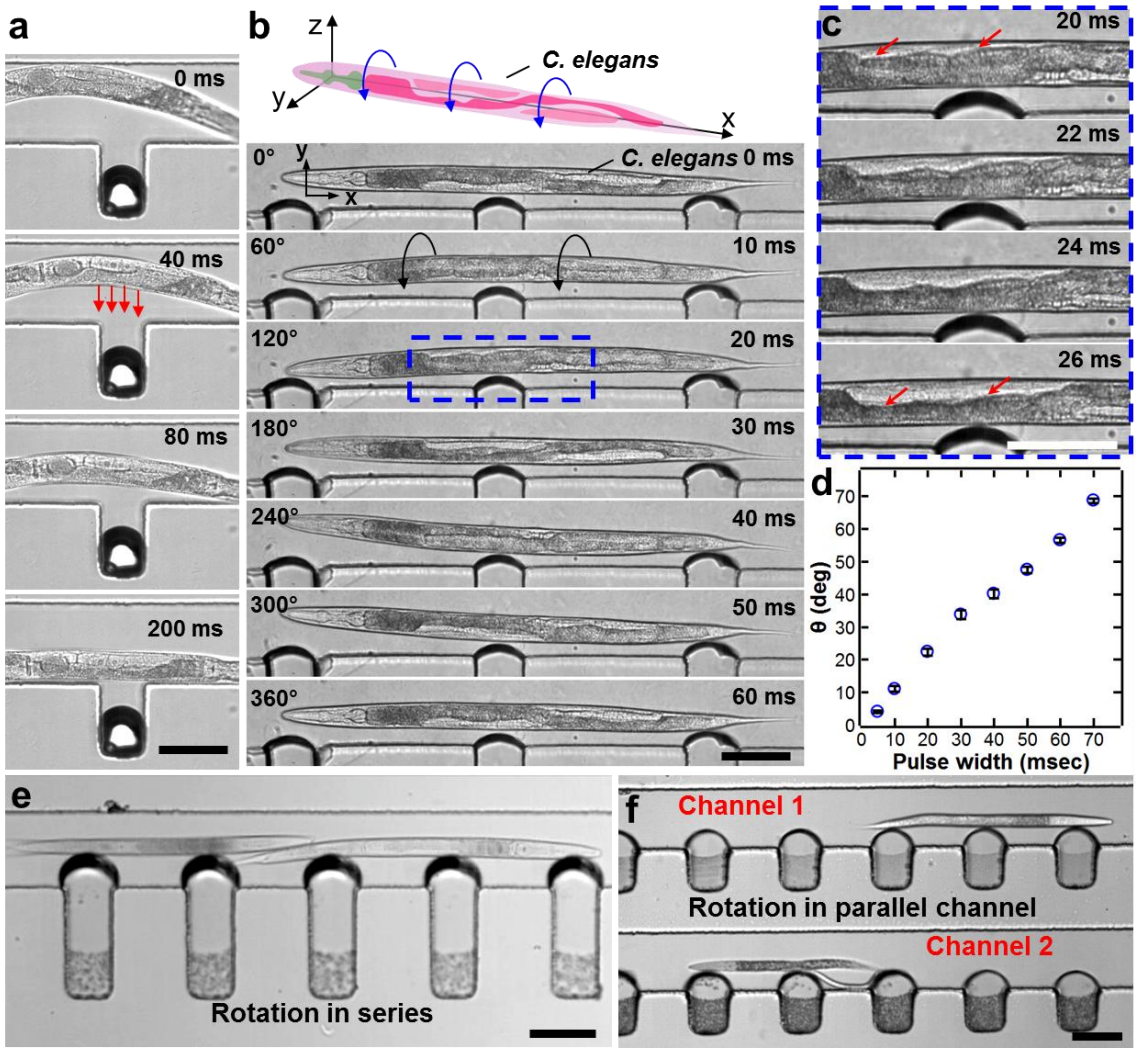

Figure 2.17. High-speed images demonstrating trapping and rotation motion of *C. elegans*. (a) Image sequence demonstrate trapping of *C. elegans* by an oscillating bubble *via* acoustic radiation force. (b) The rotational motion of an L4 stage *C. elegans* caused by simultaneous oscillation of multiple microbubbles. (c) A rotation sequence of the boxed area at a tighter time resolution. (d) Plot of the rotational angle θ versus a function of time t for a *C. elegans*. Error bars represent standard deviation ($n \geq 5$). Scale bars = 100 μm. Trapping and rotation of multiple worms (e) in series arrangement in a channel and (f) in parallel arrangement in multiple channels.

Unlike cells and particles, the trapping and rotation of *C. elegans* under the current experimental setup is decoupled due to restriction of the channel geometry and the fact that multiple bubbles are trapping the worm. Therefore, *C. elegans* cannot follow the in-

plane streaming flows (z-axis rotation), and stays trapped until the out-of-plane vortices develops by tuning the frequency.

By adjusting the duration of applied power to the piezoelectric transducer, rotation of the animal could be either continuous or stepwise. Using continuously applied power at ~ 92.2 kHz the animal underwent smooth 360 ° rotations (Figure 2.17(b),(c)**)**. Stepwise rotation was achieved through short pulses of acoustic excitation ranging from 5 to 70 millisecond durations shown in Figure 2.17(d) for a fourth larval (L4) stage worm. Stepwise rotation, along with voltage control, allowed repositioning of the *C. elegans* at any desired angle with excellent precision. For example, an individual worm was rotated by 4 ° with a 5 millisecond (ms) pulse as demonstrated in Figure 2.17(d). In Figure 2.17(b), a full 360 ° rotation occurs in 60 ms which is ~ 6 times faster than the stepwise rotation in Figure 2.17(d). For precise angular adjustment, a slow rotational rate was preferred. This could be achieved either by adjusting the applied voltage or frequency. In addition, the ARM method can be rendered for high-throughput studies as demonstrated in Figure 2.17(e),(f) Positional stability of the worms during and after the rotational manipulation is also important for better imaging capability. We have observed slight worm drifting events along the channel once the acoustic power was turned off. This was identified as a result of the pressure fluctuations in the microchannel. By careful adjustment of the inlet and outlet tubing length and positions, and designing parallel channels (Figure 2.18) to reduce the effect of minute pressure differences in the microchannel, we achieved a more robust worm positioning once the rotation is halted. In the absence of external liquid flow, the worm remains trapped and rotates in the same location after each cycle. However, during each cycle, the tip of the head of the worm

rotates in an elliptical manner due to its slightly curved shape after the anaesthetic treatment. We tracked the tip of the *C. elegans* head and measured the spatial positions (x and y coordinates) during multiple-cycle rotations, also suggesting that the worm does not drift during rotation (Figure 2.19).

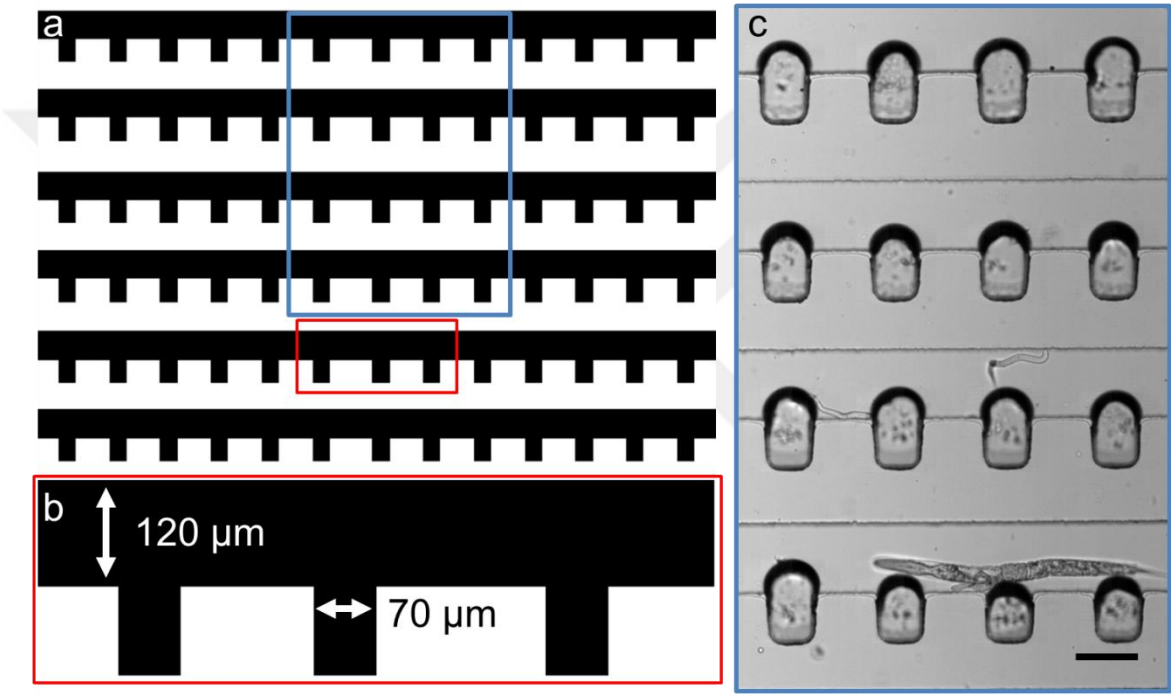

Figure 2.18. Schematic and image of parallel rotation channels. (a) and (b) show the schematic of the parallel rotation device. (c) Optical image of a part of the rotation device (blue rectangle). Scale bar = 100 µm.

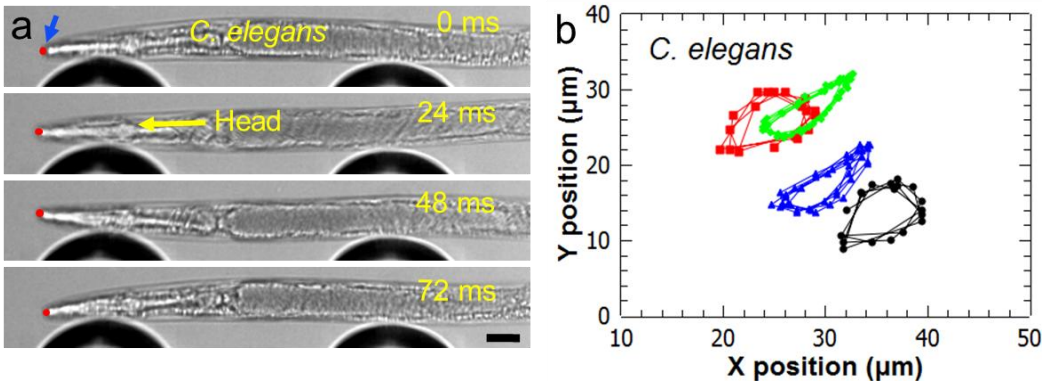

Figure 2.19. Rotation stability analysis for *C. elegans*. (a) Image sequence of *C. elegans* rotation after anaesthetic treatment. Tip of the head (marked by a red dot) is tracked during multiple rotations, and the spatial coordinates are plotted in (b). Error bars represent standard deviation ($n \geq 10$). Scale bar = 25 μm.

2-4-4 Application of the ARM to *C. elegans* developmental studies

We used the ARM method to analyse reproductive system pathology in *C. elegans*. The nematode vulva is a passageway between the uterus and the exterior and is required for egg-laying and mating. A mature vulva is tubular in shape and is formed from 22 epithelial cells that self-organize into 7 concentric rings of unique dorso-ventral positional identity, vulA to vulF (Figure 2.20(a)). We applied ARM to examine the morphological properties of the vulva toroidal rings. We imaged transgenic animals with the adherens junction marker *ajm-1::GFP* (Figure 2.20(b)) in which green fluorescent protein (GFP) localizes to the apical border between toroids, essentially outlining each toroid for visualization [107]. Toroids change shape and position during morphogenesis, and when comparing wild-type and mutant animals it is important to compare similar stages. A particular stage is most easily identified from a lateral view. However, toroid shape is most effectively visualized and compared from a dorsal or ventral view, depending on which toroid is to be examined. We imaged a wild-type animal from the

lateral side, first confirming that the animal was at the mid-L4 stage according to the characteristic vulval morphology, the extension of the gonad arms and the size of the uterine lumen (Figure 2.20(b)). Upon fluorescence imaging along this dorso-ventral axis, as seen in Figure 2.20(c), all the rings appear as parallel lines stacked upon one another. VulA is visible as the space between the two most ventral GFP lines, but minimal information pertinent to morphological properties of vulA, such as shape and size, is evident. Therefore, we applied ARM to rotate the animal in order to observe the complete vulA ring morphology on the ventral side. With a 270 ° ARM rotation, a distinct ring, defining the edge of vulA, was observed closest to the hypodermis, and its characteristic round morphology is evident (Figure 2.20(d)).

RNA interference (RNAi) with NR4A family nuclear hormone receptors *nhr-25* results in abnormal vulval ring formation[108]. We analysed ring morphology in *nhr-25(RNAi)* animals from both the lateral and ventral perspective for the first time. From a lateral perspective, we can identify an animal of appropriate stage, when fusions should be complete (Figure 2.20(e)) and observe that toroids have formed (Figure 2.20(f)). However, only after applying ARM to examine the ring morphologies from a ventral view in the same animal, can we observed an abnormally shaped toroid with defective epithelial junctions (Figure 2.20(g)). The junction between vulA and the hypodermis is abnormally elongated in the lateral plane (arrow) and an abnormally unfused cell (arrowhead) is present. 23% of animals (n=200) have visible toroid shape defects when analysed using ARM.

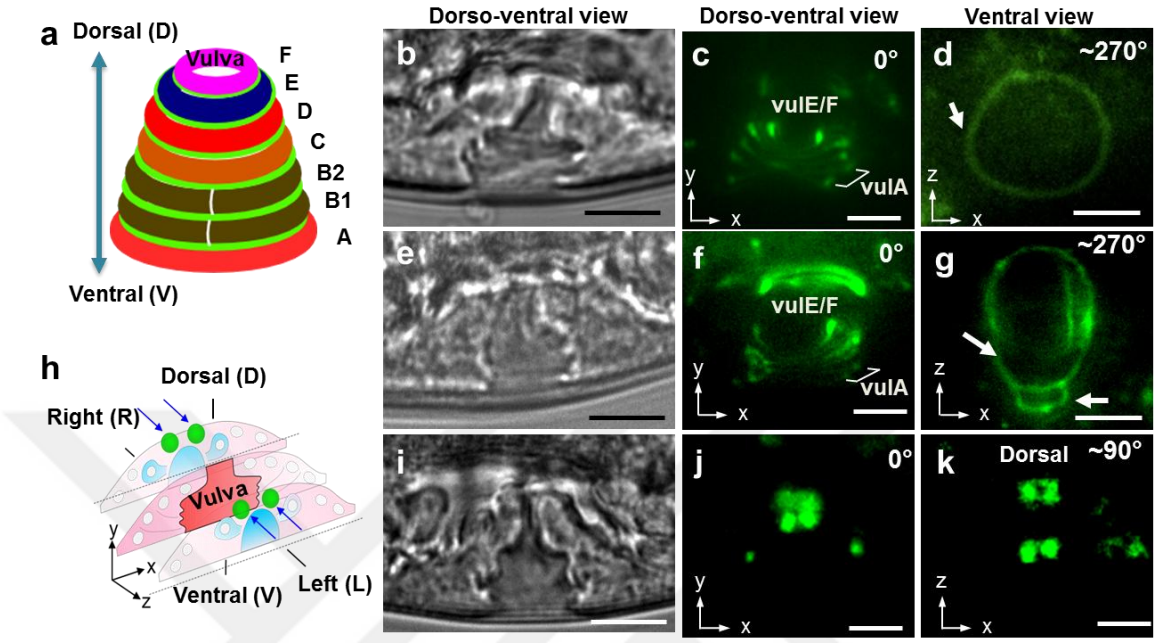

Figure 2.20. Toroid formation and cell position during *C. elegans* reproductive system morphogenesis. (a) A schematic of vulva structure of a *C. elegans* showing 7 concentric toroidal rings, VulA to VulF along the dorso-ventral positional axis, connected by adherens junctions shown in green. Digital image of a vulva of (b,i) a wild-type animal and (e) an *nhr-25(RNAi)* animal. Fluorescence image of toroids created by visualization of the space between *AJM-1::GFP* adherens junction rings in (c) a wild-type and (f) an *nhr-25(RNAi)* animal acoustically driven along the dorso-ventral axis. (d) The ventral view of an ARM rotated worm showing shape and size of border of vulA in wild-type and (g) in *nhr-25(RNAi)* animals. In the *nhr-25(RNAi)* animal, the vulA border is expanded laterally and abnormal adherens junctions (arrows) were seen. (h) A schematic of vulva epithelial cell positions along the left and right axis. Two VulF cells on the right and two on the left shown in green. (j) Dorso-ventral view shows two GFP+ cells. (k) Ventral view obtained through ARM clearly shows four GFP+ cells. Scale bars = 10 μm.

As a further demonstration of the value of ARM, we also examined the expression of a GFP marker with a distinct left and right expression pattern. The Epidermal Growth Factor (EGF) homolog LIN-3 is expressed in the VulF toroid, which is comprised of 2 left-side and 2 right-side vulval epithelial cells[109] (Figure 2.20(h),(i)). The entire *lin-3::GFP* expression pattern was effectively visualized through ARM. Along the dorso-ventral axis only 2 GFP+ cells were clearly seen (Figure 2.20(j)). ARM was applied to

rotate the animal perpendicularly to the ventral position to observe all 4 GFP+ cells simultaneously (Figure 2.20(k)).

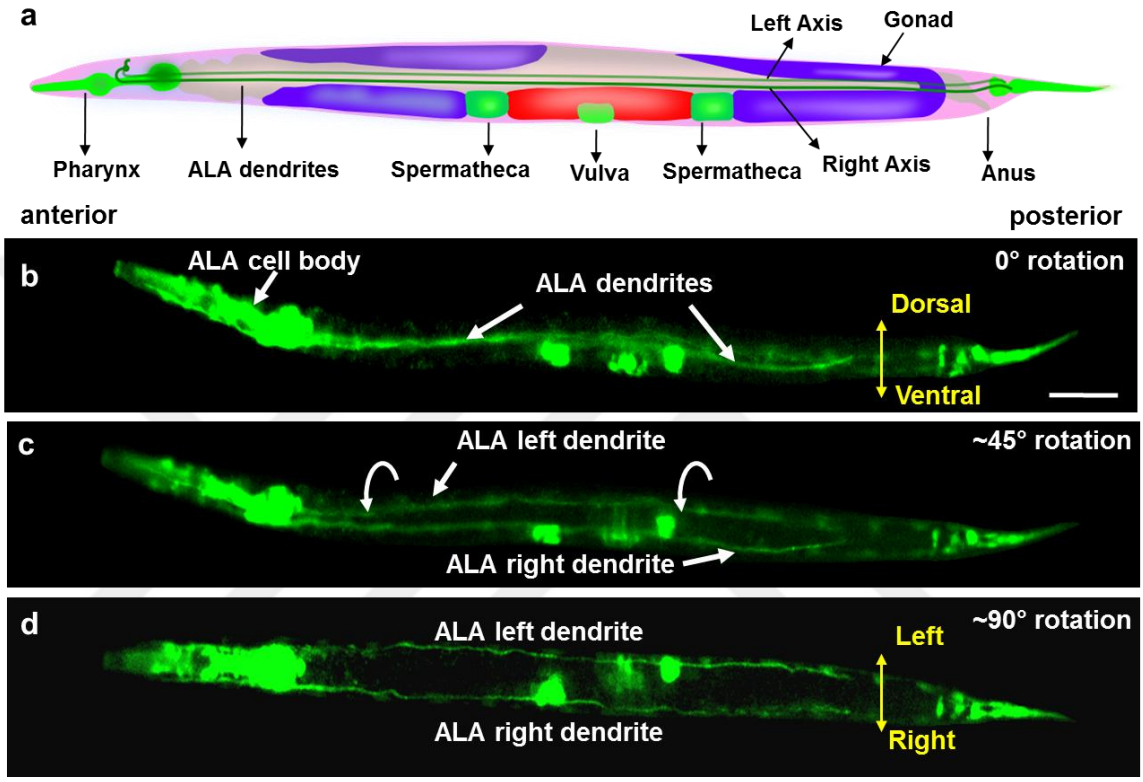

Figure 2.21. Observations of the anatomy of ALA neuron dendrites using rotational orientation. (a) A schematic of *C. elegans* showing anatomy of ALA cell body and dendrites. (b) Fluorescence image of a *C. elegans* showing overlapped, masked ALA dendrites at the dorso-ventral axis. The worm is rotated (c) ~45 °and (d) ~90 °simultaneously exposing the left and right dendrites for observation. Scale bar = 40 μm.

We also used this technique to examine the morphology of the *C. elegans* ALA interneurons using the *ida-1::GFP* transgene, which is expressed in the ALA cell body and dendrites, as well as in other neurons and the spermathecae (*ida*-1::*GFP*)[110]. The ALA cell body extends two dendrites along the left and right axis to the tail of the animal[111] as seen in Figure 2.21(a). At the dorso-ventral axis, it was difficult to distinguish left and right dendrites of ALA due to masking (Figure 2.21(b)). We used the

ARM technology to rotate the animal gradually in two steps of ~45^0 rotation and were able to observe the distinct migratory pattern of the both left and right ALA dendrites (Figure 2.21(c),(d)).

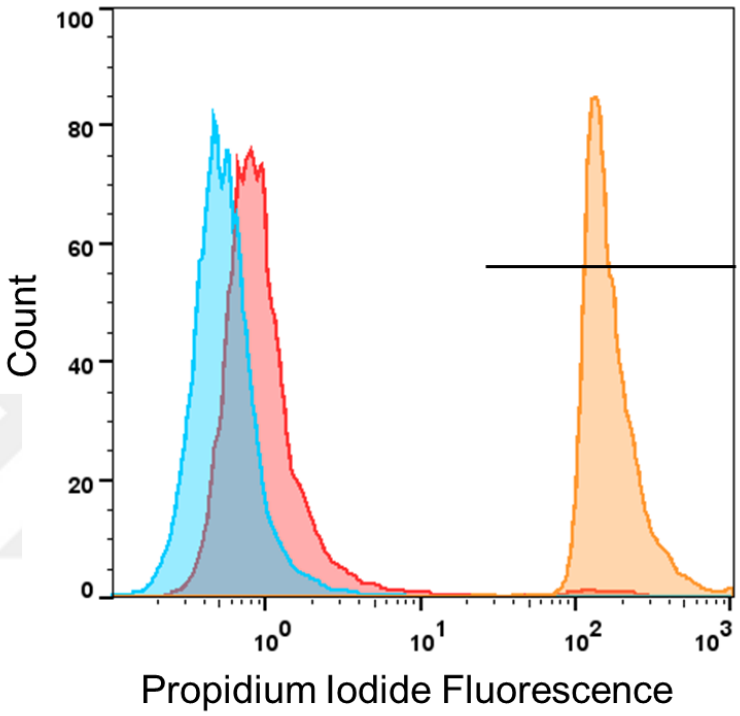

Figure 2.22. Determination of HeLa cell viability. To analyse the viability of cells subjected to the ARM process, unstained HeLa cells were injected into the ARM device and acoustic microstreaming was turned on until each cell passed completely through the device (one to two minutes). These treated HeLa cells were then collected from the outlet, followed by an addition of propidium iodide (PI), which can only bind to cells if the cell membrane is damaged. The cell solution was then subjected to commercial flow cytometric analysis which indicated that 99.2% survival of the acoustically treated (red histogram) HeLa cells. The control experiments included positive control (ethanol treated and PI stained dead HeLa cells; orange histogram), and cells without microstreaming with PI addition (blue histogram). The results show that acoustic microstreaming generated with 15 V_{pp} and 60–100 kHz had no significant detrimental effect on the cells.

2-5 Discussion

ARM provides an excellent platform for a wide range of applications in the biological and physical sciences. The ARM method can trap and rotate microparticles, cells, and organisms in a compact microfluidic device by using oscillating microbubbles in an acoustic field. It is critical that the ARM method is capable of rotating micro-objects regardless of their electrical, magnetic, or optical properties. Our ARM technology shows significant advances in biocompatibility and versatility beyond existing rotational manipulation methods. We have demonstrated the biocompatibility of our method by conducting a HeLa cell viability test, which resulted in a ~99.2% survival rate for the cells after experiencing acoustic field for one to two minutes (Figure 2.22). Viability of cells in acoustic fields primarily depends on the acoustic pressure amplitude or applied voltage, and the heat associated with it. Most acoustic applications pertaining to cells in microfluidics was reported to be biocompatible and safe [9], [112]. Unlike inertial bubble cavitation (where bubbles collapse in the presence of strong acoustic pressure) or high-amplitude strong oscillations, we used stable, low-amplitude bubble oscillations, which require very low acoustic power. Rotation of cells can even be seen at voltage as low as 2 V_{PP} corresponding to approximately ~60 rpm. Thus, low voltage corresponding to low-amplitude oscillations used for rotational manipulation does not damage cells when compared to stronger acoustic bubble cavitations [41], [98]. Controlled rotation of HeLa cells was demonstrated by modulating the oscillation amplitude of the microbubbles. The wide range of angular velocities achieved in rotational manipulation could provide an excellent tool for massively parallel single-cell mechano-biological studies through

arrays of microbubbles within horse-shoe-structures [86], [90], [91] or sidewall cavities. It is an important ability to create physiological conditions to understand how cells react to mechanical forces which is critical in various applications including tissue engineering of vascular cells and heart valves [113], [114].

The ARM technology provides unique advantages for imaging a model organism such as *C. elegans*. During investigations of the ALA neuron dendrites, imaging in general was difficult due to overlapping of GFP patterns; rotation of the worm permitted acquisition of distinct dendrites images in a single animal and allowed access to the neuronal network of the organism. This feature holds great promise for *in vivo* laser microsurgery studies applied in axon regeneration processes, where you can damage multiple neurons at a time and later analyse their regeneration properties with ease [57], [60], [62], [63].

Similarly, we used our method to examine the composition and structure of the *C. elegans* vulva. Rotational manipulation allowed us to categorize mutant worms by analysing the defective cell shape and size comprising the vulval rings. Specimen rotation using ARM is precise, rapid, and more importantly, controllable, thus photobleaching becomes less challenging for fluorescent samples. Furthermore, dynamic rotational positioning and rapid identification of the defective cellular structures can be potentially coupled with on-chip model animal sorting applications. It is also important to note that the ARM chip costs less than $1 in bulk fabrication. The permanent instrument, which includes compact, custom-designed electronics, can be manufactured for under $100. With this inexpensive setup, even low-cost fluorescent microscopes [115], [116] can be used to obtain 3D imaging capability, which makes 3D imaging accessible to many low-

budget laboratories around the world that do not have access to confocal microscopy facilities. The ARM method can be extended to other small organisms by simple design modifications of the microfluidic devices. The ARM method offers rapid and accurate angular adjustment of the cells and organisms. Given the growing use of organism-on-chip tools for investigating small animals, our method is valuable in the field of bioengineering, biophysics, medicine, and developmental biology.

Chapter 3

Acoustofluidic Rotational Manipulation using Oscillating Solid Structures

In this chapter, oscillating solid structures of PDMS sidewall sharp-edges and thin glass slides are utilized in order to generate streaming flows under acoustic excitation. This method is developed as an alternative to the bubble based rotational manipulation method in which acoustic parameters change depending on the microbubble size. In the Introduction section, current literature and brief description of the method is presented. In the Experimental methods section, device design and operation is described. Results section gives the application of the ARM method to rotate HeLa cells, and *C. elegans*. Finally, discussion section summarizes the findings and outlines the potential applications.

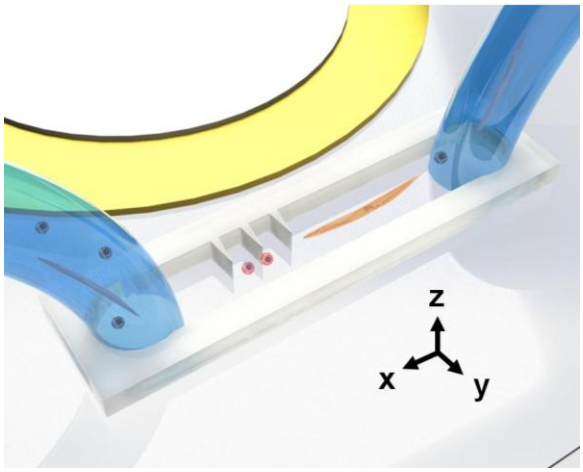

Caption: Cartoon schematic of the acoustofluidic rotational manipulation device based on oscillating solid structures.

3-1 Introduction

Controllable rotational manipulation of microscale objects benefits various fields including single cell diagnostics [55], [56], [117], model organism studies [53], [58], and nanotechnology [74], [77], [78]. For example, in single cells studies, heterogeneity in cell populations necessitates additional capabilities in single cell manipulation in order to acquire comprehensive phenotypic, genotypic and functional intercellular characteristics [118], [119]. Furthermore, in model animal studies including small organism microsurgery and phenotyping, multi-dimensional optical imaging is a crucial facility to obtain precise cellular and subcellular positional identities [11], [52], [57].

Different approaches have been practiced to generate rotational manipulation at microscales [70], [71], [76], [120]–[122]. Optical tweezers were used to rotate birefringent particles and single cells using complex optical setups [70], [72], [123]. Nonetheless, laser generated heating renders the optical methods unreliable for biological samples [73]. Magneto rotation of particles and biological cells require magnetic property which is provided through an additional step of insertion of nanoparticles into the cells [56], [77]. Electric field based methods have also been applied to various nanotubes and single cells but they require demanding special sample and medium properties [75], [78]. For rotational orientation of model organisms, only few methods have been proposed including stepper motors [53], [58] and lateral orientation through predefined microchannel geometries [52]. Rapid operation and dynamic control are advantages of using stepper motors but the technique lacks simplicity, dexterity, and on-chip adaptability. Passively orienting worms using curve channels is highly limited in control,

and lacks the precision in angle of rotation. Recently, we have developed an acoustofluidic based rotational manipulation method utilizing acoustic bubble generated microstreaming flows [25]. Even though this method has various advantages over the existing rotational manipulation technologies, the variation of the acoustic parameters due to the changing microbubble size and geometry is undesired for longer period of operation. Overall, considering the significant progress in organism and cell-on-a-chip applications, there is a need for a robust and simpler method for on-chip rotational manipulation of specimens from single cell level entities to complex model organisms.

Here, I present a microfluidic device utilizing acoustofluidics [26], [43], [124] to generate highly tunable on-chip rotational manipulation of single HeLa cells and model organism Caenorhabditis elegans (*C. elegans*). For this task, I employ steady streaming microvortices generated by oscillating solid structures in an acoustic field where the cells or the organisms are being rotated by the torque generated via the streaming flows. Compared with the existing technologies, the presented acoustofluidic rotation method is robust, biocompatible, independent of optical, magnetic or electrical properties of specimen and adoptable to existing microfluidic platforms.

3-2 Experimental methods

3-2-1 Device design and fabrication

The acoustofluidic rotation devices were designed with sharp-edge and bare channel regions to generate both in-plane and out-of-plane rotational manipulation. For sharp-edge and bare channel regions tip angle, sharp-edge length, sharp-edge period and bare channel width were experimentally optimized as 15°, 200 µm, 150 µm, and 500 µm, respectively (Figure 3.1).

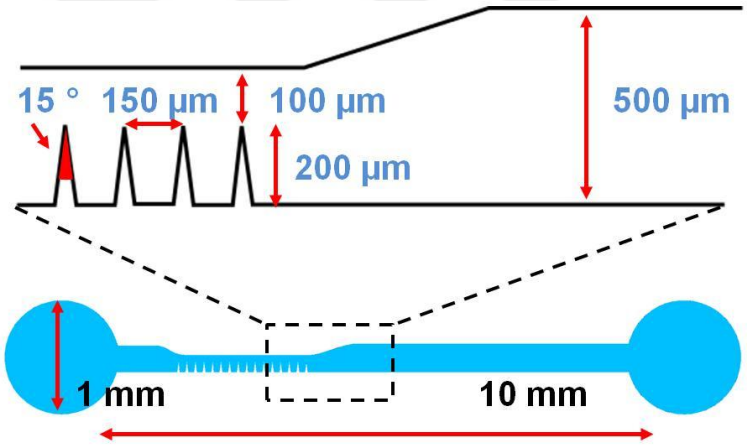

Figure 3.1. Device schematic for the PDMS microchannel features both sharp edge structures and bare regions for in-plane and out-of-plane rotational manipulation, respectively.

The microfluidic device was fabricated using PDMS soft lithography and replica molding technique. For master mold preparation, a silicon wafer was patterned and anisotropically etched using deep reactive ion etching (DRIE) process. The surface of the silicon master mold was treated with silane vapor using 1H,1H,2H,2H-perfluorooctyl-trichlorosilane (Sigma Aldrich, USA) for approximately 1 hour. SylgardTM 184 Silicone Elastomer Base was mixed with SylgardTM 184 Silicone Elastomer Curing Agent (Dow

Corning, USA) at a ratio of 10:1 and cured at 65 ℃ for 2 hours to form the PDMS channels. Once completely cured, inlet and outlet holes were punched into the designated ports of the PDMS micro channel using a hand operator puncher (Harris Uni-Core, Ted Pella, USA). Then, the PDMS channel surface and a 25 x 50 x 0.150 (width x length x thickness) mm glass slide (SuperSlips, VWR, USA) were treated with oxygen plasma for 1 minute, and bonded in 65 ℃ overnight. Finally, a piezoelectric transducer (81-7BB-27-4L0, Murata Electronics, Japan) was bonded on top of the glass slide next to the PDMS channel using an epoxy (84101, Permatex, USA).

3-2-2 Device operation

HeLa cells (5×10^5 ml^{-1}) and *C. elegans* were stably injected into the microchannel trough the inlet tubing using a 1 ml syringe (309659, Becton Dickinson, USA). Preparation of HeLa cells and *C. elegans* were previously discussed elsewhere.[91], [125], [126] For In-plane rotation, once the HeLa cells were positioned in the sharp-edge region, the piezoelectric transducer was driven around 5 kHz with varying peak-to-peak voltages from 10 to 40 V_{PP} using a function generator (AFG 3011, Tektronix, USA) and an RF power amplifier (25A250A, Amplifier Research, USA). The working frequency for in-plane rotation was found to be close to the resonant frequency of the transducer. For out-of-plane rotation, *C. elegans* were positioned in the bare section of the microchannel. Working frequency for this mode of rotation was found to be between 70 and 100 kHz. HeLa cell and *C. elegans* imaging were performed using an inverted microscope (Eclipse TE 2000-U, Nikon, Japan). Images were captured with Photron FASTCAM Viewer (PFV, Photron, USA) connected to a fast camera (Fastcam

SA4, Photron, USA). For fluorescence imaging, a Nikon filter cube (excitation: 470 nm, emission: 515 nm), a CCD digital camera (CoolSNAP HQ2, Photometrics, USA), and a fibre optic illumination system (Intensilight, Nikon, Japan) were used.

3-3 Results and discussion

Figure 3.2(a) shows the cartoon illustration of a polydimethylsiloxane (PDMS) microfluidic device adjacent to a piezoelectric transducer which provides the acoustic field. The PDMS channel features one inlet and one outlet for loading and unloading the samples into the device. Both the microchannel and the piezoelectric transducer are bonded on a glass slide of thickness ~150 μm. The rotational manipulation device consists of side wall sharp-edge structures [46], [94], [127] and bare channel parts (see the Figure 3.1). In a single device, using the same method of acoustic actuation, I aim to generate in-plane (x-y plane) and out-of-plane (y-z plane) rotational manipulation using oscillations of the sharp-edges (Figure 3.2(b)) and the glass slide (Figure 3.2(c)), respectively.

In-plane rotational manipulation of one HeLa cell around the tip of a sharp-edge structure is shown in Figure 3.3(a). The oscillating sharp-edge structures generate two counter rotating microvortices in the surrounding fluid due to viscous dissipation in the microchannel (Figure 3.3(b),(c)). To demonstrate the acoustic streaming generated by the oscillating sharp-edges, we performed numerical simulations, by following an approach similar to the one reported previously [94].

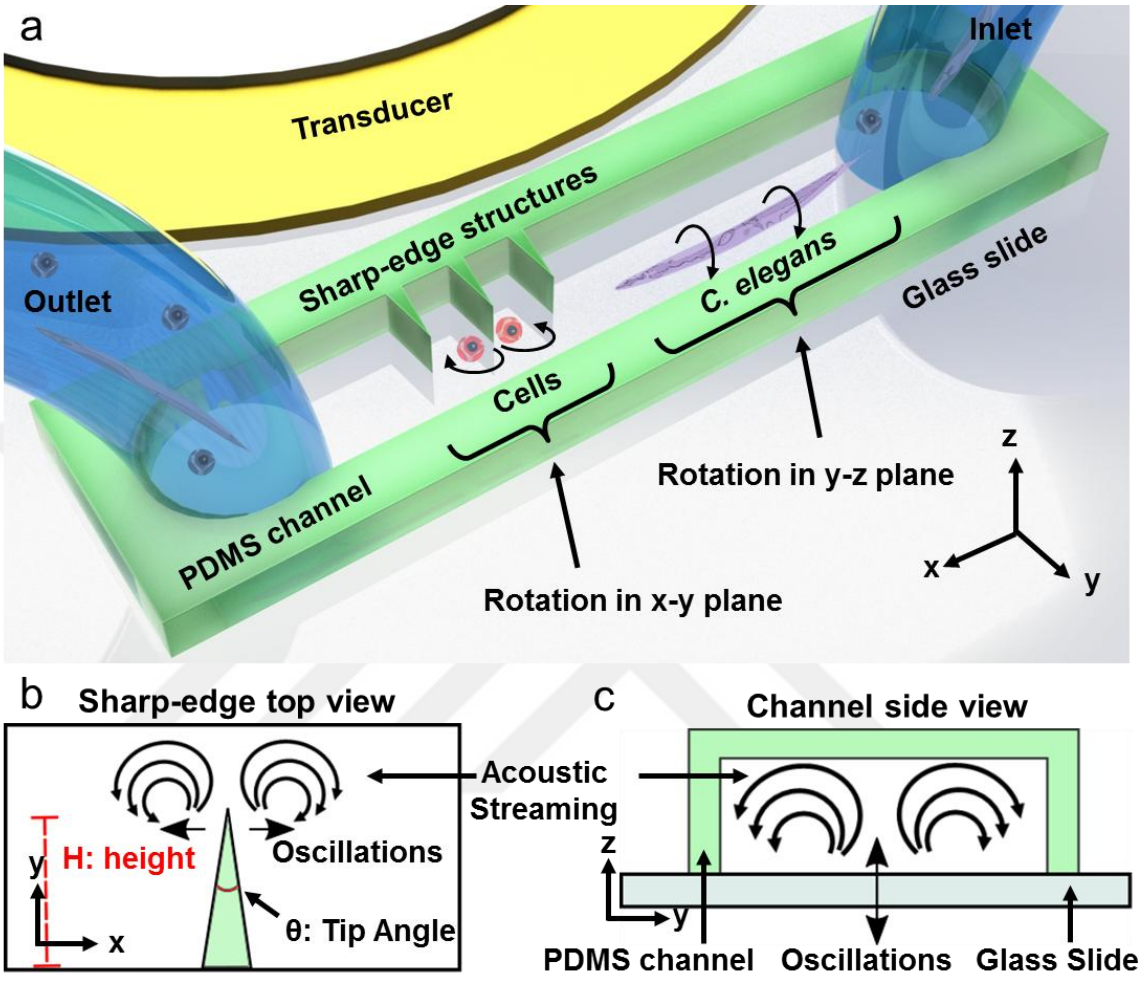

Figure 3.2. Schematic and the working principle of the acoustofluidic rotational manipulation device. (a) A simple PDMS channel contains both sharp edge and bare regions for the cell and worm rotation, respectively. Oscillations of (b) PDMS sharp edge structures and (c) glass slide generate circulating streaming flows that are used for rotational manipulation.

Specifically, we employ a perturbation approach to solve the governing equations (*i.e.* balance of mass and balance of linear momentum) for the motion of a linear viscous compressible fluid, such that the flow variables are split into two parts: (1) the first-order components, which are assumed to be time-harmonic and are indicative of the acoustic response of the fluid, and (2) the second-order components, which are assumed to be time-independent and are indicative of the acoustic streaming response of the fluid. Once

the circulating streaming flows are established, nearby HeLa cells are trapped at the center of the microvortices. Depending on the initial concentration of the cell solution, it is possible to trap and rotate two HeLa cells by one sharpedge structure. Rotation rate of the trapped HeLa cells mainly depends on the peak-to-peak voltage (V_{PP}) applied to the piezoelectric transducer. Oscillation amplitude of the sharp-edge structures also increases with increasing length and decreasing tip angle. Rotational rates of HeLa cells exceeding 14,000 RPM are demonstrated using 15 ° tip angle and 200 μm height for the sharp edge structures (Figure 3.3(d)). As the tip angle was increased to 30 °, the speed of the circulating flows decreased which in turn reduced the rotational speed of the HeLa cells. Height of the sharp edge structures also affects the rotational speeds of the cells; the 100 μm sharp edge structure results in lower rotational speed for the HeLa cells compared to the 200 μm structure with the same tip angle of 30 ° (see Figure 3.4). The flexibility in rotational speed renders this method an excellent tool for single cell studies where shear forces on the rotating cells can be tuned on-demand. In addition, fluid shear stress applied to suspended cells was found to be an important parameter for cell growth rate, volume, and metabolite production [128], [129]. Our on-chip rotational manipulation method can be used in related single cell studies in order to investigate the effect of rotation on cell fate and drug response in variable hydrodynamic shear conditions. Another benefit of using the rotational manipulation in single cell mechanobiology studies is the easy tracking and observation of individual cells thanks to the fixed position rotation at each sharp-edge structure.

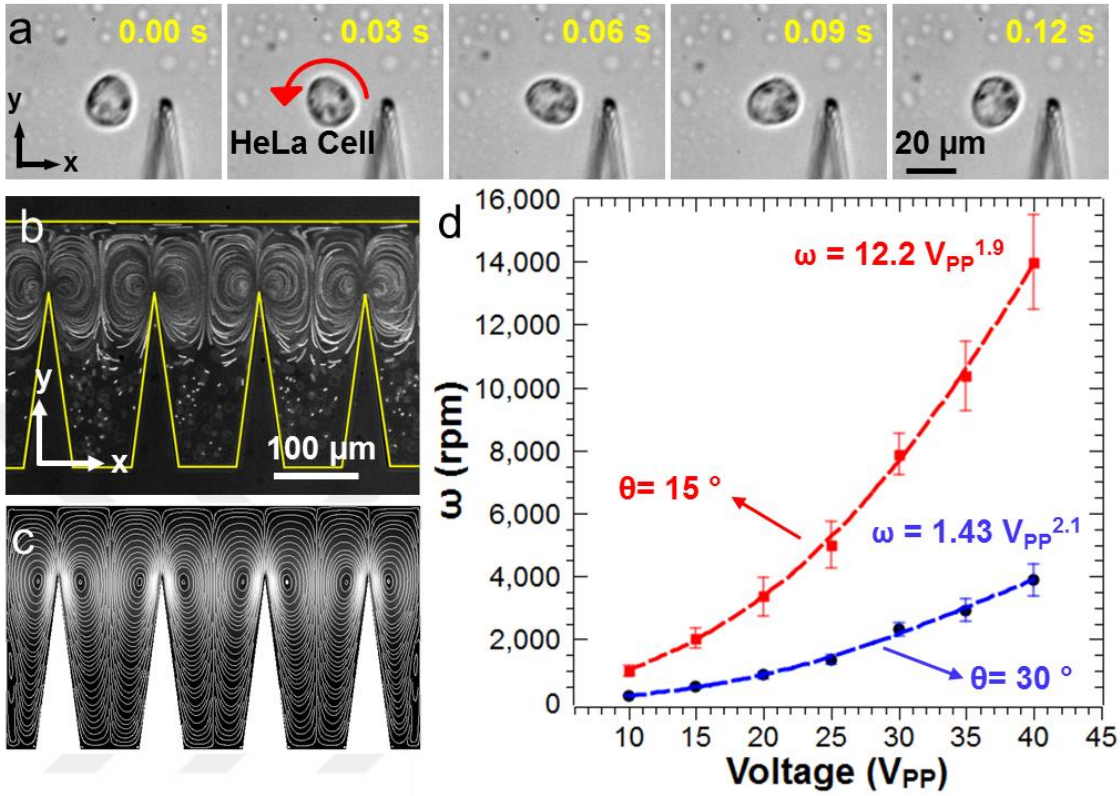

Figure 3.3. In-plane rotation of HeLa cells. (a) The oscillating PDMS sharp edge structure traps and rotates a HeLa cell through acoustic streaming vortices that are visualized (b) experimentally using 1 μm fluorescent polystyrene beads and (c) numerically by a perturbation approach. (d) The rotation rate of the HeLa cells can be tuned by the applied peak-to-peak voltage and the geometry of the sharp edge structures. Smaller sharp edge angles and longer sharp edges yield higher rotation rates.

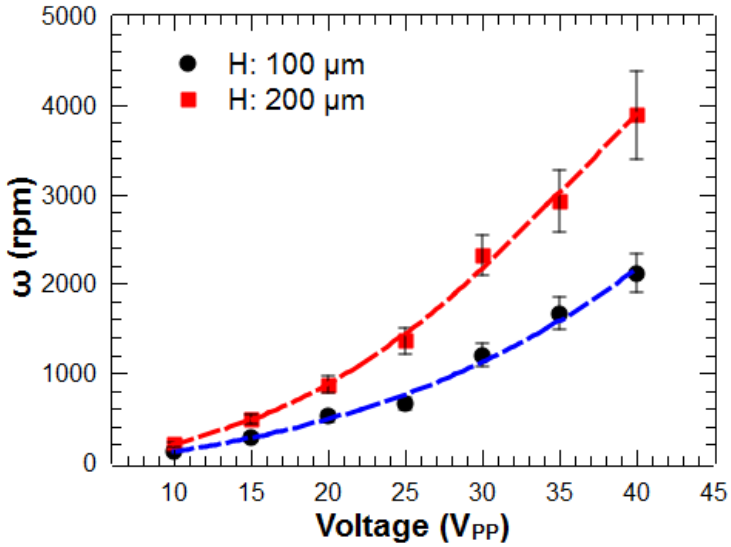

Figure 3.4. Height of the sharp edge structures affects the maximum amount of the tip oscillation which in turn influences the rotational speed of the vortices and the HeLa cells. 200 μm sharp edge structures generates higher rotational speeds for the HeLa cells compared to the 100 μm structures that have the same tip angle of 30 °.

Figure 3.5(a) shows the out-of-plane rotational manipulation of one HeLa cell in the bare section of the microfluidic device at a relative higher driving frequency (~85 kHz) compared to the one used in sharp edge induced in-plane rotational manipulation. Here, the HeLa cell is positioned close the microchannel wall due to the wall effect,[130] and rotated by the torque generated through the out-of-plane streaming flows. The streaming flows generated depend on the different vibrational modes of the glass slide. We performed numerical simulations in order to identify the resonance modes of the glass slide and associated Eigen frequencies. The resonance modes of the glass slide used in the experimental setup is simulated by considering glass as a linear elastic, isotropic material (with fixed ends on both sides) using the commercial finite element software COMSOL Multiphysics 5.1. As shown in Figure 3.5(b), at 86,937 Hz, we observe an

eigenmode where the displacement field is almost purely one-dimensional, with no significant variations along the width and the thickness of the glass slide.

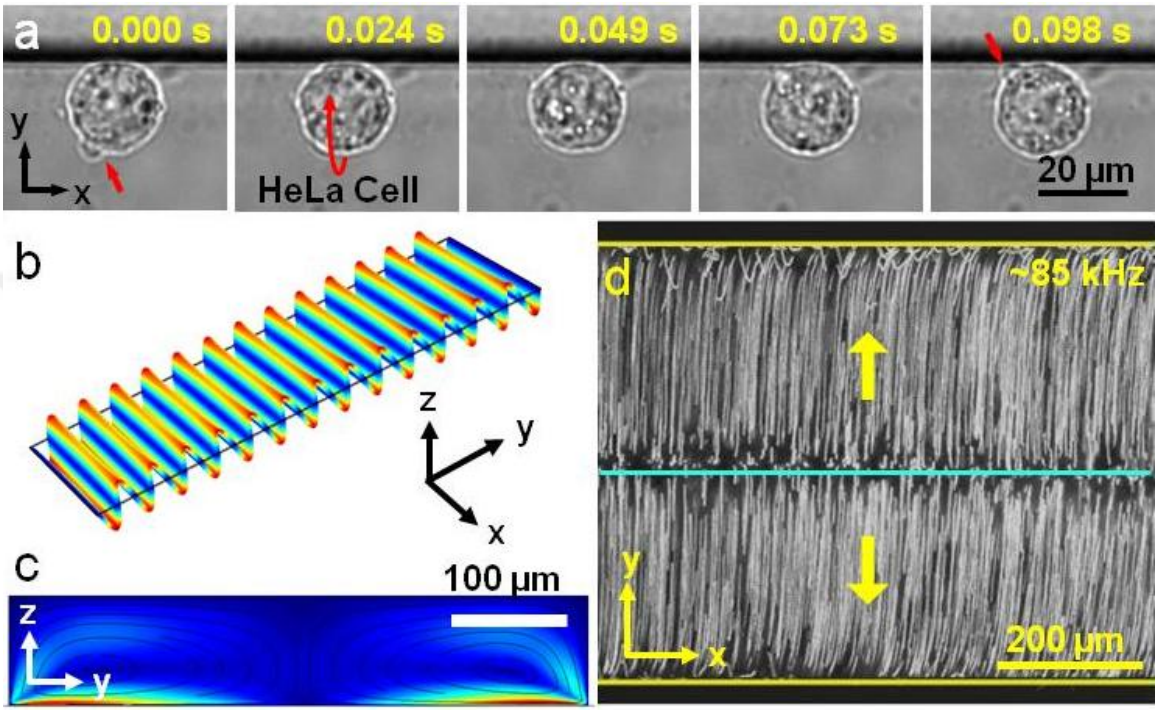

Figure 3.5. Out-of-plane streaming vortices are generated via the oscillating glass slide. (a) Out-of-plane rotation of a HeLa cell is demonstrated at ~85 kHz and 30 V_{PP}, respectively. (b) Numerical simulation of the vibration mode of the glass slide at 86,937 Hz yields parallel displacement lines. (c) Simulated streaming profile reveals two vortices inside the PDMS microchannel that is positioned along the parallel displacement lines on the glass slide. (d) 1 µm fluorescent beads are used to visualize the experimental streaming profile inside the microchannel at ~85 kHz and 30 V_{PP}.

Since I bind the PDMS microchannel parallel to the shorter edge of the glass slide, these displacement lines become parallel to the microchannel as well. This implies that there is no variation of the displacement field along the length of the channel, which is confirmed by our experimental observations where the streaming vortices are seen to be entirely planar (residing in the plane parallel to the width of the channel). The minor variation in the numerically predicted and experimentally employed frequency may be due to the

frequency shift arising out of the viscous damping associated with the loading of microchannel onto the glass slide. We also performed the numerical simulations to observe the streaming field inside the microchannel at this frequency. The glass slide is modeled as a linear elastic solid, while the acoustic streaming patterns inside the microchannel are obtained by using the same approach as employed to perform the numerical simulations for investigating sharp-edge induced streaming, as described earlier [94]. To model the walls of the microchannel, we utilized impedance boundary conditions at the channel walls, while the continuity of velocity and traction is enforced at the fluid-substrate interface. The numerical results obtained (Figure 3.5(c)) are seen to be in good qualitative agreement with the experimental observations (Figure 3.5(d)), both showing the presence of two acoustic streaming vortices along the width of the channel.

It is important to note that since the vibration profile of the glass slide depends on the actuation frequency, a variety of displacement profiles can be generated at the microchannel-substrate interface (see Figure 3.6), depending on the frequency used as well as the orientation and position of the microchannel. Thus, in principle, one can obtain a myriad of acoustic streaming patterns inside the microchannel. We expect that certain modes of the glass slide oscillations in this particular geometry could yield out-of-plane streaming vortices inside the device as shown in Figure 3.5(d). By sweeping the excitation frequency of the transducer, different streaming profiles are investigated. In addition to the parallel out-of-plane streaming vortices, some of more irregular streaming profiles are also observed featuring combination of in-plane and out-of-plane streaming flows (see Figure 3.7). These vortex formations are considered to be the result of more complex vibrational Eigen modes of the glass slide shown in Figure 3.6.

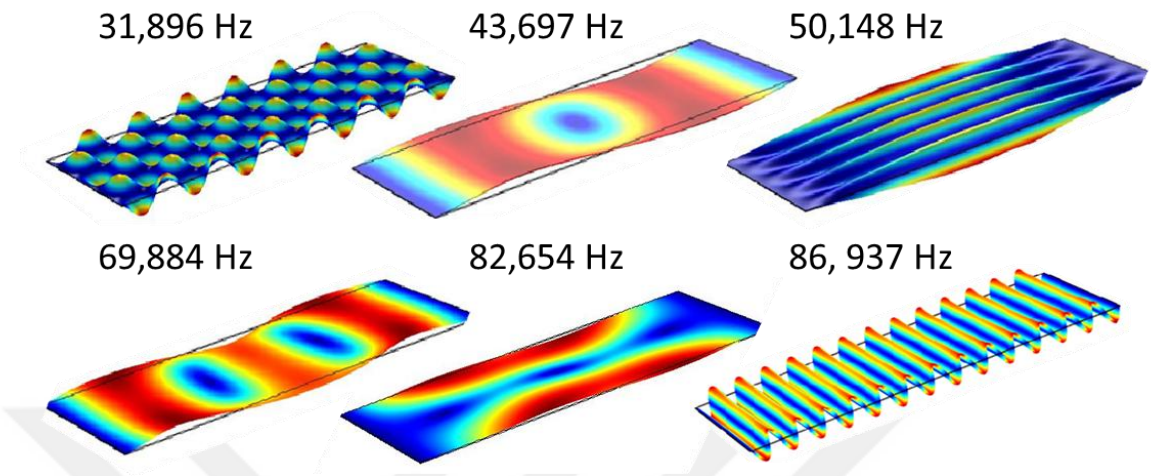

Figure 3.6. Numerical simulation of the glass slide reveals various vibration modes and associated Eigen frequencies. These vibration modes repeat at different frequencies with changing numbers of oscillation maxima and minima.

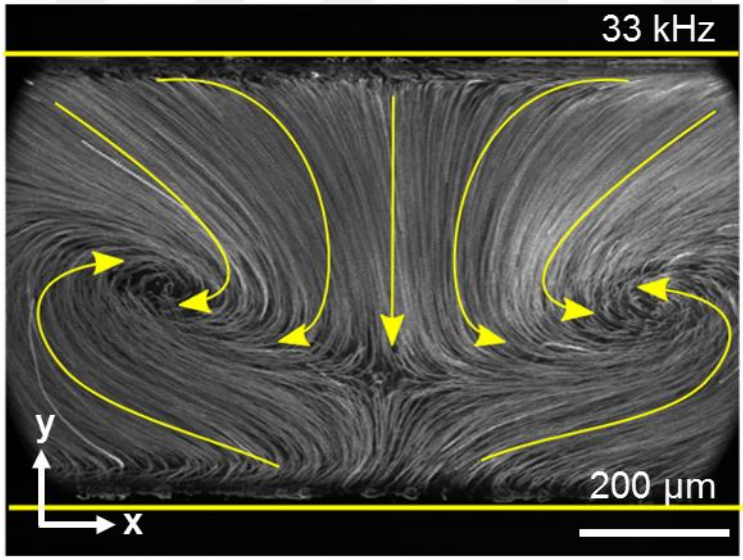

Figure 3.7. Streaming profile inside the microchannel is visualized using 1 µm fluorescent beads at ~33 kHz and 30 V_{PP}. The streaming profile features both in-plane rotating vortices and out-of-plane rotating flows.

Figure 3.8 shows out-of-plane rotational manipulation of *C. elegans.* The *C. elegans* at the developmental stage of late L4 is rotated around its long axis as illustrated in the cartoon schematic in Figure 3.8(a). *C. elegans* are first treated with Levamisole (a widely used anesthetic for worms) to reduce physical activity. Figure 3.8(b) demonstrates a 360 ° rotation of the worm by applying a continuous *RF* sine signal to the transducer. For precisely tuning the angle of rotation, we utilized very short pulses of sine waves from 10 milliseconds to 100 milliseconds (Figure 3.8(c)). Low Reynolds number (Re < 10) inside the microfluidic channel stops the worm as soon as the transducer is turned off. Using this effect, the angle of rotation can be controlled down to 2.5 ° which corresponds to less than 2 μm lateral displacement on the surface of a worm of 40 μm diameter. Worms rotated in the device resume normal activity after they recover from the effect of the anesthetic. As a demonstration of the capability of our rotational manipulation method, we used the method to simultaneously image left/right (L/R) pairs of neurons in the *C. elegans* head. The OLQ cells in *C. elegans* are a set of four mechanosensory neurons consisting of dorsal and ventral L/R pairs. Animals typically position themselves on a microscopy slide so that imaging is done from a lateral view and neurons or other cells with L/R pairs are difficult to visualize simultaneously (Figure 3.9 (a),(b)). By gradually adjusting the rotation angle, we simultaneously imaged all four OLQ cells in the head of a fourth larval stage (L4) *C. elegans* under the standard fluorescence microscopy (Figure 3.9 (c),(d)). Such imaging capability is advantageous for easily scoring differentiation or cell death decisions, for example, within a cell type.

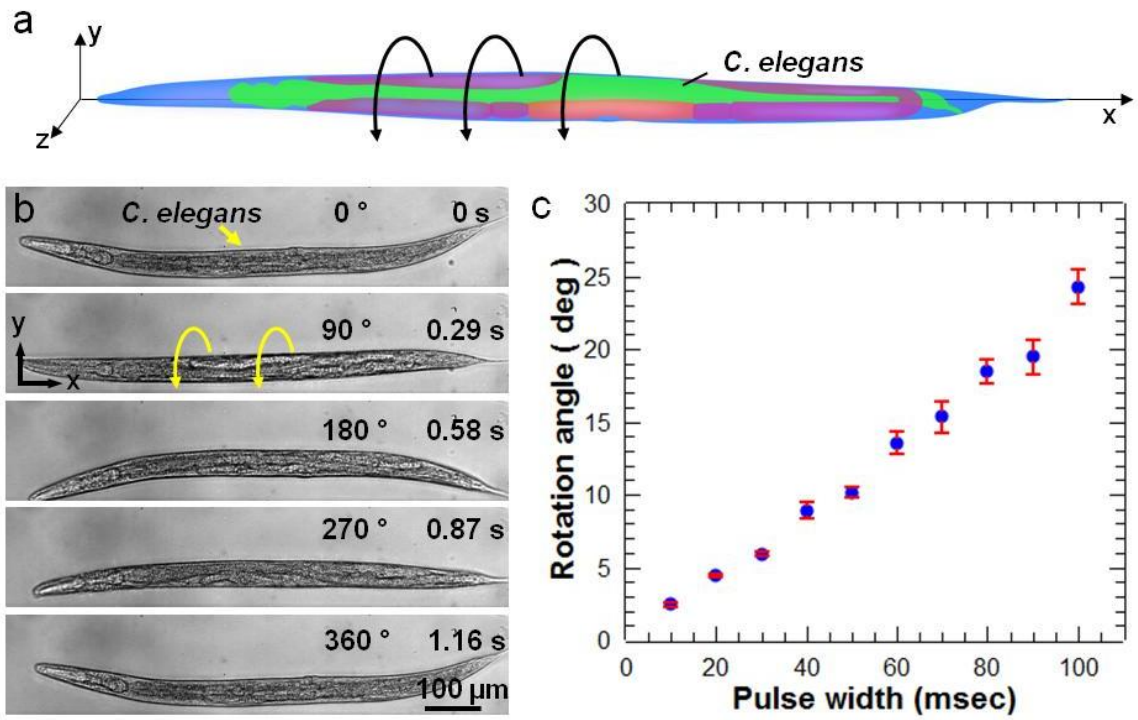

Figure 3.8. Out-of-plane streaming vortices are generated via the oscillating glass slide. (a) Out-of-plane rotation of a HeLa cell is demonstrated at ~85 kHz and 30 V_{PP}, respectively. (b) Numerical simulation of the vibration mode of the glass slide at 86,937 Hz yields parallel displacement lines. (c) Simulated streaming profile reveals two vortices inside the PDMS microchannel that is positioned along the parallel displacement lines on the glass slide. (d) 1 µm fluorescent beads are used to visualize the experimental streaming profile inside the microchannel at ~85 kHz and 30 V_{PP}.

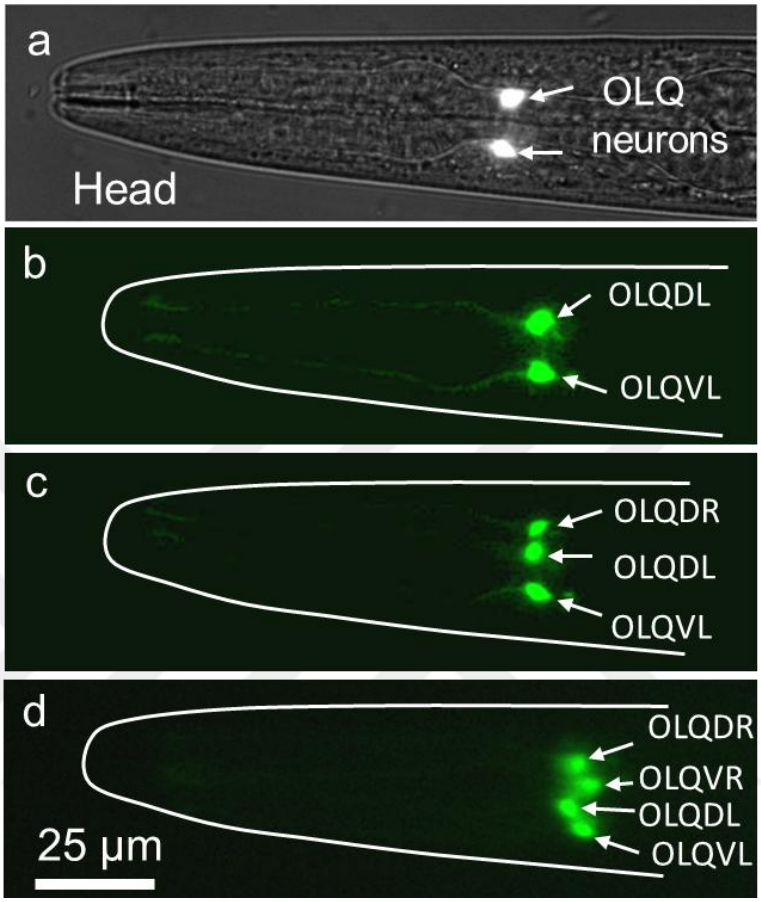

Figure 3.9. Observation of OLQ head neuron cells of an L4 stage *C. elegans* (a) Brightfield and fluorescence images of *ocr-4*::GFP transgenic animal are overlapped in order to show the position of (b) the OLQ dorsal L (OLQDL) and ventral L (OLQVL) neurons in the head of the worm. By rotational adjustment, the paired R OLQ neurons are gradually visualized simultaneously: (c) OLQDL, OLQVL and OLQDR, and (d) OLQDL, OLQVL, OLQDL and OLQDR.

3-4 Conclusion

In conclusion, I have demonstrated precise in-plane and out-of-plane rotational manipulation of single HeLa cells and *C. elegans* using acoustic microstreaming flows generated by oscillating sharp-edge structures and glass slide under the microchannel. Dynamic control of rotational manipulation is achieved using short pulses of sine waves to adjust the angular position. The OLQ neuron cells located in the head of an L4 stage *C.*

elegans are observed through the rotational manipulation. Using sharp-edge structures, single cell rotation rates exceeding 14,000 rpm are realized. As a potential application, effective tailoring of the rotational speed can be utilized to apply adjustable shear forces to single cells. Furthermore, out-of-plane rotation of single cells and model organisms like *C. elegans* is an indispensable tool for comprehensive bio-imaging capabilities. Our acoustofluidic rotational manipulation device is simple-to-fabricate and easy-to-operate that can also be integrated into the existing microfluidic laboratories [53], [131]–[133] designed for handling cells and small model organisms.

Chapter 4

An acoustofluidic micromixer via bubble inception and cavitation from microchannel sidewalls

In this chapter, an acoustofluidic based high viscosity fluid mixer is developed. The high viscosity fluid mixer takes advantage of acoustically induced transient microbubble streaming and cavitation events which generate mass transport in order to break the laminar flow profile. In the Introduction section, micro-mixer literature and brief summary of the methods is presented. In the Experimental methods section, device design and operation is described. Results section demonstrates high viscosity PEG solution mixing and characterization. In the conclusion, advantages of the presented method are discussed and potential applications are outlined.

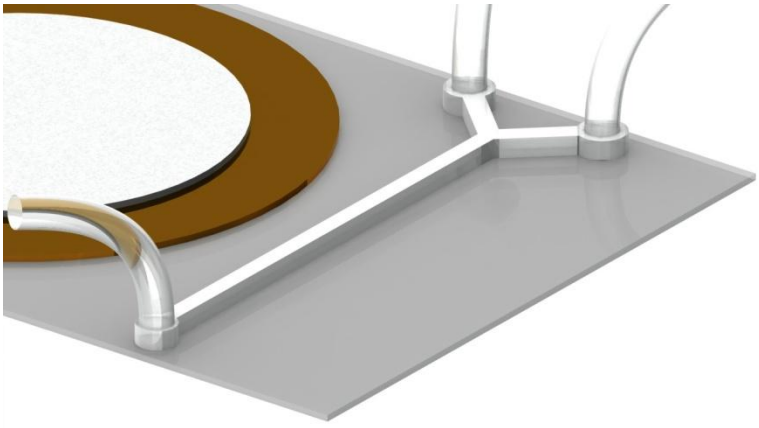

Caption: Cartoon schematic of a straight microfluidic channel used for acoustofluidic fluid mixing.

4-1 Introduction

Effective mixing of high-viscosity liquids is important in many fields including chemical synthesis [134]–[136], biochemical reactions [137]–[141], and clinical diagnosis [142]–[145]. For example, to study the functions of bio-macromolecules in living cells, substrates and enzymes/proteins need to be dissolved in high-viscosity liquids and homogenously mixed before the enzymatic reaction takes place[144]. In the context of clinical diagnostics, high-viscosity body fluids, such as sputum[146], plasma [145], or semen [147], have to be mixed with chemical reagents and/or buffers before performing analysis. In these applications, microfluidic platforms offer many advantages such as small sample/reagent consumption, rapid and high-precision analysis, and low-cost devices [1], [148]. On the other hand, achieving effective mixing of viscous samples in microfluidics is challenging due to the extremely low Reynolds number (high viscosity and small channel dimensions) [149]–[153].

In the last decade, various microfluidic mixers have been developed. These mixers utilize passive approaches, such as chaotic advection [154]–[161], as well as active approaches, such as thermal [162], optical [163], magnetic [164]–[166], electrokinetic [167]–[169], hydrodynamic [170], [171], and acoustic-based [86], [127], [172]–[178] mixing. However, few of these methods have demonstrated the ability to mix high-viscosity fluids [179], [180], and their performance is often less than optimum. For example, Li *et al*. used a passive mixer to mix high viscosity solutions (the highest viscosity is 35.25 mPa.s) with a low viscosity borate buffer solution [180]. The Reynolds number that a complete mixing occurred in their work

was reported as 73.27. Wang *et al.* used an acoustic field to generate and oscillate bubbles in circular-geometry channels and induced mixing of water-glycerol solutions, but the mixing was slow (mixing time: 2−4 seconds) [179]. In this regard, it is essential to develop a new class of microfluidic mixers that can achieve effective, fast mixing with simple devices and experimental setups.

In this dissertation, I present an acoustofluidic method that takes advantage of the wavy structures in polydimethylsiloxane (PDMS) microchannels made from silicon molds fabricated from the deep reactive ion etching (DRIE) process. Our method exploits the surface roughness of the PDMS microchannel sidewalls to incept and cavitate bubbles in the presence of acoustic waves to achieve rapid mixing of two viscous fluids with excellent homogenization. It achieves high-performance, fast mixing of high-viscosity fluids without involving any complex device designs or experimental setups. With its simplicity and high performance, the acoustofluidic micromixer presented here could become a valuable component in many lab-on-a-chip applications.

4-2 Experimental methods

PDMS microchannels with width, depth, and length of 240 μm, 155 μm, and 1.2 cm were fabricated using standard soft lithography and replica-molding techniques [181]. The microchannel was treated with oxygen plasma and bonded onto a Petri dish. An acoustic transducer (APC, Mackeyville) was bounded on to the same Petri dish using epoxy, and placed adjacent to the microchannel. Acoustic waves were generated by the

transducer driven by a function generator (Hewlett Packard 8116A) and amplified by a power amplifier (Amplifier Research 100A250A). The whole setup was mounted on a Nikon TE-2000U optical microscope stage. Different flow rates ranging from 1 μL/min to 30 μL/min were used in the experiments. Deionized (DI) water and fluorescein dye solution were first used for proof-of-concept characterizations. Following that, PEG solutions (molecular weight: ~700 Da) of various viscosities (21.2–95.9 mPa.s) and DI water were used in the mixing experiments. In all of our experiments, the frequency and voltage applied were fixed at 38.9 kHz and 130 V (peak to peak), respectively. Optimum frequency for mixing was found by sweeping the frequency, and observing cavitation behavior in the channel. For high-viscosity experiments the flow rate was fixed at 8 μL/min.

4-3 Working mechanism

The operating mechanism of the acoustofluidic mixing device is shown in Figure 4.1. The PDMS microchannel is made from a silicon mold that is patterned by photoresist followed by DRIE. DRIE process achieves vertical etching via cycles of etching of silicon and deposition of an inert passivation layer to minimize lateral silicon displacement. Duration of each cycle determines the roughness of the walls of Si channels (shorter cycles result in smoother walls). As a result of the DRIE process, the sidewall of the silicon mold features wavy structures (inset in Figure 4.1(a)). These wavy structures of the silicon mold are subsequently transferred to the PDMS channel by the replica-molding process. The rough surface of the PDMS sidewalls develops voids when

a liquid is injected into the PDMS channel. These voids form stabilized cavitation nuclei when an acoustic field is applied in the liquid [182]. Acoustic waves consist of compression and expansion cycles. During the expansion cycle, the diffusion boundary layer of the bubbles becomes thinner, and the surface area of the bubble gets larger. As a result, gas is transferred into the bubbles from the surrounding fluidic media. Depending on the flow rates and the viscosity of the fluid, we have observed both steady and unsteady cavitation in the devices. With low flow rates, bubbles frequently emerge and disappear from the channel sidewall, suggesting unsteady cavitation. During this process, bubbles grow in expansion cycles until they become unstable and eventually collapse in the next compression cycle [183].

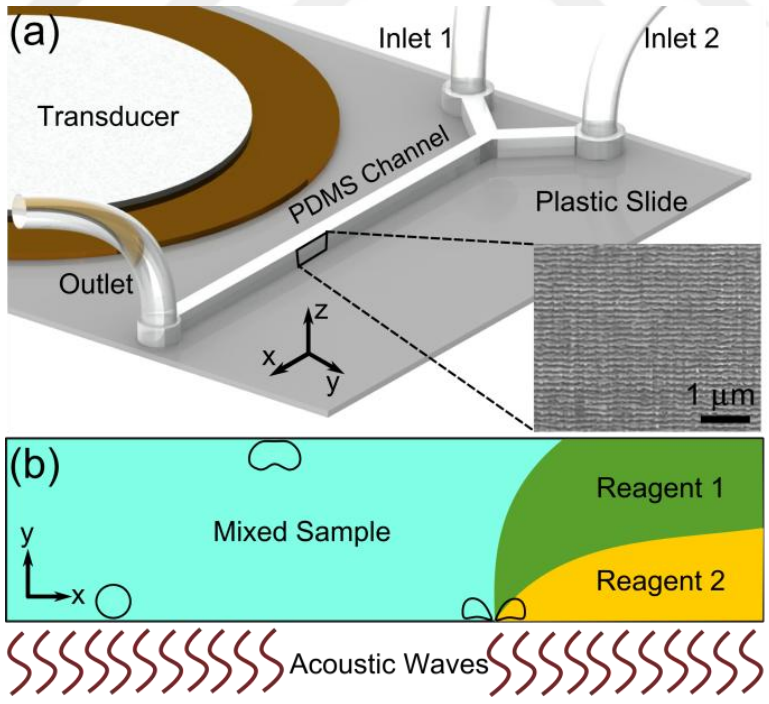

Figure 4.1. Cartoon schematic of the device and mixing process. (a) Diagram of the microfluidic channel with the SEM image of the silicon master mold. The wavy structures are transferred onto the PDMS channel sidewall. (b) Cartoon representation of the mixing of two reagents when the bubble along the sidewall of the microfluidic channel collapses in the presence of acoustic waves.

Two reagents flowing side-by-side in the channel mix by the induced mass transport via the bubble cavitation from the sidewall.

The left panel of Figure 4.2 shows the modes of a single-bubble collapse near a boundary. As the bubble collapses, jetting and counter-rotating vortices occur. Zwan *et al.* estimated that the center of each vortex rotates at a rate of 10,000 rev/s[185]. These fast-rotating vortices break the laminar flow, enabling homogenous mixing instantaneously. Figure 4.1(b) shows a cartoon representation of microfluidic mixing by bubble cavitation from the channel sidewall.

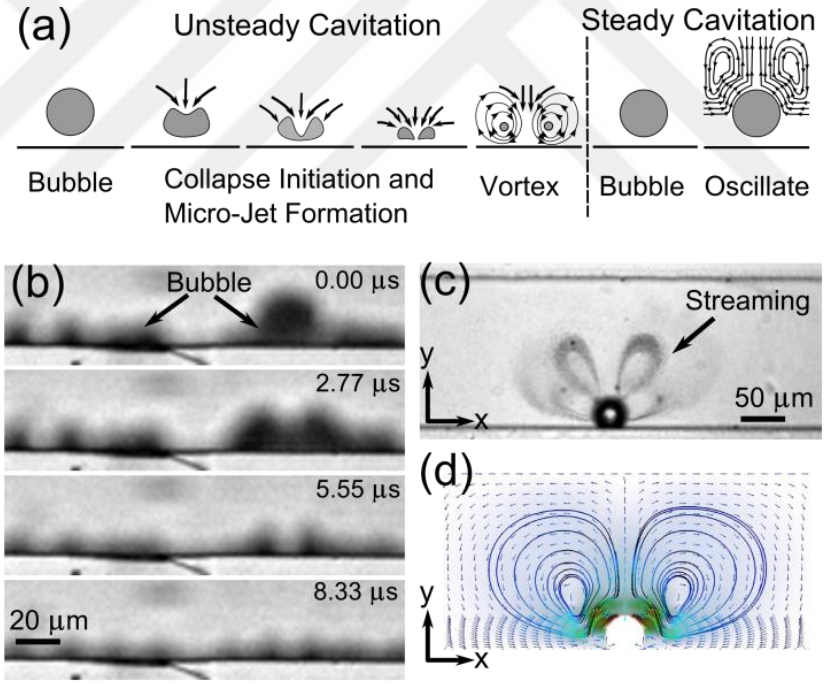

Figure 4.2. Working principle of cavitation mixing. (a) Unsteady cavitation (left panel): modes of bubble collapse near a boundary in presence of acoustic waves. Micro-jet and counter-rotating vortices are created in the final stages of the collapse. Steady cavitation (right panel): micro-streaming phenomenon. (b) Optical images of a bubble's unsteady cavitation captured by the fast camera at 360000 fps. (c) Optical images of a bubble's steady cavitation captured at 5000 fps (*i.e.*, microstreaming of a bubble visualized by micro-beads). (d) Simulated streamlines from theory.

At high flow rates (≥30 μL/min), steady cavitation is prevalently observed. During this process, the bubble membranes oscillate vigorously (both harmonics and sub-harmonics are observed), which gives rise to microstreaming [97], [186]: pressure and velocity fluctuations in the surrounding fluid (Figure 4.2(a),(b) and the right panel on Figure 4.2(a)). The flow patterns in Figure 4.2(d)were obtained using an in-house finite element code based on the perturbation approach similar to that by Koster [187]. The streaming phenomenon breaks the fluidic interface and enhances the mass transport of fluids, thus inducing mixing. At high flow rates bubbles do not collapse since higher acoustic pressure is needed to counter-balance the rise in pressure associated with fluid flow inside the microchannels.

4-4 Results and discussion

To demonstrate the inception and cavitation of bubbles from the PDMS microchannel sidewall, DI water was injected into the channel using a syringe pump (KDS-210, KD Scientific). Figure 4.2 shows the top view of a bubble-collapsing sequence occurring at the boundary. The bubble grew to a critical size of approximately 20 μm on the sidewall, and then collapsed. The critical size is defined by the Rayleigh-Plesset equation, and gives the maximum size before the bubbles collapse. Along the channel, as the bubbles collapsed, they were fragmented into tiny bubbles. Due to the smoother surfaces of the top and bottom of the microchannel, bubble inception or cavitation was observed only on the channel sidewalls, but not on the top or bottom surfaces. Based on atomic force microscopic (AFM) images, the

root mean square (rms) of the top surface, bottom surface, and sidewalls of the microchannel was determined to be 2.2 nm, 23 nm, and 100 nm, respectively. These results are congruent with the fact that the inception and cavitation of bubbles were observed only from the sidewalls. They also agree well with the report from Arora *et al.* [188] which demonstrated cavitation from the corrugated surface of acrylic polymer particles and none from a smooth one.

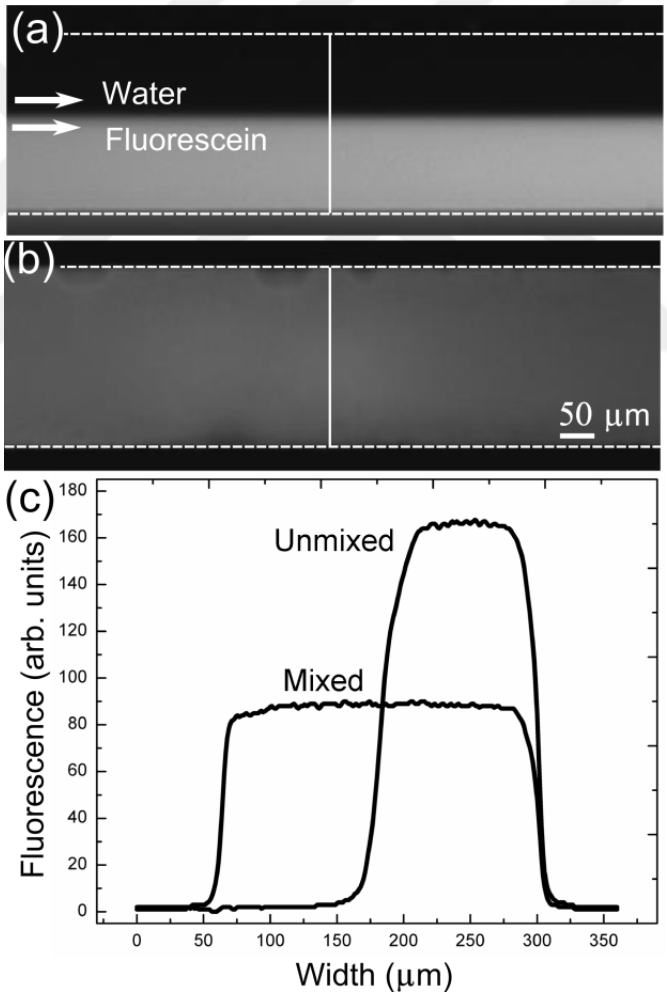

Figure 4.3. Mixing demonstration with water and fluorescein solution. (a) Laminar flow of DI water and fluorescein dye in the absence of acoustic waves. (b) Homogenized mixing in the presence of acoustic waves. (c) Fluorescence plot across the channel width (vertical lines in (a) and (b)) before and after mixing.

To demonstrate effective mixing, water and fluorescein dye were injected at the same flow rates inside the micro-channel. Figure 4.3 show the side-by-side laminar flow of two fluids at 13 μL/min in the absence and presence of acoustic waves, respectively. The mixing results were quantitatively studied by measuring the gray-scale values of the images, a good indicator of the fluorescein dye concentration in the channel (Figure 4.3(c)). The dye concentration profile before and after mixing was measured. The intensity profile shown in Figure 4.3(c) indicates no mixing of fluorescein dye and DI water when the acoustic transducer is off. The average intensity of the fluorescein concentration before mixing was measured to be 164.3 arbitrary units. Once the transducer was switched on, bubbles appeared to incept and cavitate from the sidewalls, inducing rapid mixing (Figure 4.3(b)) and resulting in a uniform gray-scale distribution across the channel width (Figure 4.3(c)). Mixing occurs via a combination of steady and unsteady cavitations. The average intensity after mixing was measured to be 87.6 arbitrary units, suggesting homogenous mixing of the two fluids. The mixing time was estimated from various trials using a fast camera (Fastcam SA4, Photron, at 20,000 frames per second) to be 10 to 50 msec.

During the operation, we also observed micro-bubbles moving along the microchannel, which contributes to the mixing via microstreaming and cavitation of smaller bubbles shooting into the fluid. In Figure 4.4, a bubble that was generated elsewhere in the channel propelled with the burst of smaller bubble fragments. Depending on the position of these bubble bursts, the bubble moved along the channel

in a certain direction. First it moved upstream with an average velocity about 58 mm/s (Figure 4.4(a)-(d)), then localized with smaller-amplitude movements with constant streaming and cavitation events (Figure 4.4(d)), and finally started moving downstream (Figure 4.4(e)). These mobile bubbles can enhance the mixing, especially in regions where bubble inception is not frequent.

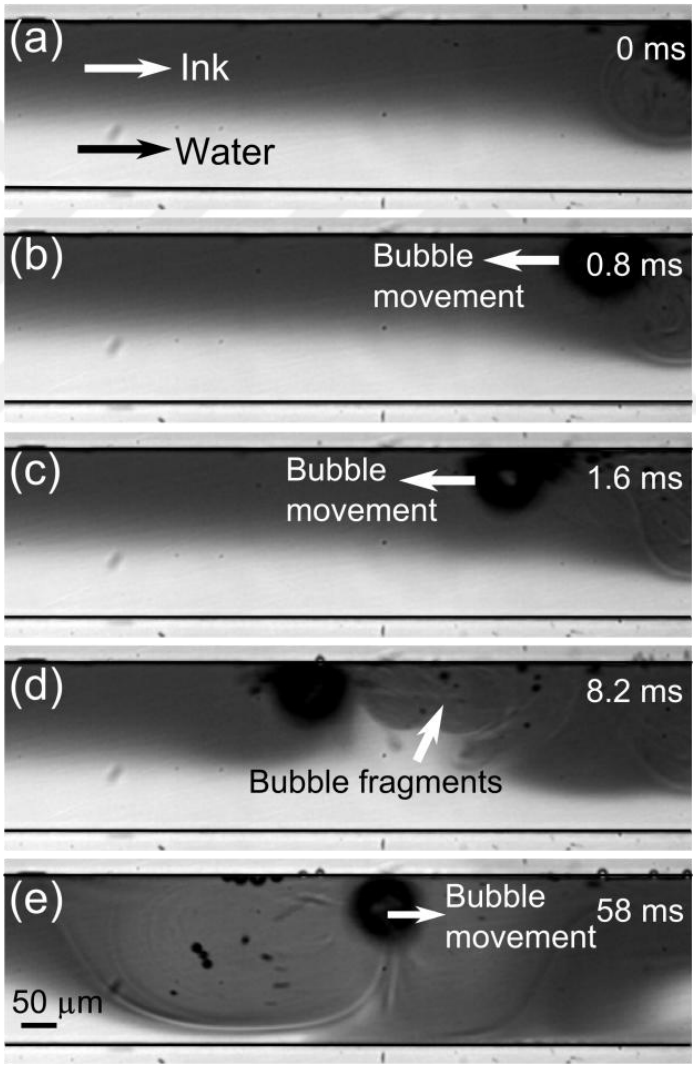

Figure 4.4. Mobile microbubbles propelling along the channel. (a)-(d) A microbubble is moving in the channel against the fluid flow via small fragmentations from the right side of the bubble. (e) Acoustic streaming and further smaller bubble cavitations help mixing, and then the bubble propels to the right by fragmentations from the left side of the bubble.

Table 4-1. Dynamic viscosity of DI water–PEG700 mixture solutions at 25 ℃. μ_2 indicates the viscosity of PEG solution with the given concentration injected from the second inlet, and μ_{mixed} indicates the viscosity of the mixed solution. μ_1 is fixed at 34.2 mPa.s.

PEG700 (volume %)	μ_2 (mPa.s)	μ_{mixed} (mPa.s)
50	18.3	21.2
63	24.5	27.9
67	34.2	34.2
71	41.7	37.7
77	48.8	41.7
83	65.3	47.1
90	77.3	48.8
100	95.9	55.8

Mixing performance of our acoustofluidic mixing device was further examined using various ratios of DI water and PEG700 solutions. We measured dynamic viscosities of the PEG solutions (Table 4-1). For all the PEG solutions the flow rate was fixed at 8 μL/min. 67 % PEG-water solution (viscosity: 34.2 mPa.s) was injected from one inlet, and was kept the same for all experiments (Figure 4.5). The second inlet was used for injecting varying concentrations of PEG solutions. Mixing efficiency (M) was calculated according to the following equation [180]:

$$M = 1 - \frac{\sqrt{\frac{1}{n}\sum (I_i - I_m)^2}}{I_m} \qquad 4\text{-}4$$

where M is the mixing efficiency, n is the total number of points, I_i is the intensity at each point, and I_m is the average intensity. For the perfectly mixed fluids, M is 1 and for the unmixed fluids M is 0. A mixing efficiency of 0.9 or above indicates excellent mixing, and a mixing efficiency between 0.8 and 0.9 indicates acceptable mixing. Figure 4.5(e) shows mixing results for 8 different viscosity values (50% - 100% PEG concentration

used in the second inlet). As shown in Figure 4.5(b)-(d), two PEG solutions were mixed with very uniform intensity profiles. Bubbles emerging from the sidewalls are also visible in Figure 4.5(b)-(d). When I used 90% PEG solution with 77.3 mPa.s (86.8 times higher than water) in the second inlet, a mixing efficiency of 0.92 was achieved. Viscosity of the mixture of 67% (in the first inlet) and 90% (in the second inlet) PEG solutions was measured to be 48.8 mPa.s, which is 54.9 times higher than the viscosity of water (0.89 mPa.s). The Reynolds number (Re) for the mixed fluids was calculated to be 1.14×10^{-2} which is significantly lower than the Re number reported in the previous high viscosity mixing studies[179], [180]. With 100 % PEG solution (final mixed viscosity: 55.8 mPa.s), the mixing efficiency was 0.88 and the mixing time was less than 100 msec.

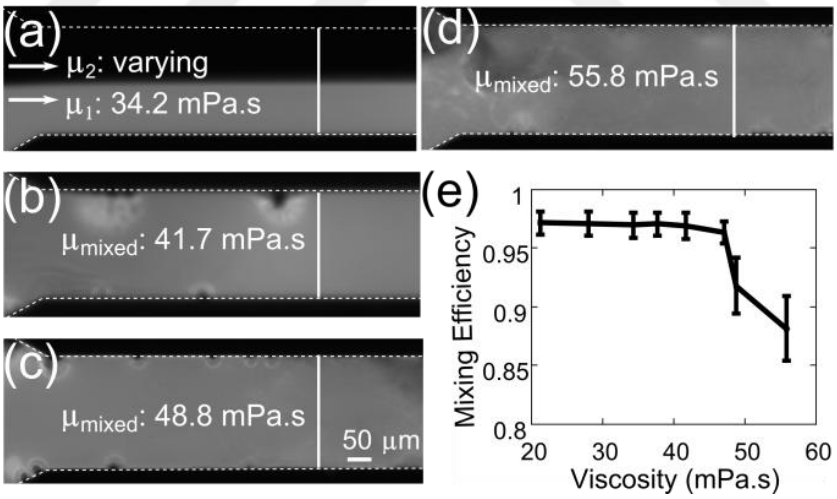

Figure 4.5. Mixing results for high viscosity solutions. (a) Laminar flow of the unmixed PEG solutions where the inlet 1 was kept at a constant viscosity of 34.2 mPa.s. (b) Mixed solutions with μ_{mixed}: 41.7 mPa.s, (c) 48.8 mPa.s, and (d) 55.8 mPa.s. (e) Plot of the mixing efficiency versus dynamic viscosity.

I also characterize mixing performance of the acoustofluidic micromixer along the z-direction (Figure 4.6). For these experiments, the PEG solution with a viscosity 65.3

mPa.s was injected from inlet 2, and the PEG solution with a viscosity of 34.2 mPa.s was injected from inlet 1. Snapshots from the bottom, middle, and top planes were captured before and after the cavitation mixing started. The intensity profiles were plotted to prove homogenous mixing along the z-direction in the channel.

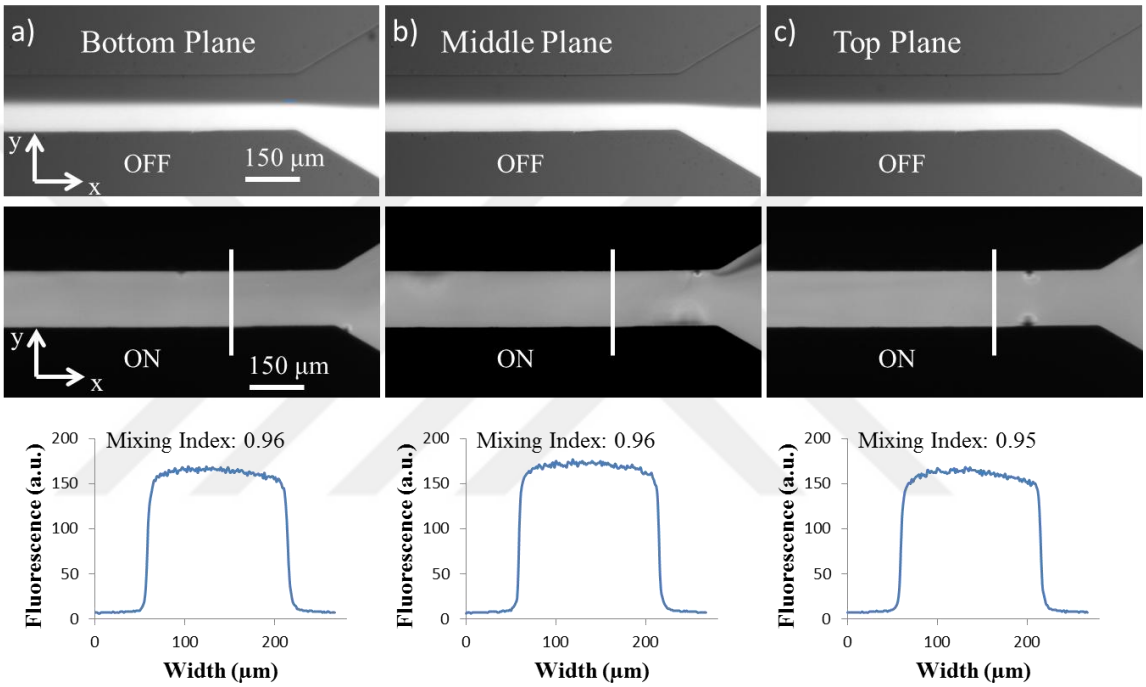

Figure 4.6. Mixing homogeneity along the z-axis. PEG solution with a viscosity 65.3 mPa.s was injected from inlet 2, and the PEG solution with a viscosity of 34.2 mPa.s was injected from inlet 1. The top panel shows the laminar flow of the fluids in the a) bottom, b) middle, and c) top planes of the microfluidic channel (when the piezoelectric transducer was off). The middle panel shows the mixed state of the fluids with the bubble inception and cavitations from the sidewall (when the piezoelectric transducer was on). The bottom panel shows the fluorescent intensity profiles along the white line in the middle panel along with the calculated mixing indexes.

4-5 Conclusions

In conclusion, I have demonstrated an acoustofluidic mixer that can effectively mix two viscous fluids within 100 milliseconds. The mixing was achieved by using the surface roughness of PDMS channel sidewalls to incept and cavitate bubbles in the

presence of acoustic waves. Large bubbles developed in the channel were found to be propelled via small bubble cavitations, which also contributed to the mixing. Mixing performance of the device was tested using a range of PEG solutions with different viscosities, and the mixing efficiency was measured to be 0.88−0.97. When 90% PEG (77.3 mPa.s) solution and 67% PEG-fluorescein (34.2 mPa.s) solution were co-injected into the device, a mixing efficiency of 0.92 was achieved, and the viscosity of the mixed solution was measured to be 48.8 mPa.s (54.9 times higher than that of water). Our device is simple to fabricate, easy to operate, and can be conveniently integrated with other microfluidic components. With further optimization, I believe that our acoustofluidic micromixer has a great potential in many lab-on-a-chip applications such as nanoparticle synthesis, microscopic sonochemical reactions, and biochemical reactors.

Chapter 5

Concluding Remarks

5-1 Summary

Development of new and useful experimental tools significantly contributes to the advancement of biotechnology. One of the challenges of working with small samples in micrometre scales is that positioning of the samples is not an easy task. Especially for three dimensional (3D) imaging of microscopic objects such as single cells and multicellular organisms, precise and controllable rotational manipulation is critical. For example, in the study of transparent samples such as cells, *C. elegans*, and zebrafish larvae, rotational manipulation can be used in 3D reconstruction of the samples. New methods of on-chip rotational manipulation are presented in this dissertation. First, trapped microbubbles were studied under acoustic excitation, and the acoustic microstreaming flows were studied for trapping capacity for single cells and *C. elegans*. These streaming flows were used to apply a torque to the samples and rotate them inside the microfluidic channels with a high precision and control. Using the microbubble induced acoustofluidic rotational manipulation, the composition and structure of the *C. elegans* vulva was studied. The ability to rotationally position the worms revealed defective vulval structures. Furthermore, by rotational positioning, the ALA neuron dendrites were clearly observed simultaneously.

Afterwards, a bubble-free rotational manipulation method was developed based on oscillating solid structures in microfluidic channels. Using the same principle of acoustic streaming which, in this case, is generated by the oscillation of sharp PDMS structures and thin glass slides on which the entire PDMS channel was bonded, single cells and *C. elegans* were rotated in a controlled manner. Trapped microbubbles tend to grow during longer acoustic excitations which render the microfluidic device unusable. This method is more robust compared to the bubble based rotational manipulation method as there is no need for bubble trapping. Therefore, acoustic characteristics of the device do not change during their operations which, on the other hand, are strongly dependent on the microbubble size in the trapped bubble systems.

Finally, an acoustofluidic high viscosity mixer was realized using microbubble inception and cavitations inside PDMS microchannels. Fluid mixing is not a trivial task in low Reynolds number microfluidic systems. High viscosity fluids pose even a more difficult task. Using very simple PDMS microchannels that had grooved structures on the inner side walls due to the deep reactive ion etching process, microbubbles were generated by application of a strong acoustic field. By further application of the acoustic waves, these microbubbles eventually collapsed and produced jetting flows which in turn induced fluid mixing. Mobile microbubbles and microbubble clusters also contributed to the fluid mixing by acoustic streaming flows along the micro channels. PEG solutions that are 54.9 times higher than that of water were efficiently mixed under 100 milliseconds using this acoustofluidic approach.

5-2 Future work

Rotational manipulation of single cells and *C. elegans* is demonstrated in this dissertation using acoustofluidics. The applications shown prove that the acoustofluidic rotational manipulation (ARM) yields tremendous advantages in model animal studies. The ARM chips costs less than 1 dollar in bulk fabrication. The whole operational setup in the current state is not miniaturized. Instead, I used function generators and power amplifiers to drive the devices. The cost of the current required electronics is in the vicinity of $10,000. However, these electronics are general purpose, full range equipment. The entire electronics can be fabricated under $100 with specific power characteristics to drive the presented devices. In the current devices, the size of the generated streaming vortices is sufficient to rotate cells and *C. elegans* which are up to a millimeter in length and 100 micrometers in diameter. *C. elegans* is an important animal model for many important diseases. ARM provides an excellent platform for multidimensional imaging of these transparent worms. However, there are other model organisms including zebrafish that is used as model organisms in critical research areas such as drug discovery and cancer studies. Zebrafish is a vertebrate which is a higher level organism than *C. elegans* or *Drosophila melanogaster* that makes zebrafish an attractive model. As a future work, I would like to develop on-chip rotational manipulation systems that can rotational maneuver zebrafish larvae for three-dimensional imaging. A zebrafish larva is about 2-3 mm in length and up to 500 micrometers in diameter. For this purpose, I will employ larger microfluidic channels and flexible piezo

materials that are commercially available to generate large streaming vortices that would be sufficiently bigger to rotate zebrafish larvae on-chip. A simple design is shown in Figure 5.1 where a flexible piezo is used to generate vibrational forcing on the fluid to generate streaming flows inside the microfluidic channels.

There is still more science and engineering to explore in the acoustofluidic rotational manipulation methods. The bubbled based method comes with the challenge of changing acoustic parameters due to variation in the bubble size during long term operations. For better bubble stability, coated bubbles can be used which can provide more stable operation conditions. I used semispherical bubbles to realize trapping and rotation of worms. Fully spherical bubbles can be studied and their performance can be compared to the semispherical bubbles. The fully spherical bubbles can be injected into microchannels along with the samples to be rotated, and under acoustic excitations the rotational manipulation can be investigated.

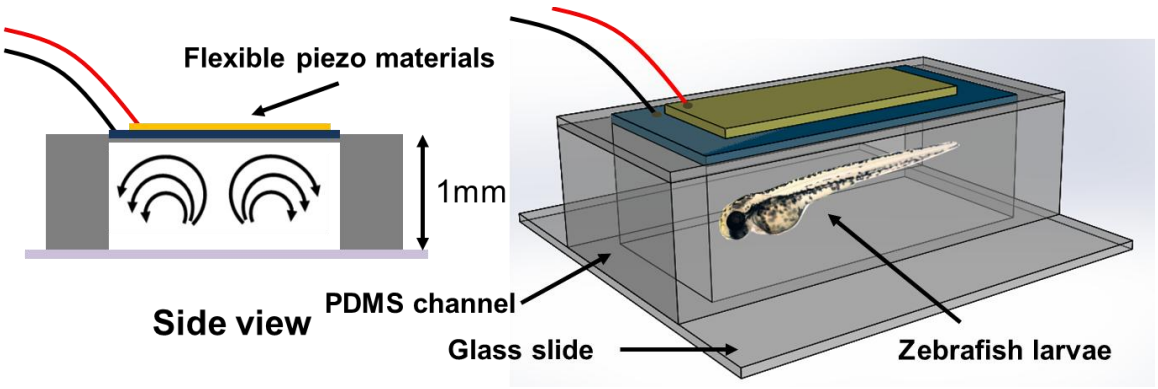

Figure 5.1. Cartoon schematic of the proposed large scale organism manipulation device. The left panel shows the side view of the proposed device. The right panel shows 3D depiction of the proposed device.

Acoustofluidic mixing of high viscosity fluids benefits many fields in biological and chemical applications that require high viscosity reagent handling. The method I presented can mix relatively high viscosity fluids. However, the experimental conditions demonstrated in this dissertation were not studied theoretically using the relevant equations. An important parameter of this method is the radius of the microbubbles before they collapse. The radius, R_c, of a single bubble at the collapsing point can be approximated by the Rayleigh-Plesset equation [184] and is given by:

$$R_C \frac{d^2R_C}{dt^2}\left\{1+\frac{R_C}{2d_C}-\frac{2}{C_\infty}\left(\frac{dR_C}{dt}\right)\right\}+\frac{3}{2}\frac{d^2R_C}{dt^2}\left\{1+\frac{2R_C}{3d_C}-\frac{4}{3C_\infty}\left(\frac{dR_C}{dt}\right)\right\}$$

$$+\rho_L^{-1}\left\{P_\infty - P_{r=R_C}-\frac{R_C}{C_\infty}\frac{dP_{r=R_C}}{dt}\right\}=0 \qquad 5\text{-}1$$

$$P_\infty = P_0 + P(t) \qquad 5\text{-}2$$

$$P_{r=R_C} = p_0\left(\frac{R_{C(max)}}{R_C}\right)^{3\chi}-\frac{2\sigma}{R_C} \qquad 5\text{-}3$$

where P_0 is the initial pressure inside the bubble, $P_{(t)}$ is the superimposed time-dependent pressure on P_0, d_c is the distance from the center of the bubble to the wall, χ is the ratio of specific heat between the vapor and gas, $R_{c(max)}$ is the maximum bubble radius, $P_{r=Rc}$ is the pressure in liquid at the bubble surface, C_∞ is the sound velocity in fluid at infinity, ρ_L is the density of the fluid, and σ is the surface tension of the fluid. Experimental results can be validated by using these equations to better understand the mixing mechanism of the presented device. Furthermore, theoretical limitations of the device can be used to estimate the maximum viscosity and flow rate that mixing can occur.

Bibliography

[1] G. M. Whitesides, “The origins and the future of microfluidics.,” *Nature*, vol. 442, no. 7101, pp. 368–73, Jul. 2006.

[2] J.-B. Bao and D. Jed Harrison, “Measurement of flow in microfluidic networks with micrometer-sized flow restrictors,” *AIChE J.*, vol. 52, no. 1, pp. 75–85, Jan. 2006.

[3] K. F. Lei, “Materials and Fabrication Techniques for Nano- and Microfluidic Devices,” in *Microfluidics in Detection Science: Lab-on-a-chip Technologies*, 2014, pp. 1–28.

[4] D. J. Beebe, G. A. Mensing, and G. M. Walker, “Physics and Applications of Microfluidics in Biology,” *Annu. Rev. Biomed. Eng.*, vol. 4, no. 1, pp. 261–286, Aug. 2002.

[5] W. Weaver, H. Kittur, M. Dhar, and D. Di Carlo, “Research highlights: microfluidic point-of-care diagnostics,” *Lab Chip*, vol. 14, no. 12, p. 1962, 2014.

[6] N. Blow, “Microfluidics: in search of a killer application,” *Nat. Methods*, vol. 4, no. 8, pp. 665–670, Aug. 2007.

[7] D. WEIBEL and G. WHITESIDES, “Applications of microfluidics in chemical biology,” *Curr. Opin. Chem. Biol.*, vol. 10, no. 6, pp. 584–591, Dec. 2006.

[8] A. Ben-Yakar, N. Chronis, and H. Lu, “Microfluidics for the analysis of behavior, nerve regeneration, and neural cell biology in C. elegans,” *Curr. Opin. Neurobiol.*, vol. 19, no. 5, pp. 561–567, Oct. 2009.

[9] X. Ding, S.-C. S. Lin, B. Kiraly, H. Yue, S. Li, I.-K. I.-K. Chiang, J. Shi, S. J. Benkovic, and T. J. Huang, “On-chip manipulation of single microparticles, cells, and organisms using surface acoustic waves,” *Proc. Natl. Acad. Sci. U. S. A.*, vol. 109, no. 28, pp. 11105–11109, Jul. 2012.

[10] X. Ai, W. Zhuo, Q. Liang, P. T. McGrath, and H. Lu, “A high-throughput device for size based separation of C. elegans developmental stages.,” *Lab Chip*, vol. 14, no. 10, pp. 1746–52, 2014.

[11] M. M. Crane, J. N. Stirman, C.-Y. Ou, P. T. Kurshan, J. M. Rehg, K. Shen, and H. Lu, “Autonomous screening of C. elegans identifies genes implicated in synaptogenesis.,” *Nat. Methods*, vol. 9, no. 10, pp. 977–80, Oct. 2012.

[12] J. West, M. Becker, S. Tombrink, and A. Manz, “Micro Total Analysis Systems: Latest Achievements,” *Anal. Chem.*, vol. 80, no. 12, pp. 4403–4419, Jun. 2008.

[13] T. Vilkner, D. Janasek, and A. Manz, “Micro Total Analysis Systems. Recent Developments,” *Anal. Chem.*, vol. 76, no. 12, pp. 3373–3386, Jun. 2004.

[14] P.-A. Auroux, D. Iossifidis, D. R. Reyes, and A. Manz, “Micro Total Analysis Systems. 2. Analytical Standard Operations and Applications,” *Anal. Chem.*, vol. 74, no. 12, pp. 2637–2652, Jun. 2002.

[15] D. R. Reyes, D. Iossifidis, P.-A. Auroux, and A. Manz, “Micro Total Analysis Systems. 1. Introduction, Theory, and Technology,” *Anal. Chem.*, vol. 74, no. 12, pp. 2623–2636, Jun. 2002.

[16] A. J. deMello, “Control and detection of chemical reactions in microfluidic systems,” *Nature*, vol. 442, no. 7101, pp. 394–402, Jul. 2006.

[17] R. Daw and J. Finkelstein, “Lab on a chip,” *Nature*, vol. 442, no. 7101, pp. 367–367, Jul. 2006.

[18] H. Craighead, “Future lab-on-a-chip technologies for interrogating individual molecules,” *Nature*, vol. 442, no. 7101, pp. 387–393, Jul. 2006.

[19] D. Janasek, J. Franzke, and A. Manz, “Scaling and the design of miniaturized chemical-analysis systems,” *Nature*, vol. 442, no. 7101, pp. 374–380, Jul. 2006.

[20] S. Haeberle and R. Zengerle, “Microfluidic platforms for lab-on-a-chip applications.,” *Lab Chip*, vol. 7, no. 9, pp. 1094–110, Sep. 2007.

[21] L. Guo, J. Feng, Z. Fang, J. Xu, and X. Lu, “Application of microfluidic ‘lab-on-a-chip’ for the detection of mycotoxins in foods,” *Trends Food Sci. Technol.*, vol. 46, no. 2, pp. 252–263, Dec. 2015.

[22] K. V. Sharp and R. J. Adrian, “Transition from laminar to turbulent flow in liquid filled microtubes,” *Exp. Fluids*, vol. 36, no. 5, pp. 741–747, May 2004.

[23] R. Barnkob, P. Augustsson, T. Laurell, and H. Bruus, “Acoustic radiation- and streaming-induced microparticle velocities determined by microparticle image velocimetry in an ultrasound symmetry plane,” *Phys. Rev. E*, vol. 86, no. 5, p. 056307, Nov. 2012.

[24] O. V. Rudenko, A. P. Sarvazyan, and S. Y. Emelianov, “Acoustic radiation force and streaming induced by focused nonlinear ultrasound in a dissipative medium,” *J. Acoust. Soc. Am.*, vol. 99, no. 5, p. 2791, 1996.

[25] D. Ahmed, A. Ozcelik, N. Bojanala, N. Nama, A. Upadhyay, Y. Chen, W. Hanna-Rose, and T. J. Huang, “Rotational manipulation of single cells and organisms using acoustic waves,” *Nat. Commun.*, vol. 7, p. 11085, Mar. 2016.

[26] X. Ding, P. Li, S.-C. S. Lin, Z. S. Stratton, N. Nama, F. Guo, D. Slotcavage, X.

Mao, J. Shi, F. Costanzo, and T. J. Huang, “Surface acoustic wave microfluidics.,” *Lab Chip*, vol. 13, no. 18, pp. 3626–49, Sep. 2013.

[27] X. Ding, J. Shi, S.-C. S. Lin, S. Yazdi, B. Kiraly, and T. J. Huang, “Tunable patterning of microparticles and cells using standing surface acoustic waves,” *Lab Chip*, vol. 12, no. 14, p. 2491, 2012.

[28] P. Marmottant, J. P. Raven, H. Gardeniers, J. G. Bomer, and S. Hilgenfeldt, “Microfluidics with ultrasound-driven bubbles,” *J. Fluid Mech.*, vol. 568, p. 109, Nov. 2006.

[29] S.-C. S. Lin, X. Mao, and T. J. Huang, “Surface acoustic wave (SAW) acoustophoresis: now and beyond.,” *Lab Chip*, vol. 12, no. 16, pp. 2766–70, Aug. 2012.

[30] X. Ding, Z. Peng, S.-C. S. Lin, M. Geri, S. Li, P. Li, Y. Chen, M. Dao, S. Suresh, and T. J. Huang, “Cell separation using tilted-angle standing surface acoustic waves.,” *Proc. Natl. Acad. Sci. U. S. A.*, vol. 111, no. 36, pp. 12992–12997, Aug. 2014.

[31] J. Shi, H. Huang, Z. Stratton, Y. Huang, and T. J. Huang, “Continuous particle separation in a microfluidic channel via standing surface acoustic waves (SSAW).,” *Lab Chip*, vol. 9, no. 23, pp. 3354–3359, 2009.

[32] C. Wang, S. V Jalikop, and S. Hilgenfeldt, “Efficient manipulation of microparticles in bubble streaming flows.,” *Biomicrofluidics*, 2012.

[33] T. Franke, A. R. Abate, D. A. Weitz, and A. Wixforth, “Surface acoustic wave (SAW) directed droplet flow in microfluidics for PDMS devices,” *Lab Chip*, vol. 9, no. 18, p. 2625, 2009.

[34] a Lenshof, M. Evander, T. Laurell, and J. Nilsson, “Acoustofluidics 5: Building microfluidic acoustic resonators.,” *Lab Chip*, vol. 12, no. 4, pp. 684–95, Feb. 2012.

[35] M. Antfolk, C. Antfolk, H. Lilja, T. Laurell, and P. Augustsson, “A single inlet two-stage acoustophoresis chip enabling tumor cell enrichment from white blood cells,” *Lab Chip*, vol. 15, no. 9, pp. 2102–2109, 2015.

[36] M. Antfolk, C. Magnusson, P. Augustsson, H. Lilja, and T. Laurell, “Acoustofluidic, Label-Free Separation and Simultaneous Concentration of Rare Tumor Cells from White Blood Cells,” *Anal. Chem.*, vol. 87, no. 18, pp. 9322–9328, Sep. 2015.

[37] R. D. O’Rorke, C. D. Wood, C. Wälti, S. D. Evans, A. G. Davies, and J. E. Cunningham, “Acousto-microfluidics: Transporting microbubble and microparticle arrays in acoustic traps using surface acoustic waves,” *J. Appl. Phys.*,

vol. 111, no. 9, p. 094911, 2012.

[38] Y. Xie, C. Chindam, N. Nama, S. Yang, M. Lu, Y. Zhao, J. D. Mai, F. Costanzo, and T. J. Huang, "Exploring bubble oscillation and mass transfer enhancement in acoustic-assisted liquid-liquid extraction with a microfluidic device," *Sci. Rep.*, vol. 5, p. 12572, Jul. 2015.

[39] Y. Chen and S. Lee, "Manipulation of Biological Objects Using Acoustic Bubbles: A Review," *Integr. Comp. Biol.*, vol. 54, no. 6, pp. 959–968, Dec. 2014.

[40] Z. Fan, H. Liu, M. Mayer, and C. X. Deng, "Spatiotemporally controlled single cell sonoporation," *Proc. Natl. Acad. Sci.*, vol. 109, no. 41, pp. 16486–16491, Oct. 2012.

[41] Y. Zhou, K. Yang, J. Cui, J. Y. Y. Ye, and C. X. X. Deng, "Controlled permeation of cell membrane by single bubble acoustic cavitation," *J. Control. Release*, vol. 157, no. 1, pp. 103–11, Jan. 2012.

[42] Y. Chen, Z. Fang, B. Merritt, D. Strack, J. Xu, and S. Lee, "Onset of particle trapping and release via acoustic bubbles," *Lab Chip*, 2016.

[43] D. Ahmed, X. Peng, A. Ozcelik, Y. Zheng, and T. J. Huang, "Acousto-plasmofluidics: Acoustic modulation of surface plasmon resonance in microfluidic systems," *AIP Adv.*, vol. 5, no. 9, p. 097161, Sep. 2015.

[44] F. Guo, P. Li, J. B. French, Z. Mao, H. Zhao, S. Li, N. Nama, J. R. Fick, S. J. Benkovic, and T. J. Huang, "Controlling cell-cell interactions using surface acoustic waves.," *Proc. Natl. Acad. Sci. U. S. A.*, Dec. 2014.

[45] Y. Chen, X. Ding, S.-C. Steven Lin, S. Yang, P.-H. Huang, N. Nama, Y. Zhao, A. A. Nawaz, F. Guo, W. Wang, Y. Gu, T. E. Mallouk, and T. J. Huang, "Tunable Nanowire Patterning Using Standing Surface Acoustic Waves," *ACS Nano*, vol. 7, no. 4, pp. 3306–3314, Apr. 2013.

[46] P.-H. Huang, N. Nama, Z. Mao, P. Li, J. Rufo, Y. Chen, Y. Xie, C.-H. Wei, L. Wang, and T. J. Huang, "A reliable and programmable acoustofluidic pump powered by oscillating sharp-edge structures," *Lab Chip*, vol. 14, no. 22, pp. 4319–4323, 2014.

[47] S. Hong, Q. Pan, and L. P. Lee, "Single-cell level co-culture platform for intercellular communication," *Integr. Biol.*, vol. 4, no. 4, p. 374, 2012.

[48] I. Pushkarsky, Y. Lyb, W. Weaver, T.-W. Su, O. Mudanyali, A. Ozcan, and D. Di Carlo, "Automated single-cell motility analysis on a chip using lensfree microscopy," *Sci. Rep.*, vol. 4, Apr. 2014.

[49] N. A. Bakhtina and J. G. Korvink, “Microfluidic laboratories for C. elegans enhance fundamental studies in biology,” *RSC Adv.*, vol. 4, no. 9, pp. 4691–4709, 2014.

[50] A. G. Fraser, R. S. Kamath, P. Zipperlen, M. Martinez-Campos, M. Sohrmann, and J. Ahringer, “Functional genomic analysis of C. elegans chromosome I by systematic RNA interference.,” *Nature*, vol. 408, no. 6810, pp. 325–30, Nov. 2000.

[51] A. J. Chung, Y. S. Huh, and D. Erickson, “A robust, electrochemically driven microwell drug delivery system for controlled vasopressin release,” *Biomed. Microdevices*, vol. 11, no. 4, pp. 861–867, Aug. 2009.

[52] I. de C. Cáceres, N. Valmas, M. A. Hilliard, and H. Lu, “Laterally orienting C. elegans using geometry at microscale for high-throughput visual screens in neurodegeneration and neuronal development studies,” *PLoS One*, vol. 7, no. 4, p. e35037, Jan. 2012.

[53] C. B. Rohde, F. Zeng, R. Gonzalez-Rubio, M. Angel, and M. F. Yanik, “Microfluidic system for on-chip high-throughput whole-animal sorting and screening at subcellular resolution.,” *Proc. Natl. Acad. Sci. U. S. A.*, vol. 104, no. 35, pp. 13891–5, Aug. 2007.

[54] A. F. Coskun, I. Sencan, T.-W. Su, and A. Ozcan, “Lensfree Fluorescent On-Chip Imaging of Transgenic Caenorhabditis elegans Over an Ultra-Wide Field-of-View,” *PLoS One*, vol. 6, no. 1, p. e15955, Jan. 2011.

[55] S. K. Mohanty, A. Uppal, and P. K. Gupta, “Self-rotation of red blood cells in optical tweezers: prospects for high throughput malaria diagnosis.,” *Biotechnol. Lett.*, vol. 26, no. 12, pp. 971–974, 2004.

[56] R. Elbez, B. H. McNaughton, L. Patel, K. J. Pienta, and R. Kopelman, “Nanoparticle induced cell magneto-rotation: monitoring morphology, stress and drug sensitivity of a suspended single cancer cell.,” *PLoS One*, vol. 6, no. 12, p. e28475, Jan. 2011.

[57] K. Chung, M. M. Crane, and H. Lu, “Automated on-chip rapid microscopy, phenotyping and sorting of C. elegans.,” *Nat. Methods*, vol. 5, no. 7, pp. 637–43, Jul. 2008.

[58] C. Pardo-Martin, A. Allalou, J. Medina, P. M. Eimon, C. Wählby, and M. Fatih Yanik, “High-throughput hyperdimensional vertebrate phenotyping.,” *Nat. Commun.*, vol. 4, p. 1467, Jan. 2013.

[59] N. Ghorashian, S. K. Gökçe, S. X. Guo, W. N. Everett, and A. Ben-Yakar, “An Automated Microfluidic Multiplexer for Fast Delivery of C. elegans Populations from Multiwells,” *PLoS One*, vol. 8, no. 9, p. e74480, Sep. 2013.

[60] C. Pardo-Martin, T.-Y. Chang, B. K. Koo, C. L. Gilleland, S. C. Wasserman, and M. F. Yanik, “High-throughput in vivo vertebrate screening.,” *Nat. Methods*, vol. 7, no. 8, pp. 634–636, Aug. 2010.

[61] S. X. Guo, F. Bourgeois, T. Chokshi, N. J. Durr, M. A. Hilliard, N. Chronis, and A. Ben-Yakar, “Femtosecond laser nanoaxotomy lab-on-a-chip for in vivo nerve regeneration studies.,” *Nat. Methods*, vol. 5, no. 6, pp. 531–3, Jun. 2008.

[62] B. Neumann, K. C. Q. Nguyen, D. H. Hall, A. Ben-Yakar, and M. A. Hilliard, “Axonal regeneration proceeds through specific axonal fusion in transected C. elegans neurons,” *Dev. Dyn.*, vol. 240, no. 6, pp. 1365–1372, 2011.

[63] M. F. Yanik, H. Cinar, H. N. Cinar, A. D. Chisholm, Y. Jin, and A. Ben-Yakar, “Neurosurgery: functional regeneration after laser axotomy.,” *Nature*, vol. 432, no. 7019, p. 822, Dec. 2004.

[64] D. G. Grier, “A revolution in optical manipulation.,” *Nature*, vol. 424, no. 6950, pp. 810–6, Aug. 2003.

[65] I. De Vlaminck and C. Dekker, “Recent Advances in Magnetic Tweezers,” *Annu. Rev. Biophys.*, vol. 41, no. 1, pp. 453–472, Jun. 2012.

[66] G. W. J. Brodie, Y. Qiu, S. Cochran, G. C. Spalding, and M. P. Macdonald, “Letters: optically transparent piezoelectric transducer for ultrasonic particle manipulation,” *IEEE Trans. Ultrason. Ferroelectr. Freq. Control*, vol. 61, no. 3, pp. 389–391, Mar. 2014.

[67] P. Cheng, M. J. Barrett, P. M. Oliver, D. Cetin, and D. Vezenov, “Dielectrophoretic tweezers as a platform for molecular force spectroscopy in a highly parallel format,” *Lab Chip*, vol. 11, no. 24, p. 4248, 2011.

[68] G. Pilwat and U. Zimmermann, “Rotation of a single cell in a discontinuous rotating electric field,” *J. Electroanal. Chem. Interfacial Electrochem.*, vol. 155, pp. 155–162, Jan. 1983.

[69] G. Fuhr, W. M. Arnold, R. Hagedorn, T. Müller, W. Benecke, B. Wagner, and U. Zimmermann, “Levitation, holding, and rotation of cells within traps made by high-frequency fields.,” *Biochim. Biophys. Acta*, vol. 1108, no. 2, pp. 215–23, Jul. 1992.

[70] M. E. J. Friese, T. A. Nieminen, N. R. Heckenberg, and H. Rubinsztein-Dunlop, “Optical alignment and spinning of laser-trapped microscopic particles,” *Nature*, vol. 395, no. October, p. 4, 2003.

[71] T. Wu, T. a. Nieminen, S. Mohanty, J. Miotke, R. L. Meyer, H. Rubinsztein-Dunlop, and M. W. Berns, “A photon-driven micromotor can direct nerve fibre

growth," *Nat. Photonics*, vol. 6, no. 1, pp. 62–67, Dec. 2011.

[72] L. Paterson, M. P. MacDonald, J. Arlt, W. Sibbett, P. E. Bryant, and K. Dholakia, "Controlled rotation of optically trapped microscopic particles.," *Science (80-.).*, vol. 292, no. 5518, pp. 912–4, May 2001.

[73] M. B. Rasmussen, L. B. Oddershede, and H. Siegumfeldt, "Optical tweezers cause physiological damage to Escherichia coli and Listeria bacteria.," *Appl. Environ. Microbiol.*, vol. 74, no. 8, pp. 2441–6, Apr. 2008.

[74] D. Fan, F. Zhu, R. Cammarata, and C. Chien, "Controllable High-Speed Rotation of Nanowires," *Phys. Rev. Lett.*, vol. 94, no. 24, p. 247208, Jun. 2005.

[75] L.-H. Chau, W. Liang, F. W. K. Cheung, W. K. Liu, W. J. Li, S.-C. Chen, and G.-B. Lee, "Self-rotation of cells in an irrotational AC E-field in an opto-electrokinetics chip.," *PLoS One*, vol. 8, no. 1, p. e51577, Jan. 2013.

[76] M. Liu, T. Zentgraf, Y. Liu, G. Bartal, and X. Zhang, "Light-driven nanoscale plasmonic motors.," *Nat. Nanotechnol.*, vol. 5, no. 8, pp. 570–3, Aug. 2010.

[77] A. K. Bentley, J. S. Trethewey, A. B. Ellis, and W. C. Crone, "Magnetic Manipulation of Copper−Tin Nanowires Capped with Nickel Ends," *Nano Lett.*, vol. 4, no. 3, pp. 487–490, Mar. 2004.

[78] D. L. Fan, F. Q. Zhu, X. Xu, R. C. Cammarata, and C. L. Chien, "Electronic properties of nanoentities revealed by electrically driven rotation.," *Proc. Natl. Acad. Sci. U. S. A.*, vol. 109, no. 24, pp. 9309–13, Jun. 2012.

[79] Z. Hong, J. Zhang, and B. W. Drinkwater, "Observation of Orbital Angular Momentum Transfer from Bessel-Shaped Acoustic Vortices to Diphasic Liquid-Microparticle Mixtures," *Phys. Rev. Lett.*, vol. 114, no. 21, p. 214301, May 2015.

[80] A. Marzo, S. A. Seah, B. W. Drinkwater, D. R. Sahoo, B. Long, and S. Subramanian, "Holographic acoustic elements for manipulation of levitated objects," *Nat. Commun.*, vol. 6, p. 8661, Oct. 2015.

[81] A. Grinenko, M. P. MacDonald, C. R. P. Courtney, P. D. Wilcox, C. E. M. Demore, S. Cochran, and B. W. Drinkwater, "Tunable beam shaping with a phased array acousto-optic modulator," *Opt. Express*, vol. 23, no. 1, p. 26, Jan. 2015.

[82] B. T. Hefner and P. L. Marston, "An acoustical helicoidal wave transducer with applications for the alignment of ultrasonic and underwater systems," *J. Acoust. Soc. Am.*, vol. 106, no. 6, p. 3313, 1999.

[83] S. Gspan, A. Meyer, S. Bernet, and M. Ritsch-Marte, "Optoacoustic generation of a helicoidal ultrasonic beam," *J. Acoust. Soc. Am.*, vol. 115, no. 3, p. 1142, 2004.

[84] A. Hashmi, G. Yu, M. Reilly-Collette, G. Heiman, and J. Xu, “Oscillating bubbles: a versatile tool for lab on a chip applications.,” *Lab Chip*, vol. 12, no. 21, pp. 4216–27, Nov. 2012.

[85] A. Hashmi, G. Heiman, G. Yu, M. Lewis, H.-J. Kwon, and J. Xu, “Oscillating bubbles in teardrop cavities for microflow control,” *Microfluid. Nanofluidics*, vol. 14, no. 3–4, pp. 591–596, Oct. 2012.

[86] D. Ahmed, X. Mao, J. Shi, B. K. Juluri, and T. J. Huang, “A millisecond micromixer via single-bubble-based acoustic streaming.,” *Lab Chip*, vol. 9, no. 18, pp. 2738–2741, Sep. 2009.

[87] A. R. Tovar, M. V. Patel, and A. P. Lee, “Lateral air cavities for microfluidic pumping with the use of acoustic energy,” *Microfluid. Nanofluidics*, vol. 10, no. 6, pp. 1269–1278, Jun. 2011.

[88] Y. Xie, D. Ahmed, M. I. Lapsley, M. Lu, S. Li, and T. J. Huang, “Acoustofluidic Relay: Sequential Trapping and Transporting of Microparticles via Acoustically Excited Oscillating Bubbles,” *J. Lab. Autom.*, vol. 19, no. 2, pp. 137–143, Apr. 2014.

[89] Y. Xu, A. Hashmi, G. Yu, X. Lu, H.-J. Kwon, X. Chen, and J. Xu, “Microbubble array for on-chip worm processing,” *Appl. Phys. Lett.*, vol. 102, no. 2, p. 023702, 2013.

[90] D. Ahmed, C. Y. Chan, S.-C. S. Lin, H. S. Muddana, N. Nama, S. J. Benkovic, T. Jun Huang, T. J. Huang, T. Jun Huang, T. J. Huang, T. Jun Huang, and T. J. Huang, “Tunable, pulsatile chemical gradient generation via acoustically driven oscillating bubbles.,” *Lab Chip*, vol. 13, no. 3, pp. 328–31, Feb. 2013.

[91] D. Ahmed, H. S. Muddana, M. Lu, J. B. French, A. Ozcelik, Y. Fang, P. J. Butler, S. J. Benkovic, A. Manz, and T. J. Huang, “Acoustofluidic Chemical Waveform Generator and Switch,” *Anal. Chem.*, vol. 86, pp. 11803–11810, 2014.

[92] T. Kaletta and M. O. Hengartner, “Finding function in novel targets: C. elegans as a model organism.,” *Nat. Rev. Drug Discov.*, vol. 5, no. 5, pp. 387–98, May 2006.

[93] S. Brenner, “The genetics of Caenorhabditis elegans.,” *Genetics*, vol. 77, no. 1, pp. 71–94, 1974.

[94] N. Nama, P.-H. Huang, T. J. Huang, and F. Costanzo, “Investigation of acoustic streaming patterns around oscillating sharp edges,” *Lab Chip*, vol. 14, pp. 2824–2836, 2014.

[95] M. S. Longuet-Higgins, “Viscous streaming from an oscillating spherical bubble,” *Proc. R. Soc. A Math. Phys. Eng. Sci.*, vol. 454, no. 1970, pp. 725–742, Feb. 1998.

[96] M. A. Ainslie and T. G. Leighton, “Review of scattering and extinction cross-sections, damping factors, and resonance frequencies of a spherical gas bubble.,” *J. Acoust. Soc. Am.*, vol. 130, no. 5, pp. 3184–208, Nov. 2011.

[97] P. Marmottant and S. Hilgenfeldt, “A bubble-driven microfluidic transport element for bioengineering.,” *Proc. Natl. Acad. Sci. U. S. A.*, vol. 101, no. 26, pp. 9523–7, Jun. 2004.

[98] P. Marmottant and S. Hilgenfeldt, “Controlled vesicle deformation and lysis by single oscillating bubbles.,” *Nature*, vol. 423, no. 6936, pp. 153–6, May 2003.

[99] C. Wang, B. Rallabandi, and S. Hilgenfeldt, “Frequency dependence and frequency control of microbubble streaming flows,” *Phys. Fluids*, vol. 25, no. 2, p. 022002, 2013.

[100] P. Tho, Y. Zhu, R. Manasseh, and A. Ooi, “Measurement of microbubble-induced acoustic microstreaming using microparticle image velocimetry,” in *Proc. SPIE*, 2005, pp. 336–347.

[101] D. L. Miller, “Particle gathering and microstreaming near ultrasonically activated gas-filled micropores,” *J. Acoust. Soc. Am.*, vol. 84, no. 4, p. 1378, Oct. 1988.

[102] D. A. Wolff and H. Pertoft, “Separation of HeLa cells by colloidal silica density gradient centrifugation. I. Separation and partial synchrony of mitotic cells.,” *J. Cell Biol.*, vol. 55, no. 3, pp. 579–85, Dec. 1972.

[103] A. Reina, A. B. Subramaniam, A. Laromaine, A. D. T. Samuel, and G. M. Whitesides, “Shifts in the Distribution of Mass Densities Is a Signature of Caloric Restriction in Caenorhabditis elegans,” *PLoS One*, vol. 8, no. 7, p. e69651, Jul. 2013.

[104] D. Ahmed, M. Lu, A. Nourhani, P. E. Lammert, Z. Stratton, H. S. Muddana, V. H. Crespi, and T. J. Huang, “Selectively manipulable acoustic-powered microswimmers,” *Sci. Rep.*, vol. 5, p. 9744, May 2015.

[105] T. G. Leighton, *The acoustic bubble*. Academic Press, 1994.

[106] L. van der Pol and J. Tramper, “Shear sensitivity of animal cells from a culture-medium perspective,” *Trends Biotechnol.*, vol. 16, no. 8, pp. 323–328, Dec. 1998.

[107] R. Sharma-Kishore, J. G. White, E. Southgate, and B. Podbilewicz, “Formation of the vulva in Caenorhabditis elegans: a paradigm for organogenesis.,” *Development*, vol. 126, no. 4, pp. 691–699, 1999.

[108] Z. Chen, D. J. Eastburn, and M. Han, “The Caenorhabditis elegans nuclear receptor gene nhr-25 regulates epidermal cell development.,” *Mol. Cell. Biol.*, vol.

24, no. 17, pp. 7345–58, Oct. 2004.

[109] B. J. Hwang and P. W. Sternberg, “A cell-specific enhancer that specifies lin-3 expression in the C. elegans anchor cell for vulval development.,” *Development*, vol. 131, no. 1, pp. 143–51, Jan. 2004.

[110] T. R. Zahn, M. A. Macmorris, W. Dong, R. Day, and J. C. Hutton, “IDA-1, a Caenorhabditis elegans homolog of the diabetic autoantigens IA-2 and phogrin, is expressed in peptidergic neurons in the worm,” *J. Comp. Neurol.*, vol. 429, no. 1, pp. 127–143, 2001.

[111] C. Van Buskirk and P. W. Sternberg, “Epidermal growth factor signaling induces behavioral quiescence in Caenorhabditis elegans.,” *Nat. Neurosci.*, vol. 10, no. 10, pp. 1300–7, Oct. 2007.

[112] Y. Qiu, H. Wang, C. Demore, D. Hughes, P. Glynne-Jones, S. Gebhardt, A. Bolhovitins, R. Poltarjonoks, K. Weijer, A. Schönecker, M. Hill, and S. Cochran, “Acoustic Devices for Particle and Cell Manipulation and Sensing,” *Sensors*, vol. 14, no. 8, pp. 14806–14838, Aug. 2014.

[113] S. Ramaswamy, S. M. Boronyak, T. Le, A. Holmes, F. Sotiropoulos, and M. S. Sacks, “A Novel Bioreactor for Mechanobiological Studies of Engineered Heart Valve Tissue Formation Under Pulmonary Arterial Physiological Flow Conditions,” *J. Biomech. Eng.*, vol. 136, no. 12, p. 121009, Dec. 2014.

[114] M. Deng, Y. Wang, B. Zhang, P. Liu, H. Xiao, and J. Zhao, “New proangiogenic activity on vascular endothelial cells for C-terminal mechano growth factor,” *Acta Biochim. Biophys. Sin. (Shanghai).*, vol. 44, no. 4, pp. 316–322, Apr. 2012.

[115] A. R. Miller, G. L. Davis, Z. M. Oden, M. R. Razavi, A. Fateh, M. Ghazanfari, F. Abdolrahimi, S. Poorazar, F. Sakhaie, R. J. Olsen, A. R. Bahrmand, M. C. Pierce, E. A. Graviss, and R. Richards-Kortum, “Portable, Battery-Operated, Low-Cost, Bright Field and Fluorescence Microscope,” *PLoS One*, vol. 5, no. 8, p. e11890, Aug. 2010.

[116] K. K. Ghosh, L. D. Burns, E. D. Cocker, A. Nimmerjahn, Y. Ziv, A. El Gamal, and M. J. Schnitzer, “Miniaturized integration of a fluorescence microscope,” *Nat. Methods*, vol. 8, no. 10, pp. 871–878, Sep. 2011.

[117] K. Tanner, H. Mori, R. Mroue, A. Bruni-Cardoso, and M. J. Bissell, “Coherent angular motion in the establishment of multicellular architecture of glandular tissues,” *Proc. Natl. Acad. Sci.*, vol. 109, no. 6, pp. 1973–1978, Feb. 2012.

[118] J. P. Junker and A. van Oudenaarden, “Every Cell Is Special: Genome-wide Studies Add a New Dimension to Single-Cell Biology,” *Cell*, vol. 157, no. 1, pp. 8–11, Mar. 2014.

[119] M. Shackleton, E. Quintana, E. R. Fearon, and S. J. Morrison, “Heterogeneity in Cancer: Cancer Stem Cells versus Clonal Evolution,” *Cell*, vol. 138, no. 5, pp. 822–829, Sep. 2009.

[120] S. K. Mohanty and P. K. Gupta, “Laser-assisted three-dimensional rotation of microscopic objects,” *Rev. Sci. Instrum.*, vol. 75, no. 7, p. 2320, 2004.

[121] W. Xi, A. A. Solovev, A. N. Ananth, D. H. Gracias, S. Sanchez, and O. G. Schmidt, “Rolled-up magnetic microdrillers: towards remotely controlled minimally invasive surgery.,” *Nanoscale*, vol. 5, no. 4, pp. 1294–7, Feb. 2013.

[122] B. J. Black and S. K. Mohanty, “Fiber-optic spanner.,” *Opt. Lett.*, vol. 37, no. 24, pp. 5030–2, Dec. 2012.

[123] J. P. Shelby, S. a Mutch, and D. T. Chiu, “Direct manipulation and observation of the rotational motion of single optically trapped microparticles and biological cells in microvortices.,” *Anal. Chem.*, vol. 76, no. 9, pp. 2492–7, May 2004.

[124] A. Ozcelik, D. Ahmed, Y. Xie, N. Nama, Z. Qu, A. A. Nawaz, and T. J. Huang, “An acoustofluidic micromixer via bubble inception and cavitation from microchannel sidewalls.,” *Anal. Chem.*, vol. 86, no. 10, pp. 5083–8, May 2014.

[125] L. Huang and W. Hanna-Rose, “EGF signaling overcomes a uterine cell death associated with temporal mis-coordination of organogenesis within the C. elegans egg-laying apparatus,” *Dev. Biol.*, vol. 300, no. 2, pp. 599–611, Dec. 2006.

[126] M. Crook, M. R. Mcreynolds, W. Wang, and W. Hanna-Rose, “An NAD + biosynthetic pathway enzyme functions cell non-autonomously in C. elegans development,” *Dev. Dyn.*, vol. 243, no. 8, pp. 965–976, Aug. 2014.

[127] P.-H. Huang, Y. Xie, D. Ahmed, J. Rufo, N. Nama, Y. Chen, C. Y. Chan, and T. J. Huang, “An acoustofluidic micromixer based on oscillating sidewall sharp-edges.,” *Lab Chip*, vol. 13, no. 19, pp. 3847–52, Oct. 2013.

[128] J. C. Merchuk, “Shear effects on suspended cells.,” *Adv. Biochem. Eng. Biotechnol.*, vol. 44, no. July 1988, pp. 65–95, 1991.

[129] J. J. Zhong, K. Fujiyama, T. Seki, and T. Yoshida, “A quantitative analysis of shear effects on cell suspension and cell culture of perilla frutescens in bioreactors,” *Biotechnol. Bioeng.*, vol. 44, no. 5, pp. 649–654, 1994.

[130] Z. Mao, Y. Xie, F. Guo, L. Ren, P.-H. Huang, Y. Chen, J. Rufo, F. Costanzo, and T. J. Huang, “Experimental and numerical studies on standing surface acoustic wave microfluidics,” *Lab Chip*, vol. 16, no. 3, pp. 515–524, 2016.

[131] W. Shi, H. Wen, B. Lin, and J. Qin, “Microfluidic platform for the study of

Caenorhabditis elegans.," *Top. Curr. Chem.*, vol. 304, pp. 323–38, Jan. 2011.

[132] A. San-Miguel and H. Lu, "Microfluidics as a tool for C. elegans research," *WormBook*, pp. 1–19, Sep. 2013.

[133] M. Cornaglia, L. Mouchiroud, A. Marette, S. Narasimhan, T. Lehnert, V. Jovaisaite, J. Auwerx, and M. A. M. Gijs, "An automated microfluidic platform for C. elegans embryo arraying, phenotyping, and long-term live imaging," *Sci. Rep.*, vol. 5, p. 10192, May 2015.

[134] Y. Song, J. Hormes, and C. S. S. R. Kumar, "Microfluidic synthesis of nanomaterials.," *Small*, vol. 4, no. 6, pp. 698–711, Jun. 2008.

[135] D. Dendukuri, D. C. Pregibon, J. Collins, T. A. Hatton, and P. S. Doyle, "Continuous-flow lithography for high-throughput microparticle synthesis.," *Nat. Mater.*, vol. 5, no. 5, pp. 365–9, May 2006.

[136] S. Yang, F. Guo, B. Kiraly, X. Mao, M. Lu, K. W. Leong, and T. J. Huang, "Microfluidic synthesis of multifunctional Janus particles for biomedical applications.," *Lab Chip*, vol. 12, no. 12, pp. 2097–102, Jun. 2012.

[137] L. Pollack, M. W. Tate, N. C. Darnton, J. B. Knight, S. M. Gruner, W. a Eaton, and R. H. Austin, "Compactness of the denatured state of a fast-folding protein measured by submillisecond small-angle x-ray scattering.," *Proc. Natl. Acad. Sci. U. S. A.*, vol. 96, no. 18, pp. 10115–7, Aug. 1999.

[138] Y. Xie, D. Ahmed, M. I. Lapsley, S. S. Lin, A. A. Nawaz, L. Wang, and T. J. Huang, "Single-shot characterization of enzymatic reaction constants Km and kcat by an acoustic-driven, bubble-based fast micromixer.," *Anal. Chem.*, vol. 84, no. 17, pp. 7495–501, Sep. 2012.

[139] G. Schabas, H. Yusuf, M. G. Moffitt, and D. Sinton, "Controlled self-assembly of quantum dots and block copolymers in a microfluidic device.," *Langmuir*, vol. 24, no. 3, pp. 637–43, Feb. 2008.

[140] L. Capretto, S. Mazzitelli, G. Colombo, R. Piva, L. Penolazzi, R. Vecchiatini, X. Zhang, and C. Nastruzzi, "Production of polymeric micelles by microfluidic technology for combined drug delivery: application to osteogenic differentiation of human periodontal ligament mesenchymal stem cells (hPDLSCs).," *Int. J. Pharm.*, vol. 440, no. 2, pp. 195–206, Jan. 2013.

[141] K. Anderson, J. M. Cooper, S. J. Haswell, D. Marshall, H. Yin, and X. Zhang, "Microfluidic-based measurements of cytochrome P450 enzyme activity of primary mammalian hepatocytes.," *Analyst*, vol. 135, no. 6, pp. 1282–7, Jun. 2010.

[142] L.-Y. Hung, Y.-H. Chuang, H.-T. Kuo, C.-H. Wang, K.-F. Hsu, C.-Y. Chou, and

G.-B. Lee, “An integrated microfluidic platform for rapid tumor cell isolation, counting and molecular diagnosis.,” *Biomed. Microdevices*, vol. 15, no. 2, pp. 339–52, Apr. 2013.

[143] J. W. Hong, V. Studer, G. Hang, W. F. Anderson, and S. R. Quake, “A nanoliter-scale nucleic acid processor with parallel architecture.,” *Nat. Biotechnol.*, vol. 22, no. 4, pp. 435–9, Apr. 2004.

[144] R. Gorkin, J. Park, J. Siegrist, M. Amasia, B. S. Lee, J.-M. Park, J. Kim, H. Kim, M. Madou, and Y.-K. Cho, “Centrifugal microfluidics for biomedical applications.,” *Lab Chip*, vol. 10, no. 14, pp. 1758–73, Jul. 2010.

[145] J. Thom, L. Ivey, and J. Eikelboom, “Normal plasma mixing studies in the laboratory diagnosis of lupus anticoagulant,” *J. Thromb. Haemost.*, vol. 1, no. 12, pp. 2689–2691, Dec. 2003.

[146] Y. Xie, N. W. Todd, Z. Liu, M. Zhan, H. Fang, H. Peng, M. Alattar, J. Deepak, S. A. Stass, and F. Jiang, “Altered miRNA expression in sputum for diagnosis of non-small cell lung cancer.,” *Lung Cancer*, vol. 67, no. 2, pp. 170–6, Feb. 2010.

[147] C. Krausz, “Male infertility: pathogenesis and clinical diagnosis.,” *Best Pract. Res. Clin. Endocrinol. Metab.*, vol. 25, no. 2, pp. 271–85, Apr. 2011.

[148] H. Song and R. F. Ismagilov, “Millisecond kinetics on a microfluidic chip using nanoliters of reagents.,” *J. Am. Chem. Soc.*, vol. 125, no. 47, pp. 14613–9, Nov. 2003.

[149] X. Mao and T. J. Huang, “Microfluidic diagnostics for the developing world.,” *Lab Chip*, vol. 12, no. 8, pp. 1412–6, Apr. 2012.

[150] X. Mao and T. J. Huang, “Exploiting mechanical biomarkers in microfluidics.,” *Lab Chip*, vol. 12, no. 20, pp. 4006–9, Oct. 2012.

[151] X. Mao, B. K. Juluri, M. I. Lapsley, Z. S. Stratton, and T. J. Huang, “Milliseconds microfluidic chaotic bubble mixer,” *Microfluid. Nanofluidics*, vol. 8, no. 1, pp. 139–144, Aug. 2009.

[152] X. Mao, J. R. Waldeisen, and T. J. Huang, “‘Microfluidic drifting’--implementing three-dimensional hydrodynamic focusing with a single-layer planar microfluidic device.,” *Lab Chip*, vol. 7, no. 10, pp. 1260–2, Oct. 2007.

[153] N.-T. Nguyen and Z. Wu, “Micromixers—a review,” *J. Micromechanics Microengineering*, vol. 15, no. 2, pp. R1–R16, Feb. 2005.

[154] F. Guo, M. I. Lapsley, A. A. Nawaz, Y. Zhao, S. S. Lin, Y. Chen, S. Yang, X. Zhao, and T. J. Huang, “A droplet-based, optofluidic device for high-throughput,

quantitative bioanalysis.," *Anal. Chem.*, vol. 84, no. 24, pp. 10745–9, Dec. 2012.

[155] E. M. Miller and A. R. Wheeler, "Digital bioanalysis.," *Anal. Bioanal. Chem.*, vol. 393, no. 2, pp. 419–26, Jan. 2009.

[156] C.-H. Hsu and A. Folch, "Spatio-temporally-complex concentration profiles using a tunable chaotic micromixer," *Appl. Phys. Lett.*, vol. 89, no. 14, p. 144102, 2006.

[157] A. D. Stroock, S. K. W. Dertinger, A. Ajdari, I. Mezic, H. A. Stone, and G. M. Whitesides, "Chaotic mixer for microchannels.," *Science*, vol. 295, no. 5555, pp. 647–51, Jan. 2002.

[158] D. Therriault, S. R. White, and J. A. Lewis, "Chaotic mixing in three-dimensional microvascular networks fabricated by direct-write assembly.," *Nat. Mater.*, vol. 2, no. 4, pp. 265–71, Apr. 2003.

[159] C. Neils, Z. Tyree, B. Finlayson, and A. Folch, "Combinatorial mixing of microfluidic streams.," *Lab Chip*, vol. 4, no. 4, pp. 342–50, Aug. 2004.

[160] W. Sheng, O. O. Ogunwobi, T. Chen, J. Zhang, T. J. George, C. Liu, and Z. H. Fan, "Capture, release and culture of circulating tumor cells from pancreatic cancer patients using an enhanced mixing chip.," *Lab Chip*, vol. 14, no. 1, pp. 89–98, Jan. 2014.

[161] Q. Mei, Z. Xia, F. Xu, S. a Soper, and Z. H. Fan, "Fabrication of microfluidic reactors and mixing studies for luciferase detection.," *Anal. Chem.*, vol. 80, no. 15, pp. 6045–50, Aug. 2008.

[162] J. Tsai and L. Lin, "Active microfluidic mixer and gas bubble filter driven by thermal bubble micropump," *Sensors Actuators A Phys.*, vol. 97–98, pp. 665–671, Apr. 2002.

[163] A. N. Hellman, K. R. Rau, H. H. Yoon, S. Bae, J. F. Palmer, K. S. Phillips, N. L. Allbritton, and V. Venugopalan, "Laser-induced mixing in microfluidic channels.," *Anal. Chem.*, vol. 79, no. 12, pp. 4484–92, Jun. 2007.

[164] K. S. Ryu, K. Shaikh, E. Goluch, Z. Fan, and C. Liu, "Micro magnetic stir-bar mixer integrated with parylene microfluidic channels.," *Lab Chip*, vol. 4, no. 6, pp. 608–13, Dec. 2004.

[165] M. Riahi and E. Alizadeh, "Fabrication of a 3D active mixer based on deformable Fe-doped PDMS cones with magnetic actuation," *J. Micromechanics Microengineering*, vol. 22, no. 11, p. 115001, Nov. 2012.

[166] G.-P. Zhu and N.-T. Nguyen, "Rapid magnetofluidic mixing in a uniform magnetic field.," *Lab Chip*, vol. 12, no. 22, pp. 4772–80, Nov. 2012.

[167] C.-C. Chang and R.-J. Yang, “Electrokinetic mixing in microfluidic systems,” *Microfluid. Nanofluidics*, vol. 3, no. 5, pp. 501–525, Jun. 2007.

[168] C. K. Harnett, J. Templeton, K. a Dunphy-Guzman, Y. M. Senousy, and M. P. Kanouff, “Model based design of a microfluidic mixer driven by induced charge electroosmosis.,” *Lab Chip*, vol. 8, no. 4, pp. 565–72, Apr. 2008.

[169] M. Sigurdson, D. Wang, and C. D. Meinhart, “Electrothermal stirring for heterogeneous immunoassays.,” *Lab Chip*, vol. 5, no. 12, pp. 1366–73, Dec. 2005.

[170] T. Thorsen, S. J. Maerkl, and S. R. Quake, “Microfluidic large-scale integration.,” *Science*, vol. 298, no. 5593, pp. 580–4, Oct. 2002.

[171] H. Y. Park, X. Qiu, E. Rhoades, J. Korlach, L. W. Kwok, W. R. Zipfel, W. W. Webb, and L. Pollack, “Achieving uniform mixing in a microfluidic device: hydrodynamic focusing prior to mixing.,” *Anal. Chem.*, vol. 78, no. 13, pp. 4465–73, Jul. 2006.

[172] G. G. Yaralioglu, I. O. Wygant, T. C. Marentis, and B. T. Khuri-Yakub, “Ultrasonic mixing in microfluidic channels using integrated transducers.,” *Anal. Chem.*, vol. 76, no. 13, pp. 3694–8, Jul. 2004.

[173] Z. Yang, S. Matsumoto, H. Goto, M. Matsumoto, and R. Maeda, “Ultrasonic micromixer for microfluidic systems,” *Sensors Actuators A Phys.*, vol. 93, no. 3, pp. 266–272, Oct. 2001.

[174] A. Wixforth, C. Strobl, C. Gauer, a Toegl, J. Scriba, and Z. v Guttenberg, “Acoustic manipulation of small droplets.,” *Anal. Bioanal. Chem.*, vol. 379, no. 7–8, pp. 982–91, Aug. 2004.

[175] T. Frommelt, M. Kostur, M. Wenzel-Schafer, P. Talkner, P. Hanggi, A. Wixforth, M. Wenzel-Schäfer, P. Talkner, P. Hänggi, and A. Wixforth, “Microfluidic Mixing via Acoustically Driven Chaotic Advection,” *Phys. Rev. Lett.*, vol. 100, no. 3, p. 034502, Jan. 2008.

[176] W.-K. Tseng, J.-L. Lin, W.-C. Sung, S.-H. Chen, and G.-B. Lee, “Active micro-mixers using surface acoustic waves on Y-cut 128° LiNbO 3,” *J. Micromechanics Microengineering*, vol. 16, no. 3, pp. 539–548, Mar. 2006.

[177] D. Ahmed, X. Mao, B. K. Juluri, and T. J. Huang, “A fast microfluidic mixer based on acoustically driven sidewall-trapped microbubbles,” *Microfluid. Nanofluidics*, vol. 7, no. 5, pp. 727–731, Apr. 2009.

[178] R. H. Liu, J. Yang, M. Z. Pindera, M. Athavale, and P. Grodzinski, “Bubble-induced acoustic micromixing.,” *Lab Chip*, vol. 2, no. 3, pp. 151–7, Aug. 2002.

[179] S. Wang, X. Huang, and C. Yang, “Mixing enhancement for high viscous fluids in a microfluidic chamber.,” *Lab Chip*, vol. 11, no. 12, pp. 2081–7, Jun. 2011.

[180] Y. Li, Y. Xu, X. Feng, and B. Liu, “A rapid microfluidic mixer for high-viscosity fluids to track ultrafast early folding kinetics of G-quadruplex under molecular crowding conditions.,” *Anal. Chem.*, vol. 84, no. 21, pp. 9025–32, Nov. 2012.

[181] D. Qin, Y. Xia, and G. M. Whitesides, “Soft lithography for micro- and nanoscale patterning.,” *Nat. Protoc.*, vol. 5, no. 3, pp. 491–502, Mar. 2010.

[182] H. B. Marschall, K. a. Mørch, a. P. Keller, and M. Kjeldsen, “Cavitation inception by almost spherical solid particles in water,” *Phys. Fluids*, vol. 15, no. 2, p. 545, 2003.

[183] A. Pradhan, R. C. Jones, D. Caruntu, C. J. O’Connor, and M. a Tarr, “Gold-magnetite nanocomposite materials formed via sonochemical methods.,” *Ultrason. Sonochem.*, vol. 15, no. 5, pp. 891–7, Jul. 2008.

[184] A. Shima, “Studies on bubble dynamics,” *Shock Waves*, vol. 7, no. 1, pp. 33–42, Feb. 1997.

[185] E. Zwaan, S. Le Gac, K. Tsuji, and C.-D. Ohl, “Controlled Cavitation in Microfluidic Systems,” *Phys. Rev. Lett.*, vol. 98, no. 25, p. 254501, Jun. 2007.

[186] M. Wiklund, R. Green, and M. Ohlin, “Acoustofluidics 14: Applications of acoustic streaming in microfluidic devices.,” *Lab Chip*, vol. 12, no. 14, pp. 2438–51, Jul. 2012.

[187] D. Köster, “Numerical Simulation of Acoustic Streaming on SAW-Driven Biochips,” University of Augsburg, Germany, 2006.

[188] M. Arora, C.-D. Ohl, and K. Mørch, “Cavitation Inception on Microparticles: A Self-Propelled Particle Accelerator,” *Phys. Rev. Lett.*, vol. 92, no. 17, p. 174501, Apr. 2004.

VITA

Adem Ozcelik

Education

Ph.D., Engineering Science and Mechanics, The Pennsylvania State University, USA (2016)
M.S., Materials Science and Engineering, The Pennsylvania State University, USA (2011)
B.S., Physics, Karadeniz Technical University, Turkey (2007)

Honors and awards

First place, Penn State ESM Today Graduate Research Symposium (2016)
Turkish Ministry of Education abroad study scholarship (2008-2015)
Chemical and Biological Microsystems Society Travel Award (2014)
Socrates\Erasmus European Union Exchange Student Fellowship (2005)

Selected journal publications

1. Daniel Ahmed,* **Adem Ozcelik**,* Nagagireesh Bojanala, Nitesh Nama, Awani Upadhyay, Yuchao Chen, Wendy Hanna-Rose, and Tony Jun Huang, Rotational manipulation of single microparticles, cells, and organisms using acoustic waves, *Nature Communications*, 7, 11085, 2016 (*equal contribution)

2. Murat Kaynak, **Adem Ozcelik**, Amir Nourhani, Nitesh Nama, Paul E. Lammert, Vincent H. Crespi, and Tony Jun Huang, Acoustofluidic Actuation of In Situ Fabricated Microrotors, Under review in *Lab on Chip*

3. **Adem Ozcelik**, Nitesh Nama, Po-Hsun Huang, Murat Kaynak, Wendy Hanna-Rose, and Tony Jun Huang, Acoustofluidic rotational manipulation using oscillating solid structures, Under review in *Small*

4. Feng Guo, Yuliang Xie, Sixing Li, James Lata, Liqiang Ren, Zhangming Mao, Baiyang Ren, Mengxi Wu, **Adem Ozcelik**, and Tony Jun Huang, Reusable acoustic tweezers for disposable devices, Lab on a Chip, accepted, 2015. DOI: 10.1039/C5LC01049G

5. Ahmad Ahsan Nawaz, Yucaho Chen, Nitesh Nama, Ruth Nissly, Liqiang Ren, **Adem Ozcelik**, Lin Wang, J. Phillip McCoy, Stewart J. Levine, and Tony Jun Huang, An Acoustofluidic Fluorescence Activated Cell Sorter, *Analytical Chemistry*, accepted, 2015. DOI: 10.1021/acs.analchem.5b02398

6. Daniel Ahmed, Xiaolei Peng, **Adem Ozcelik**, Yuebing Zheng, Tony Jun Huang, Acousto-Plasmofluidics: Acoustic Modulation of Surface Plasmon Resonance in Microfluidic Systems, *AIP Advances*, 5 (9), 097161, 2015.

7. **Adem Ozcelik**, Daniel Ahmed, Yuliang Xie, Nitesh Nama, Zhiguo Qu, Ahmad Ahsan Nawaz, Tony Jun Huang, An acoustofluidic micromixer via bubble inception and cavitation from microchannel sidewalls, , *Analytical Chemistry*, 86 (10), 5083-5088, 2014

8. Daniel Ahmed, Hari S Muddana, Mengqian Lu, Jarrod B French, **Adem Ozcelik**, Ye Fang, Peter J Butler, Stephen J Benkovic, Andreas Manz, Tony Jun Huang, Acoustofluidic Chemical Waveform Generator and Switch, *Analytical Chemistry*, 86 (23), 11803-11810, 2014